ABSTRACT

Title of Proposal: Modeling Key Issues in Post Silicon Semiconductors: Germanium and Gallium Nitride

Ziyang Xiao, Doctor of Philosophy, 2018

Proposal directed by: Professor Neil Goldsman
Department of Electrical and Computer Engineering

We are rapidly approaching the end of the semiconductor roadmap with respect to silicon. To continue its growth, the semiconductor industry is therefore looking into new materials. Two primary materials that are of interest for continuing semiconductor development are germanium (Ge) and gallium nitride (GaN). Ge is of interest as a replacement for silicon, in an effort to improve electronics performances because of its high mobility and its ability to grow a native oxide. In addition, Ge is of interest because of its potential use for economical CMOS-based short wave infrared (SWIR) imaging systems. GaN is a nascent wide bandgap semiconductor and has many potential applications in high power electronics and ultraviolet imaging systems. In this thesis, the key material properties and applications of these two "end of the roadmap" semiconductors are explored.

Ge is a semiconductor material with an indirect bandgap of 0.66eV[1]. This bandgap value corresponds to a wavelength of 1.88μm, which lies in the infrared range. The Ge material itself is also compatible with the standard Si CMOS process technology. Because of these advantages, Ge is considered a candidate for the

application of photo detecting in the SWIR range. Apart from the indirect bandgap of 0.66eV, Ge also has a direct bandgap of 0.8eV[1]. From early research, the relatively small offset between the indirect and direct bandgaps can be inverted either by applying strain[1, 9, 10, 11] or alloying with tin[2, 14].

GaN is a binary direct wide bandgap material with a direct bandgap of 3.4eV[26, 27]. It has a high breakdown field, and relatively high saturation velocity and carrier mobility[28]. These properties give GaN an advantage in the realm of high power application. GaN can also form a heterostructure with AlGaN, which can give rise to a 2D electron gas (2DEG) layer at the interface without intentionally doping either material. The 2DEG layer has an even higher mobility when compared to the mobility of the bulk GaN, which allows the heterostructure to be utilized for the design of high electron mobility transistors (HEMTs). The formation of the 2DEG layer also gives rise to potential well confinement at the heterostructure interface. The width of the potential well is only a few nanometers, making the interface electron gas subject to quantum confinement along the direction perpendicular to the interface. The detailed shape of the potential well is determined by the configuration of the heterostructure, as well as the applied voltage across the heterostructure.

The first set of goals for this research is to investigate how the bandstructure of Ge changes: Part (1) with the applied strain, and Part (2) with alloyed tin (Sn). The empirical pseudopotential method (EPM) was utilized for the band structure calculation, together with the rules for strain translation for the investigation of Part (1). In Part (1), simulation results give the optimal orientation for different

types of applied strain and also thoroughly map the influence of strain applied on any arbitrary orientations. It also reveals that for biaxial strain, there exists another orientation that is more robust against misalignment with respect to the originally desired orientation than the optimal plane, with little compromise of bandgap and slightly higher requirements for the sufficient strain. For Part (2), EPM is combined with perturbation theory for the inclusion of the influence of the Sn atoms in the Ge lattice. A new and computationally inexpensive method is developed during the research. Simulation results agree significantly when compared to reported experimental measurements, indicating the capability of the method.

The second set of goals is to investigate the electron transport properties of the 2DEG layer at the interface of GaN HEMT and related power transistors. The potential well is approximated and quantified by a triangular potential well and the carrier sheet density is kept the same during the approximation. Thorough simulations are conducted by calculating the band alignment of the heterostructure with different structural configurations. A fixed correlation between the carrier sheet density and the shape of the potential well (slope of the triangular potential well and the height of the well) is revealed. This correlation is used as an input for the Monte Carlo (MC) simulation. The changes to the mobility of the electrons at the 2DEG layer with changing interface potential well shape are investigated and statistics of drift velocity, electron energy, and valley occupation are collected. Mobility information is also extracted and compares favorably with reported experimental measurements. The simulation results are used in the device simulations, which compares the performances of two GaN/AlGaN heterostructure based devices: a

lateral HEMT and a current aperture vertical electron transistor (CAVET).

Thesis Structure

Chapter 1 presents the background and literature review. It explains the background knowledge of this thesis and the necessity of this research.

Chapter 2 through Chapter 4 focus on the band structure engineering of Ge, aiming to transform Ge from an indirect bandgap material to a direct bandgap one. Chapter 2 explains the methodology of band structure calculation using EPM. Chapter 3 investigates the band structure of Ge under the influence of strain and Chapter 4 develops a new method to calculate the band structure of GeSn alloy.

Chapter 5 through Chapter 7 introduce the MC method to investigate the electron transport properties of GaN material. Chapter 5 lists and describes all the included scattering mechanisms for the MC simulation. Chapter 6 conducts MC simulation for bulk GaN, while Chapter 7 describes the quantum confinement of 2DEG and how to model the potential well for 2DEG and conducts 2D MC simulation for 2DEG under different potential well parameters. Chapter 8 conducts the device simulations on two types of GaN based devices using our simulation results and compares their simulation results to provide insight into device design.

Chapter 9 summarizes the contribution and major results of the thesis.

Modeling Key Issues in Post Silicon Semiconductors: Germanium and Galium Nitride

by

Ziyang Xiao

© Copyright by
Ziyang Xiao
2018

Acknowledgments

I would like to thank all the people who have made this journey possible and full of memories that I'll cherish for the rest of my life.

First and foremost, I owe my greatest gratitude towards my advisor, Professor Neil Goldsman, for giving me this invaluable opportunity to work with him on these challenging and fascinating projects over the years. He has already been kind and encouraging for all the progress I've been making, and supportive and informative for all the obstacles I came across throughout the years, both academically and personally. It has been a great pleasure to work with a person with a such intellectual mind and a wonderful personality.

I would also like to thank Professor Agis Iliadis, Professor Aris Christou, Professor Pamela Abshire and Professor Kevin Daniels for agreeing to serve on the committee and for sparing their invaluable time reviewing the thesis.

Christopher Darmody, as my oldest buddy at the lab, has been such a delight to work with. I will always cherish all the great discussions we had and all the help I received from him since day one when I joined the team. Ittai Baun, a math genius in my opinion, has the most curious mind I've ever seen, and is quite funny too. Yuming Cui, who is always so thorough with all the matters, has always been a pleasure for me to see him working and I can see great success in his future. This team is the best that anyone can ask for. We are always there for each other, for big and for small.

Special thanks to my family. My parents, Haizhou Xiao and Zhenwen Hu,

who are all the way across the globe, have been giving me support since I was born. My husband, Daniel J. Pekar, even though only joined the journey with me halfway, has been my greatest support. Thank you for being the most patient and lovable person. Mrs. Janette Pekar, You are my mother far away from home and thank you for your support in my life. Zhi (Jenny) Gao, you let me realize that a best friend does not have to be lifelong, just needs to be there at the right time. Peiwen He, my friend since day one at the University of Maryland, thank you for all the dinner parties.

Last but not least, for those I fail to mention here, I'll always remember all of your help and your support along this journey.

Table of Contents

List of Tables vi

List of Figures vii

1 Background and Literature Review 1
- 1.1 Germanium (Ge) Crystal and Band Structure 1
  - 1.1.1 Empirical Pseudopotential Method (EPM) 2
  - 1.1.2 Strained Germanium (Ge) and Germanium-Tin (GeSn) Alloy 6
- 1.2 Gallium Nitride (GaN) Electron Transport 9
  - 1.2.1 Gallium Nitride/Aluminum Gallium Nitride (GaN/AlGaN) Heterostructure and Formation of 2D Electron Gas (2DEG) . 10
  - 1.2.2 Monte Carlo (MC) method 16

2 Germanium (Ge) Band Structure Calculations 19
- 2.1 Empirical Pseudopotential Method (EPM) for Calculating Germanium (Ge) Band Structure 20
- 2.2 Crystal Structure for Germanium (Ge) 22
- 2.3 Calculation Results 29

3 Germanium Band Structure Under Strain 34
- 3.1 Strain Translation of Ge Crystal 34
- 3.2 Band Structure Calculation Using the Empirical Pseudopotential Method (EPM) for Strained Germanium (Ge) 36
- 3.3 Results and Analysis 37
  - 3.3.1 Strain Along Commonly Used Orientations 37
  - 3.3.2 Strain Along Arbitrary Orientation 40

4 Band Structure of Germanium-Tin (GeSn) alloy 49
- 4.1 Band Structure Calculation for Germanium (Ge) and Tin (Sn) using the Empirical Pseudopotential Method (EPM) 50
- 4.2 Volume Change for Germanium-Tin (GeSn) alloy 52
- 4.3 Accounting for Potential Energy Changed from Tin (Sn) Substitution 55
  - 4.3.1 Genetic Algorithm for Single Atom Pseudopotential 56
  - 4.3.2 First-Order Perturbation Theory Accounting for Potential Energy Changed from Tin (Sn) Substitution 59
- 4.4 Results and Analysis 61
  - 4.4.1 Volume Change 61
  - 4.4.2 Potential Difference between Germanium (Ge) and Tin (Sn) . 65
  - 4.4.3 Combined Volume Change and Perturbation Effects 66
  - 4.4.4 Comparison with Reported Experiments 66

5 Scattering Mechanisms for Monte Carlo (MC) Simulation 70
5.1 Acoustic Phonon Scattering . . . 72
5.1.1 Acoustic Phonon Scattering Rate for Bulk Electrons . . . 72
5.1.2 Acoustic Phonon Scattering Rate for 2D Electron Gas (2DEG) 77
5.2 Piezoelectric Scattering . . . 82
5.2.1 Piezoelectric Scattering Rate for Bulk Electrons . . . 82
5.2.2 Piezoelectric Scattering Rate for 2D Electron Gas (2DEG) . . 85
5.3 Polar Optical Scattering . . . 86
5.3.1 Polar Optical Scattering Rate for Bulk Electrons . . . 86
5.3.2 Polar Optical Scattering Rate for 2D Electron Gas (2DEG) . . 88
5.4 Impurity Scattering . . . 89
5.5 Intervalley Scattering . . . 90
5.6 Scattering Angle Selection . . . 93
5.7 Summary . . . 95

6 Investigation of Electron Transport in Bulk Gallium Nitride (GaN) 97
6.1 Calculation of the Scattering Rates and Analysis . . . 97
6.2 Set up for Bulk Gallium Nitride (GaN) Monte Carlo (MC) Simulation 103
6.3 Results and Analysis . . . 105

7 Investigation of Electron Transport in 2D Electron Gas (2DEG) 113
7.1 Quantum Confinement of 2D Electron Gas (2DEG) . . . 113
7.2 Modeling of 2D Electron Gas (2DEG) Potential Well . . . 120
7.3 Investigation of the Relationship Between 2D Electron Gas (2DEG) and Potential Well Structure Parameters . . . 123
7.4 Set up for 2D Electron Gas (2DEG) Monte Carlo (MC) Simulation . 129
7.5 Results and Analysis . . . 131
7.5.1 High Electric Field Simulation . . . 131
7.5.2 Low Electric Field Simulation . . . 136

8 Gallium Nitride (GaN) Device Overview and Simulation 140
8.1 Device Simulation of High Electron Mobility Transistor (HEMT) . . . 143
8.2 Device Simulation of Current Aperture Vertical Electron Transistor (CAVET) . . . 148
8.3 Summary . . . 156

9 Summary 158
9.1 Summary of Germanium (Ge) . . . 158
9.2 Summary of Gallium Nitride (GaN) . . . 161

Bibliography 165

List of Tables

1.1 Material properties corresponding to spontaneous and piezoelectric polarization for GaN and AlN 14

2.1 $\vec{G}$ groups included in the empirical pseudopotential method (EPM) calculation of germanium (Ge) band structure 26
2.2 Form factors for the calculation using Empirical Pseudopotential Method (EPM) of Ge. $|\vec{G}|^2$ are in unit of $(2\pi/a_0)^2$ 30
2.3 Empirical Pseudopotential Method (EPM) calculation compared to experimental data and first principle calculation collected from literature 33

3.1 Coefficients for continuous form factors for Empirical Pseudopotential Method (EPM) for Ge 37
3.2 Calculation results of strained Ge: strain at the transition point (STP) and Bandgap at the transition point (BTP) 39

4.1 Form factors for the calculation using Empirical Pseudopotential Method (EPM) of Sn 50
4.2 Reported bowing parameter for the alloy lattice constant and the corresponding used method 54
4.3 Comparison of the measurements of the samples reported in literature and the calculated values of this work 69

6.1 Material properties of gallium nitride (GaN) and parameters for the three-valley model for Monte Carlo (MC) 98
6.2 Comparison of simulated results for gallium nitride (GaN) electron transport properties 111

7.1 Gallium nitride/aluminum gallium nitride (GaN/AlGaN) heterostructure parameters for Poisson's equation solver 124

8.1 Key parameters for High Electron Mobility Transistor (HEMT) simulated using Genius 143
8.2 Key parameters for Current Aperture Vertical Electron Transistor (CAVET) 149

List of Figures

1.1 The conventional unit cell with illustrated primitive unit cell. 3
1.2 The reciprocal lattice for a wurtzite crystal 4
1.3 The crystal structure for GaN 11
1.4 Four possible configurations for GaN/AlGaN heterostructures 13
1.5 Formation of 2DEG 16
1.6 Flowchart of the single-particle MC simulation 18

2.1 The reciprocal lattice for Ge crystal 25
2.2 Calculation results of the band structure of Ge in this work. 31
2.3 Band structure illustration for Table. 2.3 31
2.4 Contour of the 2D band structure of Ge 32

3.1 Band structure of relaxed and strained Ge 38
3.2 Projection of Miller indices for directions 42
3.3 Projection of Miller Indices for directions 42
3.4 Bandgap at Transition Point (BTP) and applied Strain at Transition Point (STP) vs. different orientations of the plane under uniaxial strain 43
3.5 Bandgap at Transition Point (BTP) and applied Strain at Transition Point (STP) vs. different orientations of the crystal direction under biaxial strain 44
3.6 Bandgap at Transition Point (BTP) and applied Strain at Transition Point (STP) under uniaxial strain on path $\langle 100\rangle$-$\langle 111\rangle$-$\langle 110\rangle$ 46
3.7 Bandgap at Transition Point (BTP) and applied Strain at Transition Point (STP) under biaxial strain on path $\{111\}$-$\{100\}$-$\{110\}$ 47

4.1 Calculation results of the band structure of tin (Sn) and germanium (Ge) 51
4.2 Flowchart of the genetic algorithm for extracting single atom pseudopotential. 57
4.3 Pseudo-potential of germanium (Ge) and tin (Sn) and the potential difference between Sn and Ge (ΔV) versus radial distance from the nucleus 60
4.4 The direct and indirect bandgaps versus the tensile hydrostatic strain 62
4.5 Band structure of the germanium (Ge) lattice without volume change and perturbation 63
4.6 Germanium (Ge) Band structure shift due to volume change 63
4.7 Germanium (Ge) Band structure shift due to perturbation 64
4.8 The direct and indirect bandgap with respect to different fraction of alloyed tin (Sn) 67
4.9 The minimum fraction of tin (Sn) required to achieve the indirect-direct transition and the transition point bandgap (BTP) vs. bowing parameter 67

6.1 Empirial pseudopotential method (EPM) calculated conduction band structure with the illustration of included valleys for Monte Carlo (MC) simulation . . . 99
6.2 The calculated scattering rates vs. electron energy for Γ_1, Γ_3 and U valley. . . . 100
6.3 The calculated impurity scattering rates vs. electron energy for Γ_1 valley, Γ_3 valley and U valley under different impurity concentrations. 101
6.4 The calculated impurity scattering angle vs. generated random number for Γ_1 valley at electron energy of 0.002 eV under different impurity concentrations. . . . 101
6.5 (Top) The electron energy versus simulation time (ranging from 0 to 0.2ns) at the electrical field of 130kV/cm with the impurity concentration of $10^{17}cm^{-3}$. (Bottom) Zoom-in of the top figure at around 0.1ns simulation time. Every red cross mark represents a scattering event. . . . 106
6.6 The average electron energy versus the electric field (full range: 0 - 450kV/cm) with the impurity concentration of $10^{17}cm^{-3}$. The insets are distributions of the sampled electron energies (the probability density of the electron energy) at selected electric field of 10kV/cm, 130kV/cm and 300kV/cm . . . 107
6.7 The valley occupation percentages for valleys Γ_1, Γ_3 and U versus the electric field (full range: 0 - 450kV/cm) with the impurity concentration of $10^{17}cm^{-3}$ . . . 108
6.8 The drift velocity versus the electric field (full range: 0 - 450kV/cm) with the impurity concentration of $10^{17}cm^{-3}$. The insets are the distribution of the sampled instantaneous velocity (the probability density of the instantaneous velocity) during the simulation at selected electrical fields of 10kV/cm, 130kV/cm and 250kV/cm . . . 110
6.9 Bulk low-field mobility vs. impurity concentration extracted from Monte Carlo (MC) simulation. . . . 112

7.1 Sketch of the band alignment of gallium nitride/alunimum gallium nitride (GaN/AlGaN) heterostructure after the formation of 2D electron gas (2DEG) . . . 114
7.2 Sketch of the density of state: 3D vs 2D . . . 115
7.3 Sketch of the potential well for 2D electron gas (2DEG) at the heterostructure interface with approximated triangular potential well . . 116
7.4 The approximated wave functions $|\Psi|^2$ for two triangular potential wells . . . 118
7.5 Scattering rate comparison between 3D scattering and 2D scattering . 119
7.6 Band alignment for gallium nitride/alunimum gallium nitride (GaN/AlGaN) heterstructure after the formation of 2D electron gas (2DEG) and the illustration of approximating the potential well . . . 122
7.7 Schematic of the simulated gallium nitride/aluminum gallium nitride (GaN/AlGaN) heterostructure . . . 124

7.8 Left: Potential well slope (S_{int}) vs. Interface carrier sheet density (σ_{int}) with different parameters changing from default values. Right: S_{int} vs. selected parameters in the right graph with σ_{int} chosen at $3 \times 10^{12} cm^{-2}$. 125
7.9 Left: Potential well height (E_t) vs. interface carrier sheet density (σ_{int}). Right: potential well width (l_w) vs. σ_{int} 128
7.10 The first three subband energy levels (E_1, E_2, E_3) and potential well height (E_t) versus their correlated potential well slope (S_{int}) 130
7.11 Drift velocity versus electric field at different potential well slope (S_{int}) 132
7.12 Valley occupation percentages versus electric field at different potential well slope (S_{int}) 132
7.13 Interpolated peak velocity and electric field to achieve peak velocity versus potential well slope (S_{int}) 135
7.14 Drift velocity versus electric field at different potential well slope (S_{int}) 135
7.15 Mobility vs. electric field at different potential well slope (S_{int}) 136
7.16 Low-field mobility (μ_0) vs. potential well slope (S_{int}). 137
7.17 Low-field mobility (μ_0) vs. the sheet density of 2DEG (S_{int}) 138

8.1 Schematic of a gallium nitride/aluminum gallium nitride (GaN/AlGaN) based high electron mobility transistor (HEMT) 141
8.2 Schematic of a gallium nitride/aluminum gallium nitride (GaN/AlGaN) based current aperture vertical electron transistor (CAVET) 142
8.3 Meshing for the simulation of the lateral high electrom mobility transistor (HEMT) 144
8.4 Drain current versus gate voltage characteristic of the simulated lateral high electron mobility transistor HEMT 145
8.5 Sheet electron density at the heterostructure interface versus the applied gate voltage with V_{ds}=0.02V for the high electron mobility transitor (HEMT) 145
8.6 Drain current versus drain voltage at various gate voltages for the lateral high electron mobility transistor (HEMT) 146
8.7 Electron concentration profile under different bias conditions for the high mobility electron transistor (HEMT) 147
8.8 Meshing for the simulation of the vertical Current Aperture Vertical Electron Transistor (CAVET) 150
8.9 Drain current versus gate voltage characteristic of the simulated current aperture vertical electron transistor (CAVET) 152
8.10 Sheet electron density at the heterostructure interface versus the applie gate voltages for the current aperture vertical electron transistor (CAVET) 152
8.11 Drain current versus drain voltage at various gate voltages for the current aperture vertical electron transistor (CAVET) 153
8.12 Electron concentration profile under different bias conditions for the current aperture vertical electron transistor (CAVET) 155

Chapter 1

Background and Literature Review

This chapter provides the background to, and review of the literature around the topics related to Ge and GaN that are germane to the research on post-silicon semiconductors proposed for this thesis.

1.1 Germanium (Ge) Crystal and Band Structure

Ge is a semiconductor material with a diamond crystal structure. It has re-drawn attention in the realm of photo detecting in the SWIR range because of its advantage of being well suited for integration into a CMOS process[1], as well as having a direct bandgap of 0.8eV and an indirect bandgap of 0.66eV[1], with the difference between the two being only 0.14eV. Even though photo detectors are achievable using the indirect bandgap material, such as silicon and gallium phosphide, due to the nature of the indirect bandgap material, the photon absorption coefficient varies less abruptly with wavelength than with the direct bandgap material. In addition, the probability of light absorption for photon energies greater than the bandgap is less than that of direct gap materials.

Strain engineering is a possible method for transforming Ge from being indirect to direct bandgap. When Ge is under tensile strain, both the direct and indirect bandgaps are reduced. When enough tensile strain is applied along certain

orientations (i.e. uniaxial $\langle 111 \rangle$, biaxial $\{100\}$[1])[1], the direct bandgap gets pushed lower than the indirect bandgap, thus Ge becomes a direct bandgap material.

A similar phenomenon can also be observed with a GeSn alloy. Sn is also a Group IV element, Sn has two major allotropes: α-Sn which has a diamond crystal structure, more stable at low temperature; and β-Sn, a malleable metal, more stable at room temperature. The band structure of α-Sn is calculated to have zero band gap with its bottom-most conduction touching the top-most valence band. This band structure is believed to help push the direct bandgap of Ge downwards, passing the indirect bandgap, when a Ge-Sn alloy is fabricated. The alloy is still mainly composed of Ge, with a small percentage of Sn introduced to achieve the direct gap [2].

1.1.1 Empirical Pseudopotential Method (EPM)

Ge has a diamond crystal structure (shown in Fig. 1.1). For a diamond crystal, the primitive cell consists of two atoms, which are also illustrated in Fig. 1.1.

The reciprocal lattice of a diamond crystal is shown in Fig. 1.2, with high symmetry points labeled. A irreducible wedge of the reciprocal lattice is also shown in the figure. This is the smallest region that can reproduce the entire reciprocal lattice.

To quantify a band structure, experimental methods are limited to being able

[1]Notation: We use the standard notations for Miller Indices where curly brackets represent a family of planes; angled brackets represent a family of directions; parentheses represent a single plane and square brackets represent a single direction.

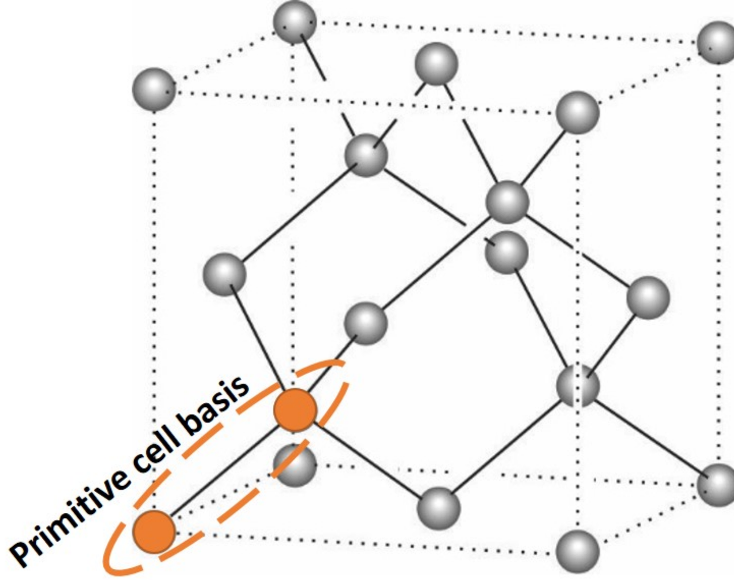

Figure 1.1: The conventional unit cell with illustrated primitive unit cell.

to measure certain points or certain band-to-band transition energies on the band structure. A band structure calculation is usually needed in order to obtain more details. There are numerous methods available for the calculation. First principle calculations such as density functional theory (DFT), are able to calculate the ground state energy of a many body system. These kinds of calculations are usually without empirical fitting. However, purely first principle calculations usually give results which show significant discrepancies when compared to experimental data. Therefore, techniques such as hybrid functionals are commonly used to adjust the calculation to agree with experiments. The huge computational expense to achieve convergence is a disadvantage of such calculations, usually requiring massively parallel computation[3].

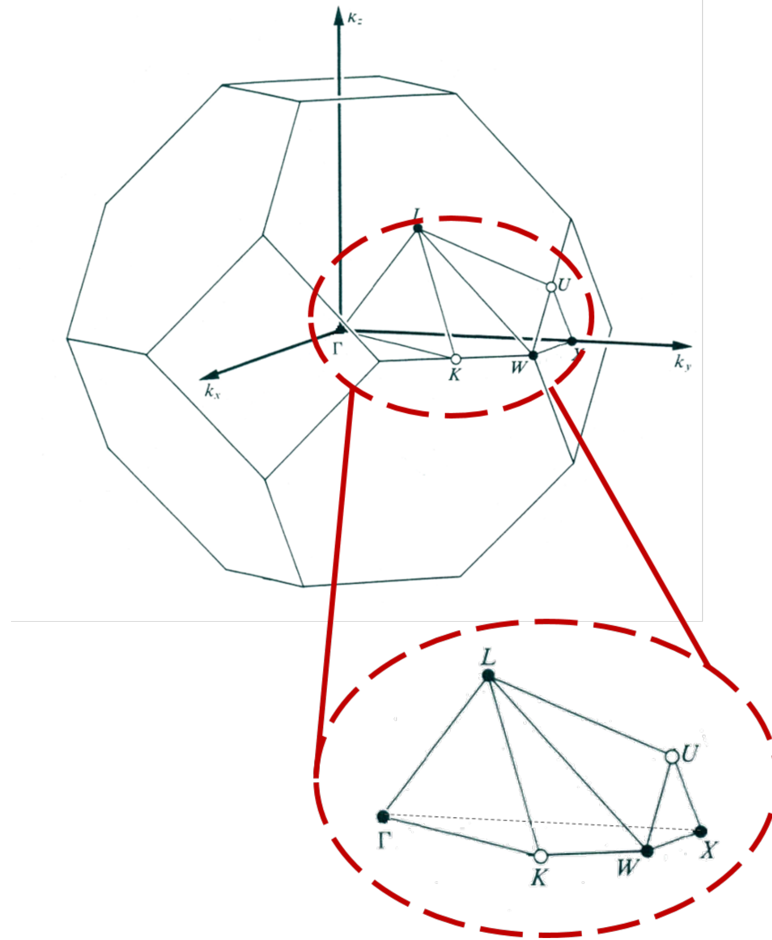

Figure 1.2: The reciprocal lattice for a wurtzite crystal with high symmetry points labeled. Zoom in onto the irreducible wedge of the reciprocal lattice.

As well as first principle calculations, another group of calculation methods is widely used in the band structure calculation with empirically fitted parameters. Other approaches are the tight-binding method (TB)[4], the **k·p** method[5] and the EPM[6, 7]. A big advantage of these methods as opposed to the first principle calculations, is that they solve the one-electron Schrödinger equation instead of the many-body equation, therefore the calculation expenses are hugely reduced. The TB method can accurately describe the valence bands, while improving the accuracy of the conduction band would destroy the simplicity of the method[3]. **k·p** method is excellent at calculating band structure around the Γ point and the effective mass. The simplicity goes away when the method is used to conduct a full band calculation. Both TB and **k·p** method have some level of first principle atomic orbital approximation for the valence electrons, and they both get more and more complicated when the mixing of orbitals is taken into consideration.

EPM has the lowest computational expenses of the three methods. Its parameters are fitted based on experimental measurements. EPM takes advantage of the periodicity of the lattice and uses a pseudopotential, rather than the real potential, to reduce the bases needed to reconstruct the potential term used in the calculation. Using the pseudopotential allows the solution to be focused on the valence electrons, which are most important for semiconductors, as opposed to the core levels. The method becomes slightly complicated when the non-locality is included in the method (nonlocal EPM), but this correction is used to account for the effect that the angular momentum of the core electrons has on the pseudopotential[7]. Nonetheless, EPM has relatively the lowest computational expense.

Numerous papers report the band structure calculation on Ge[6, 7, 8]. Ref. [6] and Ref. [8] both use the local EPM to calculate the band structure. The calculation results for direct/indirect bandgap are $\sim 1.1/1eV$ and $0.794/0.923eV$. Both calculations show significant discrepancies when compared to experimental values for bandgaps of $0.66/0.8eV$. In Ref.[7], it is pointed out that "purely local pseudopotential technique could not yield satisfactory results, an energy dependent and nonlocal pseudopotential should be considered." In Ref.[7], the calculated direct/indirect bandgaps are given as $0.76/0.90eV$.

1.1.2 Strained Germanium (Ge) and Germanium-Tin (GeSn) Alloy

Strain is defined as the deformation of a material divided by its original dimension. When strain is applied, the spacing between the atoms changes. A strain in considered tensile if the effect is increase of the spacing between the atoms. The deformation of the lattice also changes the potential distribution of the nuclei, which consequently alters the band structure of Ge. When the strain is tensile, both the indirect and the direct bandgaps tend to decrease. Under certain strains, the direct bandgap is pushed even below the indirect bandgap; at which point, Ge becomes a direct bandgap material. The value of the bandgap when Ge transforms from an indirect to direct semiconductor upon the application of strain is named the "bandgap transition point" (BTP), and the required strain is named "strain at transition point" (STP) in this work.

There are three basic types of strain commonly described in the literature:

(a) Uniaxial: the stress is applied along a certain direction, such as in a nanowire;

(b) Biaxial: the stress is applied on a certain plane, such as in a deposited film on a substrate;

(c) Hydrostatic: the stress is applied equally on all three directions.

Previous research has focused on uniaxial and biaxial strained Ge on the conventional orientations, as these types of strain are more viable for engineering. Cicek et al. (2014) report a requirement of 2% tensile biaxial strain threshold in a {100} plane; while for a uniaxial stress, more than 4% is required for the direct-indirect transition to happen[1]. Aldaphri et al. (2012) report a 4.5% biaxial strain on the {110} plane, with no transition if the strain is applied on the {111} plane[9]. On the $\langle 111 \rangle$ direction, a uniaxial strain of 4.2% and 4.7% are reported in Ref. [10] and Ref. [11]

One of the advantages of Ge is that it is compatible with the silicon CMOS process, which usually involves a silicon substrate. In Ref. [12], it is suggested that by using a {100} Si substrate with a miscut angle, the quality of relaxed graded Si-Ge and Ge layers are greatly improved in the surface roughness and dislocation densities when compared to those grown on an on-axis {100} substrate. The miscut angle ranges from 2° to 6°, and then inevitably passes onto the grown Si-Ge or Ge layer on top, which changes how the strain is applied to the deposited or grown material on top of the substrate. Therefore, research into how the misalignment affects the indirect-direct bandgap transition phenomenon is needed.

Sn, or α-Sn to be more specific, is a zero bandgap semiconductor material with

a diamond crystal structure, like Ge, and is one row below Ge in the periodic table. Its band structure has zero bandgap with a sharp valley in the conduction band in contact with the top of the valence band at the Γ point. The alloying of Sn into Ge is expected to lower the Γ point valley in the conduction band of the Ge band structure. With increasing Sn fraction, the Γ point will eventually become lower in energy than the L point in the conduction band, making the Ge-Sn alloy a direct bandgap material. Regarding how much Sn is needed to achieve the indirect-direct bandgap transition of the Ge-Sn alloy, various theoretical investigations have been carried out. These investigations range from quasi-empirical methods, such as the combined empirical pseudo-potential method/virtual lattice approximation method (EPM/VLA)[13], to first principle calculations using DFT[14, 15, 16]. Experimental efforts sought to grow the alloy with a different fraction of Sn and to measure the photon absorption properties[2, 20, 17, 14, 19] to directly observe the transition.

Considering the theoretical calculations, the EPM could provide accurate bandgaps once a proper pseudopotential was determined. The EPM has been shown to provide the correct bandgap energy for group IV crystalline materials, including Ge and Sn[6]. The combined EPM/VLA is an approach to calculating the alloy band structure by taking the pseudopotentials for the alloy as a linear combination of the two alloy elements in the alloy. While this approach is intuitive and relatively computationally efficient, the linear approximation is difficult to fully justify[17]. The DFT method accounts for the many-body interaction of the alloy. However, it is extremely computationally intensive for supercells that are sufficiently large to account for the various ratios of alloy components. In addition, since the DFT

really focuses on the ground state energy, it is not always optimal for calculating bandgaps. Different hybrid functionals used in DFT calculations yield differing results[17, 25, 16], as the Sn fraction to achieve the transition varies from 1.6%[25] to 17%[17].

1.2 Gallium Nitride (GaN) Electron Transport

GaN is a binary direct wide bandgap material with a direct bandgap of approximately 3.4eV[28]. It has a high breakdown voltage and relatively high saturation velocity and carrier mobility[28]. GaN can also form an alloy with aluminum nitride (AlN) forming $Al_xGa_{1-x}N$ with mole fraction percentage x ranging from 0 to 1, and bandgap changing from 3.4eV (corresponding to the bandgap of GaN) to 6.2eV [29] (corresponding to the bandgap of AlN).

A heterostructure can be formed when the two materials (GaN and AlGaN) are brought together. An accumulation of electrons also occurs at the interface, resulting in a Two Dimension Electron Gas (2DEG) layer without any intentional doping on either material[30]. This layer of 2DEG has different properties when compared to electrons in the bulk material, such as higher mobility. The presence and the advanced properties of the 2DEG at the interface of the heterostructure give rise to the possibility of the application of the High Electron Mobility Transistors (HEMTs)[31].

The formation of the 2DEG layer is accompanied by the formation of a potential well at the interface, in which the electrons are confined. The width of

the potential well is in the range of nanometers, confining the 2DEG quantum in the direction perpendicular to the interface. However, the specific structure of the potential well highly depends on the components of the heterostructure, as well as the applied voltage across the heterostructure. However, the changing of the electron transport properties with the changing parameters of the structure of the heterostructure is not well-known.

1.2.1 Gallium Nitride/Aluminum Gallium Nitride (GaN/AlGaN) Heterostructure and Formation of 2D Electron Gas (2DEG)

Both GaN and AlGaN have a crystal structure of wurtzite. This structure lacks symmetry along the <0001> direction and there is polarity in the Ga-N bond, therefore GaN has spontaneous polarization. The spontaneous polarization points toward the N-face; in effect, it is the $< 000\bar{1} >$ direction. Ga-face, N-face and the direction of the spontaneous polarization are shown in Fig. 1.3.

A piezoelectric property also rises from the wurtzite crystal configuration for GaN, which, if the crystal is under stress, will also give rise to polarization. This polarization is called piezoelectric polarization.

AlGaN shares this characteristic of spontaneous polarization and piezoelectric polarization, when under stress. For a GaN/AlGaN heterostructure, a mismatch of lattice constant is usually present. More specifically, when a film is deposited onto a substrate with a lattice mismatch in between, the film is forced to accommodate the lattice of the substrate, resulting in strain in the film, until the film reaches a

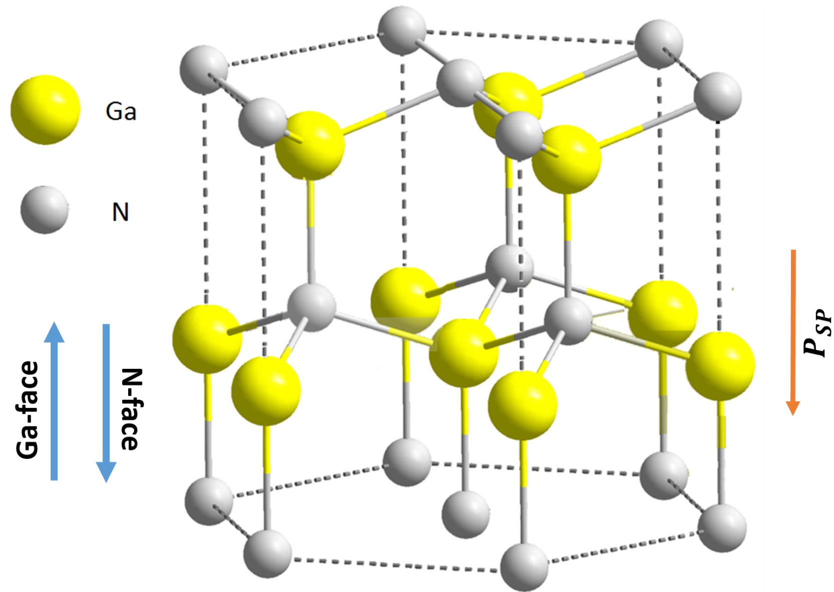

Figure 1.3: The crystal structure for GaN. The growth toward $< 0001 >$ is called the Ga-face and the growth toward $< 000\bar{1} >$ is called the N-face. The spontaneous polarization (P_{SP}) of GaN is aligned with N-face.

critical thickness when dislocations are generated to release the stress caused by the lattice mismatch.

Depending on the material chosen for the substrate and the film, and/or the direction in which the growth is happening, spontaneous polarization and piezoelectric polarization of the deposited film can either be enhanced or weakened. The possible combinations of heterostructures consisting of GaN and AlGaN are shown in Fig. 1.4.

As shown in Fig. 1.4, when GaN is chosen as the substrate material and AlGaN film is deposited, the two types of polarization are of the same direction in the film, despite the direction of the growth. In contrast, when GaN is deposited on AlGaN, the two types of polarization are of the opposite direction in the film. Regardless of the configuration of the heterostructure, there is always an abrupt change of polarization when crossing the heterostructure interface. This change gives rise to a layer of induced charge at the interface, and at each end of the heterostructure. The quantity of the polarization induced charge is given by Eq. 1.1

$$\sigma = -(P_{film} - P_{substrate}) \tag{1.1}$$

$$P_{film} = (P_{PZ} + P_{SP})_{film} \tag{1.2}$$

$$P_{substrate} = (P_{SP})_{substrate} \tag{1.3}$$

where:

P_{PZ} is the piezoelectric polarization

P_{SP} is the spontaneous polarization.

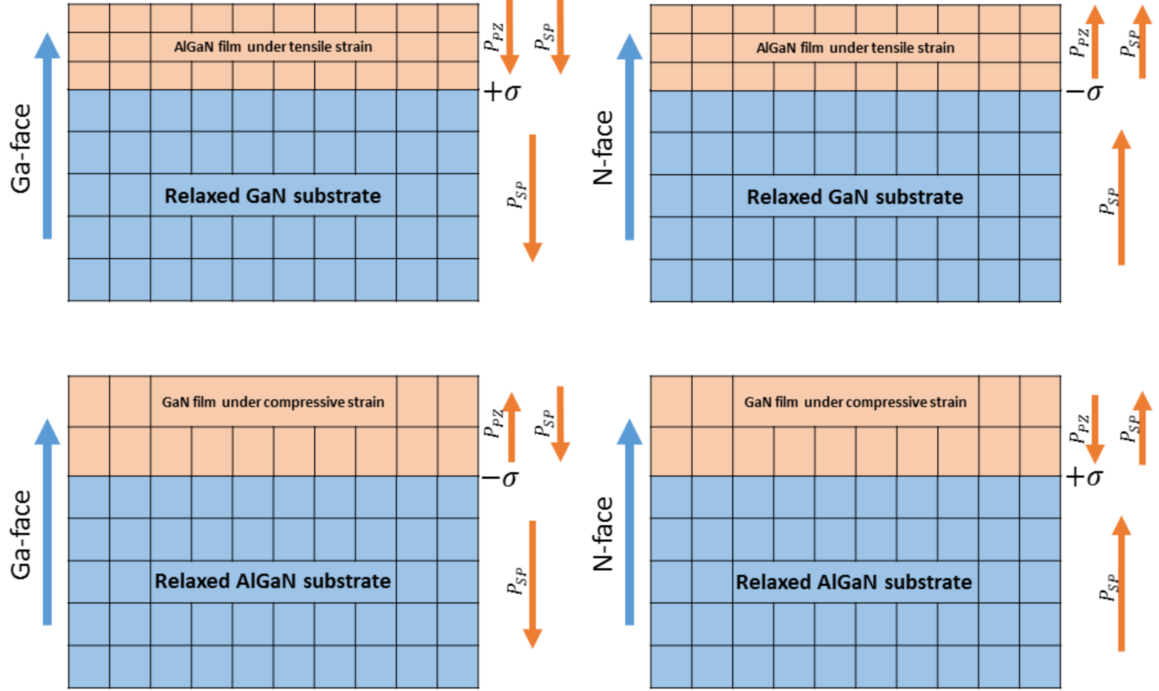

Figure 1.4: Four possible configurations of GaN/AlGaN heterostructures: the direction of the blue arrows are the growth direction and the orange arrows are the direction of the polarization. The induced interface charges are also labeled with a proper sign indicating whether they are positive or negative charges

NOTE: If the polarization is in the direction of the growth direction, the sign is positive and if the polarization is in the opposite direction to the growth, the sign is negative.

Some material properties regarding the polarization of the GaN/AlGaN heterostructure are listed in Table. 1.1

Of course, the properties of AlGaN are mole fraction dependent. Nonetheless, the values listed in Table. 1.1 can be considered the upper and lower limits for the

Table 1.1: Material properties corresponding to spontaneous and piezoelectric polarization for GaN and AlN

	GaN	AlN
Crystal structure	Wurtzite	Wurtzite
Lattice constant	a=3.186Å c=5.186Å	a=3.11Å c=4.98Å
Spontaneous polarization $P_{SP}(C/m^2)$	0.029	0.081
Piezoelectric coeff. (C/m^2)	$e_{31} = -0.49$ $e_{33} = 0.73$	$e_{31} = -0.60$ $e_{33} = 1.46$

corresponding properties of AlGaN.

For all four heterostructure configurations, it is only when GaN is used as the substrate that we get the maximum polarization change (assuming the same mole fraction for AlGaN material). If the growth preference is the Ga-face, the induced interface charges are positive, which aids the accumulation of electrons; while N-face growth gives negative polarization induced charges, which helps accumulate holes at the interface.

For reasons such as the effective mass for electrons being smaller than that of holes[32, 33], and the activation energy of holes being much higher than electrons[34], electrons are preferable for carriers in applications such as HEMTs. There are also other configurations of the heterostructure involving more than two layers of material[35, 36, 37], but that with GaN substrate and AlGaN film will be the core of most.

There is research indicating that the defects at the AlGaN surface act as "surface donors" with a mid-bandgap energy level. These surface donors are considered the source of the formation of the 2DEG at the interface of the heterostructure[38], and the induced interface charges are the "driving force" for this formation.

The induced positive interface charges generate an electric field pointing away from the interface. This induced electric field then bends the band alignment of the heterostructure; more specifically, bending the band in AlGaN upwards in the direction away from the interface. At the same time, this raises the energy level of the surface donors, as shown in Fig. 1.5.

With the increasing thickness of the AlGaN layer, the energy level of the surface donor is raised increasingly close to the Fermi level, until a "critical thickness" is reached when the surface donor level surpasses the Fermi level of the heterostructure. At this point the electrons of the donors are ready to be transported due to the attraction of the induced positive interface charges. These electrons are therefore accumulated at the interface, forming the 2DEG layer. This layer of 2DEG is the core of the application and operation of GaN/AlGaN heterostructure HEMTs.

The relationship between the polarization and the 2DEG layer is described in both intuitive and quantitative ways. The polarization-induced charges are, as mentioned above, the driving force of the formation of the 2DEG layer. The effect of this induced charge on the formation of the 2DEG, and the potential well of the 2DEG, together with other conditions, such as the applied gate voltage, will be thoroughly investigated.

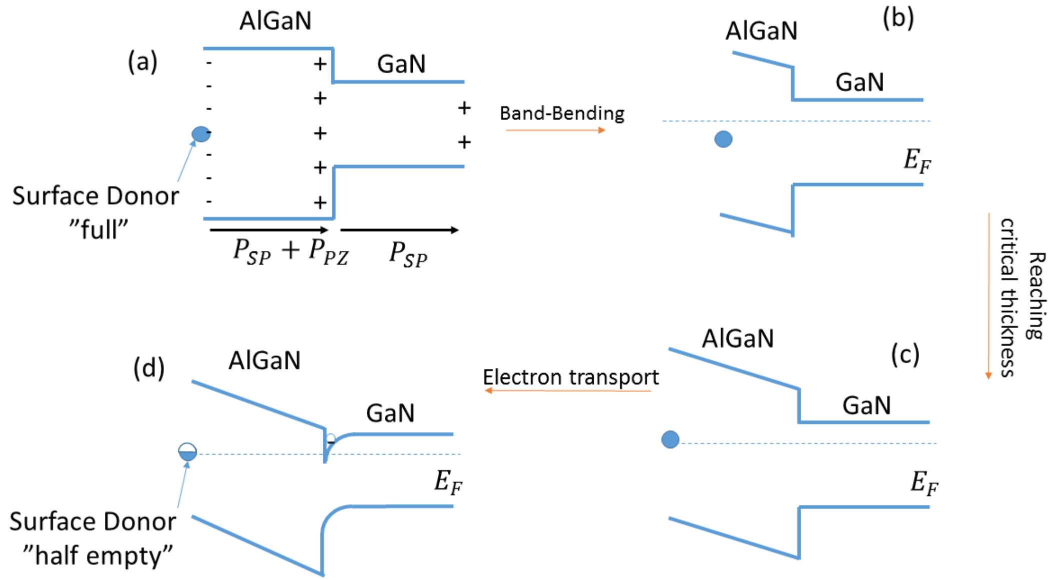

Figure 1.5: Formation of 2DEG: (a) abrupt change in polarization gives rise to induced interface and surface charges; (b) the electric field caused by the induced charges bends the band alignment of the heterostructure, making the band on the AlGaN side go upwards away from the interface. (c) When the thickness of AlGaN surpasses a "critical thickness," the energy level of the surface donors is raised high enough to pass the Fermi level of the heterostructure. (d) Electrons from the surface donor are transported towards the interface and accumulate to form a layer of electrons, called 2DEG.

1.2.2 Monte Carlo (MC) method

The MC method is usually used to investigate the electron transport properties of semiconductors. The MC method is used throughout in this work, and it is therefore introduced in the introduction as a main tool of analysis. The manner

in which the electron's state evolves under the influence of external force (electric fields), as well as internal scatterings, is simulated. The whole process is as described below:

(1) Initialize a single electron by giving a starting energy (E) and momentum ($\vec{k}$)

(2) Generate a random number (r_1) to determine the flight time during (τ) which the electron drifts before encountering a scattering event

(3) E and k evolve and sampling points are collected during the drift time

(4) At the end of the flight time, two more random numbers r_2 and r_3 are generated to determine the scattering type for the electron and the resulting angle after the scattering

(5) Repeat steps 2-4 until the predefined total flight time is reached

The process of the MC method is illustrated in Fig. 1.6.

When the MC simulation is finished, statistics such as distribution of the electron energy, distribution of the drift velocity, average electron energy, average drift velocity, and so on. can be gathered to describe the transport of the electron. By conducting a series of MC simulations under different electric fields, a graph of average velocity versus electric field can be obtained, which can be used to extract the information of the electron mobility.

There are various reports on the MC simulation on the bulk GaN[39, 40, 41] and the AlGaN/GaN heterostructure[42, 43, 44]. For the bulk MC simulation, most reports implemented a multiple-valley model, in which the electrons can be scattered into higher valleys when they gain high enough energy.

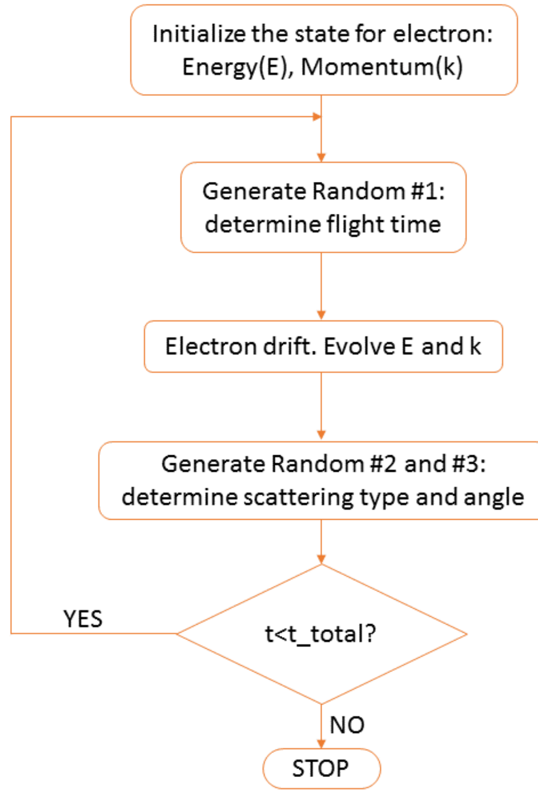

Figure 1.6: Flowchart of the single-particle MC simulation

For the heterostructure Monte Carlo simulation, previous research has tended to focus on one specific configuration, corresponding to a fixed structure of the potential well of the 2DEG. It is not mentioned in the literature to date that The alteration of the potential well itself would change the results of the MC simulation. Such research is needed because the potential well parameters are strongly dependent on the configuration and applied voltage across the heterostructure. There is thus a need for investigation of how potential well alteration changes electron transport properties.

Chapter 2

Germanium (Ge) Band Structure Calculations

In this chapter, we focus on Ge as one of our post-silicon semiconductors. We examine the basic electronic properties, where the typical starting point is usually the electronic energy band structure, which provides the electron energy versus electron wave-vector relationship. From the band structure, virtually all of the electronic properties of the material can eventually be obtained. The properties include bandgap, effective mass and density of states. As a result, virtually all electron transport properties and all optical properties are contained within the band structure. In this work, we will focus on the optical properties of Ge and how they can be engineered by physically altering the lattice structure. The change in the lattice structure gives rise to a variation in the band structure, and thus the electric and optical properties. In this chapter we perform calculations which guide the distortion of the lattice in order to change the bandgap and thus engineer the optical properties of Ge.

As is mentioned in the previous chapter, Ge is an indirect bandgap ($\sim 0.66eV$) material, but with a relatively small offset ($\sim 0.14eV$) between the direct and indirect bandgap. The bandgap of Ge makes it a candidate for photo detection in the SWIR range. However, its bandgap being indirect means the material suffers from a relatively large dark current.

By straining the material in a proper orientation, it is possible to transform Ge into a direct bandgap material. In order to analyze this transition phenomenon, EPM is utilized to calculate the band structure of Ge. EPM has relatively low computational expenses and uses parameters extracted from experimental data, thus it guarantees a reasonable agreement with experiments. To verify the method, calculation results will be compared to experimental data.

2.1 Empirical Pseudopotential Method (EPM) for Calculating Germanium (Ge) Band Structure

EPM solves the one-electron Schrödinger equation, described in Eq. 2.1:

$$\left(-\frac{\hbar^2}{2m}\nabla^2 + V(\vec{r})\right)\psi(\vec{r}) = E\psi(\vec{r}) \tag{2.1}$$

where,

$\psi(\vec{r})$ is the wave function solution for the equation

$V(\vec{r})$ is the potential experienced by the electron

E is the total energy of the electron

m is the rest mass of an electron

The method starts with the standard approach of transforming the Schrödinger equation into a system of algebraic equations [18].

Based on Bloch's theorem, the wave function of a crystal can be expressed in the form of:

$$\psi(\vec{r}) = e^{-i\vec{k}\cdot\vec{r}} \cdot u(\vec{r}) \tag{2.2}$$

where $e^{-i\vec{k}\cdot\vec{r}}$ represents a plane wave, $\vec{k}$ is the wave vector and $u(\vec{r})$ is a Bloch function with the same periodicity as the lattice. The same periodicity can also be applied to the potential term $V(\vec{r})$. Because of the periodicity, both $u(\vec{r})$ and $V(\vec{r})$ can be transformed into Fourier's series:

$$u(\vec{r}) = \sum_{\vec{G}} U(\vec{G}) e^{i\vec{G}\cdot\vec{r}} \tag{2.3}$$

$$V(\vec{r}) = \sum_{\vec{G}} V(|\vec{G}|) e^{i\vec{G}\cdot\vec{r}} \tag{2.4}$$

where:

$\vec{G}$ is the translation vector of the reciprocal lattice points;

$V(\vec{G})$ is the Fourier coefficient of the periodic potential;

$U(\vec{G})$ is the Fourier coefficient of the Bloch function.

By substituting Eq. (2.4) and Eq. (2.3) back into Eq. (2.1), the Schrödinger equation can be transformed into an algebraic equation:

$$\left[\frac{\hbar^2(\vec{k}+\vec{G})^2}{2m}\right] U(\vec{G}) + \sum_{\vec{G}'} V(|\vec{G}-\vec{G}'|) U(\vec{G}') = E\ U(\vec{G}) \tag{2.5}$$

For each individual $\vec{G}$, an equation can be constructed from Eq. 2.5. The number of equations is equal to the number of $\vec{G}$ being considered. This series of equations can be reorganized into a matrix from, which is expressed as follows:

$$
\begin{bmatrix} H_{11} & \dots & H_{1n} \\ \vdots & \ddots & \vdots \\ H_{n1} & \dots & H_{nn} \end{bmatrix} \begin{bmatrix} U(\vec{G}_1) \\ \vdots \\ U(\vec{G}_n) \end{bmatrix} = E \begin{bmatrix} U(\vec{G}_1) \\ \vdots \\ U(\vec{G}_n) \end{bmatrix} \tag{2.6}
$$

where:

$$
H_{ij} = \begin{cases} \left[\frac{\hbar^2(\vec{k}+\vec{G})^2}{2m}\right] + V(0), & i = j \\ V(|\vec{G}_i - \vec{G}_j|), & i \neq j \end{cases} \tag{2.7}
$$

By finding the determinant of this matrix equation and solving the characteristic equation, the eigenvalues (the energies) at each $\vec{k}$ point can be obtained. This process will be repeated for every $\vec{k}$ point of interest. To construct the complete band structure of Ge, all $\vec{k}$ points in the BZ, or at least the points in the irreducible wedge, need to be evaluated. Nonetheless, considering the symmetry of the BZ, a specific path that connects all the high symmetry point will be a good representative of the total band structure.

2.2 Crystal Structure for Germanium (Ge)

As mentioned above, the crystal structure for Ge is diamond, which is shown in Fig. 1.1. The three primitive lattice vectors[1] to describe a diamond crystal structure

[1] Notation: for real space and reciprocal space vectors throughout this work, the different components of the vectors are separated by commas, and are within parentheses.

are listed below:

$$a_1 = a_0(\frac{1}{2}, \frac{1}{2}, 0) \quad (2.8)$$

$$a_2 = a_0(0, \frac{1}{2}, \frac{1}{2}) \quad (2.9)$$

$$a_3 = a_0(\frac{1}{2}, 0, \frac{1}{2}) \quad (2.10)$$

where:

a_0 is the lattice constant of the conventional unit cell of Ge.

The diamond structure is constructed from a face-centered cubic crystal described by the three vectors above using an elementary pattern, which is also shown in Fig. 1.1. If the mid-point of the basis is chosen as the origin, the vectors for the elementary pattern are given in Eq. 2.11:

$$\vec{r_b} = a_0 \left(\frac{1}{8}, \frac{1}{8}, \frac{1}{8} \right) \quad (2.11)$$

At each location of r_b and $-r_b$, there is an atom. If both atoms are of the same element, the crystal is a diamond structure. If they are different elements, the crystal is a Zinc-Blende crystal.

Considering that the potential in a crystal is periodically repeated by the primitive vector, the potential can be expanded into a Fourier series of $V(\vec{G})'s$ as in Eq. 2.4, which is expressed as follows:

$$V(|\vec{G}|) = \frac{2}{\Omega} \int_{\Omega} d\vec{r}\; V(\vec{r})\, e^{i\vec{G}\cdot\vec{r}} \quad (2.12)$$

where Ω is the volume of the unit cell.

In the equation, the total potential will be expressed as the sum of the two

atoms in the elemental pattern:

$$V(\vec{r}) = V_1(\vec{r} + \vec{r_b}) + V_2(\vec{r} - \vec{r_b}) \tag{2.13}$$

where V_1 and V_2 are the potential of the nuclei of the two-atom bases, respectively.

Plug the above expression back into $V(\vec{G})$ equation:

$$\begin{aligned} V(|\vec{G}|) &= \left[V_1(|\vec{G}|)e^{-i\vec{G}\cdot\vec{r_b}} + V_2(|\vec{G}|)e^{i\vec{G}\cdot\vec{r_b}}\right]/2 \\ &= \frac{V_1(|\vec{G}|) + V_2(|\vec{G}|)}{2}\left[cos(\vec{G}\cdot\vec{r_b})\right] + \frac{V_1(|\vec{G}|) - V_2(|\vec{G}|)}{2}\left[-isin(\vec{G}\cdot\vec{r_b})\right] \\ &= V_s(|\vec{G}|)\ cos(\vec{G}\cdot\vec{r_b}) + V_a(|\vec{G}|)\ \left[-isin(\vec{G}\cdot\vec{r_b})\right] \\ &= V_s(|\vec{G}|)\ S_s + V_a(|\vec{G}|)\ S_a \end{aligned} \tag{2.14}$$

where V_s and V_a are called symmetry and anti-symmetry form factors, respectively; and S_s and S_a are called symmetry and anti-symmetry structure factors respectively for either diamond or zinc-blende structure.

For The Ge band structure calculation, $V_1 = V_2$ in Eq. 2.14. Therefore, $V_a = 0$, as there are only symmetry form factors (V_s) and symmetry structure factors (S_s) for Ge.

The first Brillouin zone (BZ) of Ge is shown in Fig. 1.2 and is presented here again in Fig. 2.1. The coordinates for the labeled high symmetry points are listed below:

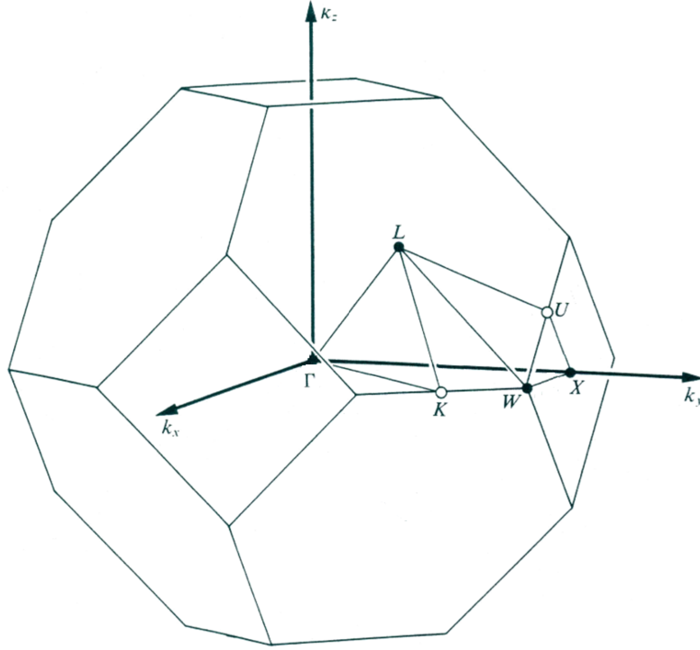

Figure 2.1: The reciprocal lattice for Ge crystal with high symmetry points labeled.

$$
\begin{aligned}
\Gamma &= (0,0,0) \\
X &= (0,\frac{2\pi}{a_0},0) \\
W &= (\frac{\pi}{a_0},\frac{2\pi}{a_0},0) \\
K &= (\frac{3\pi}{2a_0},\frac{3\pi}{2a_0},0) \\
L &= (\frac{\pi}{a_0},\frac{\pi}{a_0},\frac{\pi}{a_0})
\end{aligned}
\tag{2.15}
$$

The k-point path for the band structure calculation is selected as: L-Γ-X-K-Γ. The calculation of band structure along the high symmetry k-point path is considered a good representation of the band structure of the entire BZ.

The primitive vectors for the reciprocal lattice are as follows:

$$b_1 = \frac{4\pi}{a_0}\left(\frac{1}{2},\frac{1}{2},-\frac{1}{2}\right) \tag{2.16}$$

$$b_2 = \frac{4\pi}{a_0}\left(-\frac{1}{2},\frac{1}{2},\frac{1}{2}\right) \tag{2.17}$$

$$b_3 = \frac{4\pi}{a_0}\left(\frac{1}{2},-\frac{1}{2},\frac{1}{2}\right) \tag{2.18}$$

Therefore the $\vec{G}'s$ expressed in Eq. 2.14 can be expressed as follows:

$$\vec{G} = l \cdot b_1 + m \cdot b_2 + n \cdot b_3 \tag{2.19}$$

where: l, m, and n are integers.

Now we build on these basics and use the empirical pseudopotential to obtain the band structure for Ge.

Theoretically, to restore the wave function, required $\vec{G}'s$ are infinite; nonetheless, a cut-off of $|\vec{G}|^2$ is considered sufficient to give the wave function with enough precision. In this report's case, the cut-off is set at 11 with the unit of $(2\pi/a_0)^2$[6] [7], which includes $|\vec{G}|^2 = 0, 3, 4, 8, 11$. As an example, to get $|\vec{G}|^2 = 3$, all the possible combinations of b_1, b_2, b_3 are: b_1, b_2, b_3, $b_1 + b_2 + b_3$, $-b_1$, $-b_2$, $-b_3$, $-(b_1 + b_2 + b_3)$.

All the included $\vec{G}$'s are presented in Table 2.1. Permutations of the same family of $\vec{G}$ group are presented by one of the members in the table.

Table 2.1: $\vec{G}$ groups included in the EPM calculation of Ge band structure

$\lvert\vec{G}\rvert^2$ unit:$(2\pi/a_0)^2$	$\vec{G}$ group unit: $2\pi/a_0$	number of permutations
0	(0,0,0)	1
3	(1,1,1)	8
4	(2,0,0)	6
8	(2,2,0)	12
11	(3,1,1)	24

There are total 51 of $\vec{G}$'s included in the EPM calculation for Ge band structure. And 5 unique values for V($|\vec{G}|$) are required, which are noted V(0), V($\sqrt{3}$), V($\sqrt{4}$), V($\sqrt{8}$), V($\sqrt{11}$) for simplicity. Among the 5 required V($|\vec{G}|$)'s, $V(0)$ is essentially the overall offset of the final band structure. It won't affect the bandgaps, which are the differences between energy bands. For $V(\sqrt{4})$, the corresponding $\vec{G}$ group is the (2,0,0) family, as shown in Table 2.1. Taking $\vec{G} = 2\pi/a_0 \cdot (2,0,0)$ as an example, we can calculate the symmetry structure factor S_s, as shown below:

$$\begin{aligned} S_s &= cos(\vec{G} \cdot \vec{r_b}) \\ &= cos\left(\left(2 \cdot \frac{2\pi}{a_0}, 0, 0\right) \cdot \left(\frac{a0}{8}, \frac{a0}{8}, \frac{a0}{8}\right)\right) \\ &= cos(\frac{\pi}{2}) = 0 \end{aligned} \quad (2.20)$$

Similar calculations can be conducted on all the permutations of the $(2,0,0)$ family and the same conclusion can be drawn that the structure factor S_s associated with $V(\sqrt{4})$ is always 0. Therefore, it is unnecessary to obtain a form factor for $V(\sqrt{4})$. All the other necessary form factors are presented in Table 2.2.

By using pseudopotential rather than all electron potential, the calculation is focused on the electric properties of valence electrons, and the calculated band structure is the valence band and the conduction band for the valence electrons. By empirically selecting the appropriate values for the form factors, the EPM is considered suitable to construct the right band structure of Ge.

As mentioned previously, it is insufficient to calculate the band structure of Ge with only consideration of the local form factors, where all valence electrons feel the

same core pseudopotential. For a better approximation, a nonlocal compensation is also required to accommodate the assumption that different orbitals of electrons feel different core pseudopotentials.

The algebraic form of the Schrödinger Equation, with the inclusion of the nonlocal term, is shown below:

$$\left[\frac{\hbar^2\left(\vec{k}+\vec{G}\right)}{2m}\right]U\left(\vec{G}\right)+\sum_{\vec{G'}}\left\{\left[V\left(\vec{G}-\vec{G'}\right)+V_{ps}^{NL}\left(\vec{k},\vec{G},\vec{G'}\right)\right]U\left(\vec{G'}\right)\right\}=E\,\vec{G} \tag{2.21}$$

where V_{ps}^{NL} is the nonlocal compensation term for the EPM calculation, as expressed in Eq. 2.22 [7].

$$\begin{aligned} V_{ps}^{NL}\left(\vec{k},\vec{G},\vec{G'}\right) &= \frac{4\pi}{\Omega_a}\sum_{l} A_l(2l+1)P_l(cos\ \theta_{KK'}) \\ &\quad \times S(\vec{K}-\vec{K'})F_l(K,K') \end{aligned} \tag{2.22}$$

where:

$\vec{K}=\vec{k}+\vec{G}$ and $K=|\vec{K}|$, with units of m^{-1}

$\vec{K'}=\vec{k}+\vec{G'}$ and $K'=|\vec{K'}|$, with units of m^{-1}

$\theta_{KK'}$ is the angle between $\vec{K}$ and $\vec{K'}$

l is the angular quantum number of the core electrons

A_l is the coefficient for l, with units of J

$P_l(x)$ are Legendre polynomials

$S(\vec{G})$ is the form factor as expressed in Eq. 2.14

$F_l(K,K')$ is expressed in Eq. 2.23 as follows:

$$F_l(K,K') = \begin{cases} (1/2R_l^2)\{[j_l(KR_l)]^2 - j_{l-1}(KR_l)j_{l+1}KR_l\}, & K = K' \\ \\ R_l^2/(K^2 - K'^2)[Kj_{l+1}(KR_l)j_l(K'R_l) \\ \qquad\qquad -K'j_{l+1}(K'R_l)j_l(KR_l)]], & K \neq K' \end{cases} \tag{2.23}$$

where:

R_l is the cut-off radius of nonlocal effect;

$j_l(x)$ are spherical Bessel functions with argument of x.

In Ref [7], it is stated that only the contribution from $l = 2$ is significant for the EPM band structure calculation of Ge. Therefore, Equ. 2.22 can be simplified as:

$$\begin{aligned} V_{ps}^{NL}\left(\vec{k},\vec{G},\vec{G'}\right) &= \frac{4\pi}{\Omega_a}A_2 \cdot 5 \cdot P_2(cos\ \theta_{KK'}) \\ &\quad \times S(\vec{K}-\vec{K'})F_2(K,K') \end{aligned} \tag{2.24}$$

The nonlocal parameters for the inclusion of the nonlocal effect of the EPM calculation are also listed in Table. 2.2.

2.3 Calculation Results

The methodology for solving the one-particle Scrödinger equation is explained in the previous section. For each $\vec{k}$ point on the chosen high symmetry k-point path, a matrix equation is constructed using Eq. 2.21. The matrix equation is then

Table 2.2: Form factors for the calculation using (EPM) of Ge[6] [7].

Lattice constant	Form factors				Nonlocal parameters	
a_0	$\|\vec{G}\|^2$	3	8	11	A_2	R_2
5.658$\mathring{A}$	$V_s(\|\vec{G}\|)$	-0.23Ry	0.01Ry	0.06Ry	0.275Ry	1.22Å

solved and eigenvalues are extracted. The lowest 8 solutions of the matrix equation represent the 4 top-most valence band energy and 4 bottom-most conduction band energy for the specific $\vec{k}$ point used to construct the matrix equation. After repeating such process for all the $\vec{k}$ points on the hight symmetry k-point path, curves can be drawn to connect the eigenvalues corresponding to the save energy band, forming a band structure plot.

The calculation results of the band structure along the high symmetry k-point path mentioned above are shown in Fig. 2.2.

The simulation results indicate that Ge is an indirect band gap material with a conduction band minimum at the L point, the valence maximum at the Γ with a band gap of 0.66 eV. The direct Γ point conduction minimum has a direct bandgap of 0.8eV. The results from the calculation of the band structure are compared to experimental data and are listed in Table. 2.3.

In addition to the results along the selected k-point path, band structure calculations are also conducted on the specific 2D planes that cut through the first BZ. The planes are selected to pass through the high symmetry points displayed alongside the band structure calculation results in these various planes.

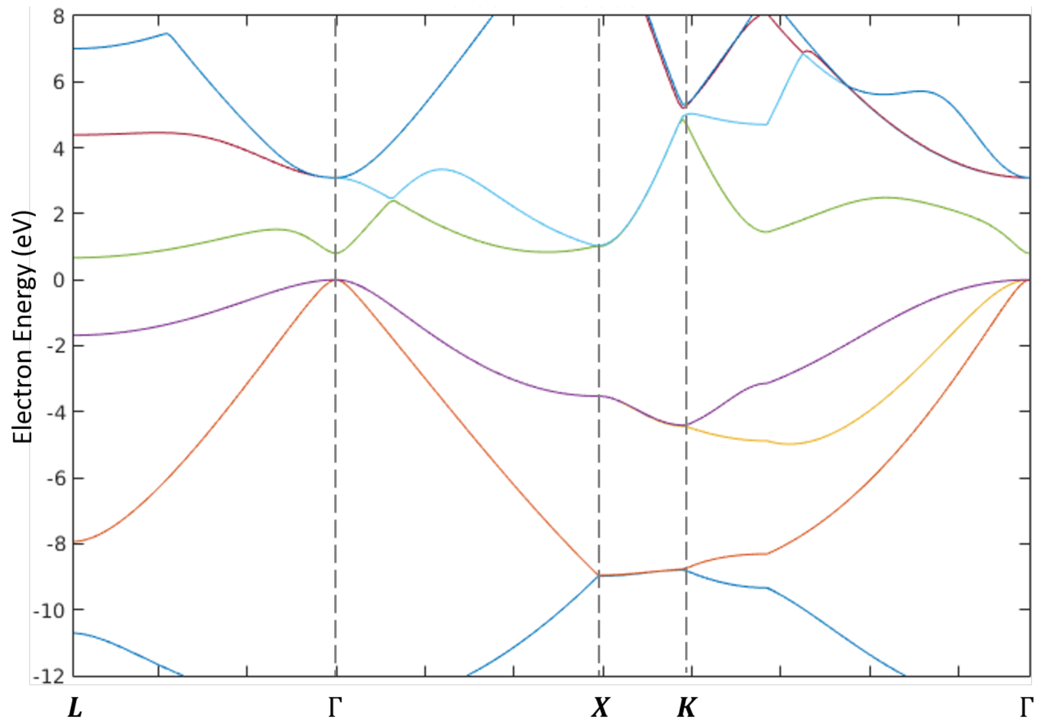

Figure 2.2: Calculation results of the band structure of Ge in this work.

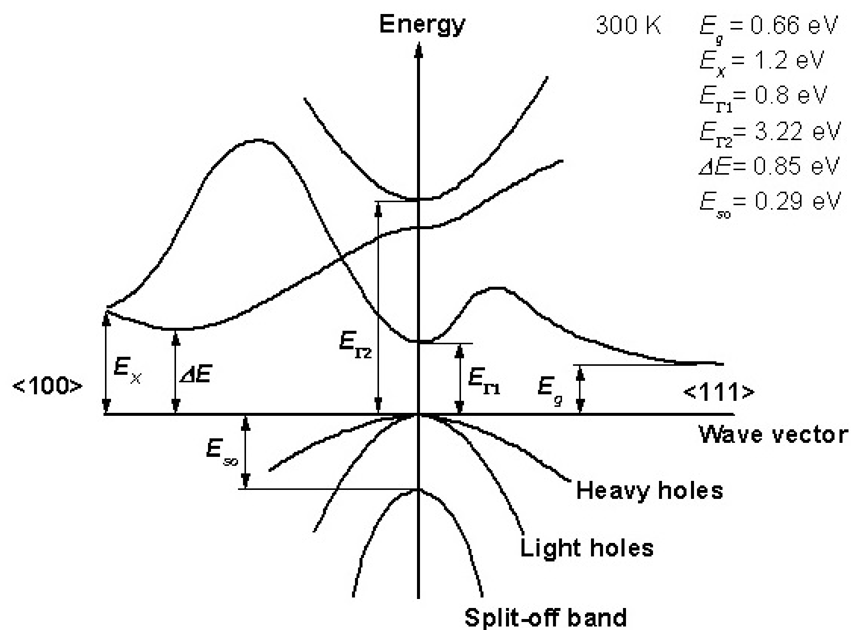

Figure 2.3: Band structure illustration for Table. 2.3 (source: http://www.ioffe.ru/SVA/NSM/Semicond/Ge/bandstr.html)

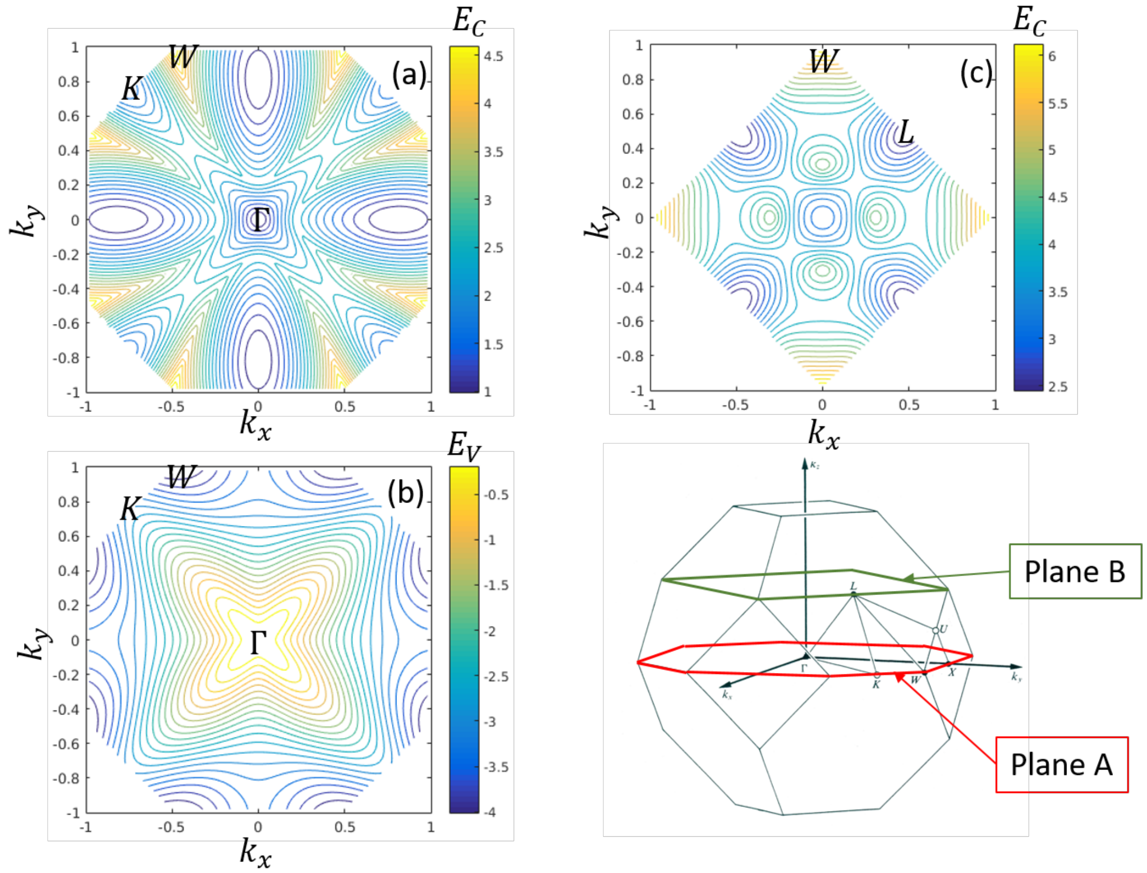

Figure 2.4: Contour of the 2D band structure of (a) the top-most valence band (TVB) and (b) bottom-most conduction band (BCB) along Plane A and (c) BCB along Plane B. The units of the axes are $2\pi/a_0$. The unit of the color bar is eV. The high symmetry points are also labeled on the band structure graph. Of all the equivalent points, only one is labeled.

Table 2.3: EPM calculation compared to experimental data and first principle calculation collected from literature. The energy levels listed below are illustrated in Fig. 2.3.

	EPM	Experiment
$E_g(eV)$	0.66	0.66
$E_{\Gamma_1}(eV)$	0.796	0.8
$E_X(eV)$	1.005	1.2
$E_{\Gamma_2}(eV)$	3.073	3.22
$\Delta E(eV)$	0.832	0.85

These calculations form the foundation for the band structure engineering which is presented in the next chapter.

Chapter 3

Germanium Band Structure Under Strain

As mentioned in previous chapters, a direct bandgap Ge is desired for the application of photo detection in the SWIR range. Straining the material is one possible method of transforming Ge from an indirect to a direct bandgap material. The band structure of Ge is subject to change when strain is applied to the lattice. Tensile strain tends to decrease both the direct ($E_{g-\Gamma}$) and indirect (E_{g-L}) bandgaps. How they change, however, depends on the type of strain applied (uniaxial, biaxial, or hydrostatic) and the orientation on which the strain is applied.

3.1 Strain Translation of Ge Crystal

Strain is the fraction of the change in the crystal lattice's dimension, from its original dimension, after deformation by an applied force. There are two coordinate systems involved in strain translation: (1) the one to describe the Ge crystal lattice (using subscripts $\overline{xyz}$) and (2) the one to directly describe the applied strain (using subscripts $\overline{x'y'z'}$). For a cubic lattice crystal such as Ge, There are three different types of strain: uniaxial, biaxial and hydrostatic, which are defined as follows:

(a) Uniaxial: the stress is applied along a certain direction, such as in a nanowire;

(b) Biaxial: the stress is applied on a certain plane, such as in a deposited film on a substrate;

(c) hydrostatic: the stress is applied equally on all three directions.

The three basic strain types can be expressed by a diagonal strain tensor:

$$\overline{\overline{\epsilon}}'(\overline{x'y'z'}) = \begin{bmatrix} \epsilon_{x'x'} & 0 & 0 \\ 0 & \epsilon_{y'y'} & 0 \\ 0 & 0 & \epsilon_{z'z'} \end{bmatrix} \tag{3.1}$$

In this expression of strain, the assignment of the x' unit vector of the $\overline{x'y'z'}$ coordinate system is dependent on the type of the strain. For uniaxial strain, the x' unit vector is assigned in the same direction as the applied strain; while for biaxial strain, it is assigned the direction perpendicular to the plane the strain is applied on. For hydrostatic strain, the $\overline{x'y'z'}$ coordinate system is assigned the same as the $\overline{xyz}$.

The two coordinates systems can also be expressed as a 3×3 matrix ($\overline{\overline{\overline{xyz}}}$ and $\overline{\overline{\overline{x'y'z'}}}$ for $\overline{xyz}$ and $\overline{x'y'z'}$). The two coordinate system matrices are connected through a translation matrix noted as $\overline{\overline{\overline{T}}}$:

$$\overline{\overline{\overline{x'y'z'}}} = \overline{\overline{\overline{T}}} \cdot \overline{\overline{\overline{xyz}}} \tag{3.2}$$

The stress tensors $\overline{\overline{\sigma}}(\overline{xyz})$ and $\overline{\overline{\sigma}}(\overline{x'y'z'})$ are also connected through the translation matrix $\overline{\overline{\overline{T}}}$:

$$\overline{\overline{\sigma}}(\overline{xyz}) = \overline{\overline{\overline{T}}}^T \cdot \overline{\overline{\sigma}}(\overline{x'y'z'}) \cdot \overline{\overline{\overline{T}}} \tag{3.3}$$

The two stress vectors both satisfy Hooke's law under their own coordinate system:

$$\vec{\sigma}(\overline{xyz}) = \overline{\overline{c}}(\overline{xyz}) \cdot \vec{\epsilon}(\overline{xyz}) \tag{3.4}$$

$$\vec{\sigma}(\overline{x'y'z'}) = \overline{\overline{c}}(\overline{x'y'z'}) \cdot \vec{\epsilon}(\overline{x'y'z'}) \tag{3.5}$$

where $\bar{\bar{c}}(\overline{xyz})$ and $\bar{\bar{c}}(\overline{x'y'z'})$ are the elastic constant matrices under coordinate systems $\overline{xyz}$ and $\overline{x'y'z'}$, respectively. The translation between the two elastic constant matrices is given in detail in Ref. [45].

3.2 Band Structure Calculation Using the Empirical Pseudopotential Method (EPM) for Strained Germanium (Ge)

The previous section described the method of translating the strain tensor ($\bar{\bar{\epsilon}}'$) from the original coordinate system to that ($\bar{\bar{\epsilon}}$) with the coordinates in which the crystal lattice is described.

Because of the applied strain, the primitive vectors ($\vec{a_1}$, $\vec{a_2}$ and $\vec{a_3}$) used to describe the original unstrained lattice are changed, as well as the vector used to describe the basis of the diamond crystal structure ($\vec{r_b}$). The change is described by the obtained $\bar{\bar{\epsilon}}'$:

$$\vec{a_i}' = (\bar{\bar{1}} + \bar{\bar{\epsilon}}) \cdot \vec{a_i} \tag{3.6}$$

$$\vec{r_b}' = (\bar{\bar{1}} + \bar{\bar{\epsilon}}) \cdot \vec{r_b} \tag{3.7}$$

where: i = 1,2,3

As the lattice vector is distorted, the reciprocal lattice will also be so. Therefore the three discrete values of $V(\vec{G})$ must expand into a continuous curve to accommodate the continuously changing $|\vec{G}|$ values under arbitrary strain. A cubic spline interpolation of the atomic form factors is used here for purpose[46], which is

Table 3.1: Coefficients for continuous form factors for EPM for Ge[47].

Parameter	Value (a.u.)	Parameter	Value (a.u.)
C_1	23.31608	C_4	0.97655
C_2	2.50648	C_5	5.0
C_3	0.63901	C_6	0.3

described as follows:

$$V(|\vec{G}|) = \frac{1}{\Omega_a} \frac{C_1(|\vec{G}|^2 - C_2)}{exp\left[C_3(|\vec{G}|^2 - C_4) - 1\right]} \left[\frac{1}{2} tanh\left(\frac{C_5 - |\vec{G}|^2}{C_6}\right) + \frac{1}{2}\right] \quad (3.8)$$

where:

C_1-C_6 are fitting parameters.

Ω_a is the volume of the primitive cell.

The coefficients mentioned in Eq. 3.8 are listed in Table 3.1.

3.3 Results and Analysis

3.3.1 Strain Along Commonly Used Orientations

The calculations are first conducted on the commonly used orientations of the three basic strain types. In the example in Fig. 3.1, the direct-indirect bandgap transition happens with the right type of strain and a sufficient amount of it. (This transition is when the Ge transforms from an indirect to a direct bandgap semiconductor after the proper strain is applied.) As shown in Fig. 3.1 by the dashed/double-dotted curve, the original unstrained band structure has an indirect bandgap, with the L valley lower than the Γ valley. When a 1.7% tensile strain is

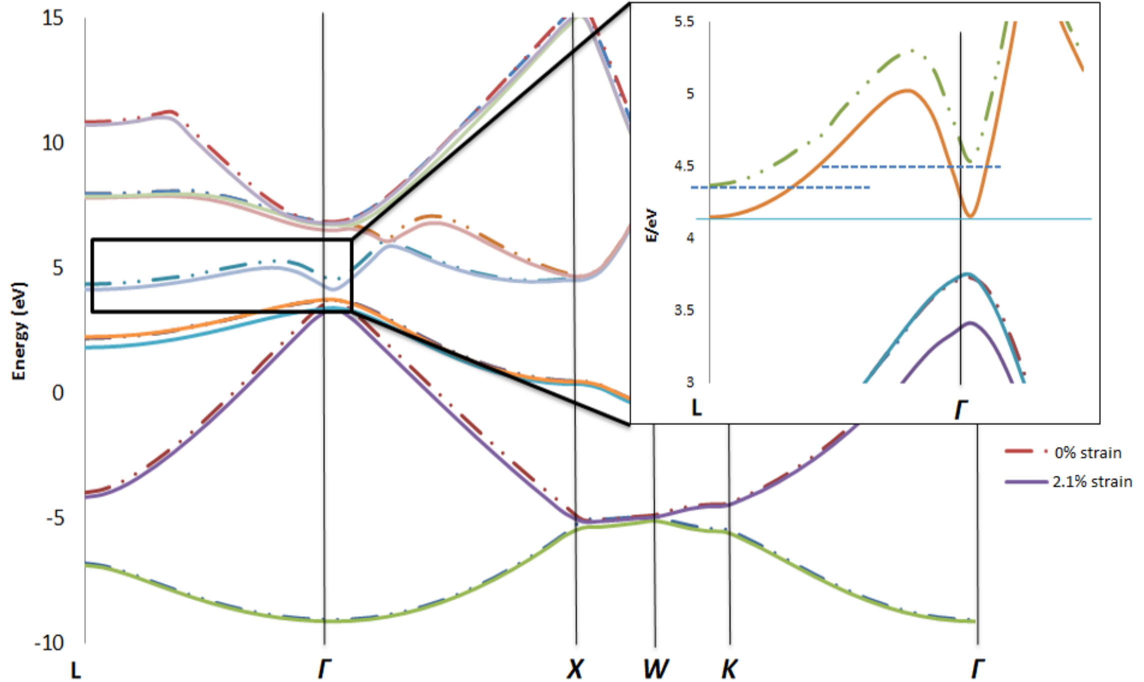

Figure 3.1: Band structure of Ge. Dashed/double-dotted line is for 0 % strain; Solid line is for biaxial strain of 1.7% on {100} plane.

applied on the {100} plane, it can be observed on the graph that both valleys are pushed downwards, though the Γ valley is pushed further than the L valley. With this amount of the strain, the Γ valley reaches the same level as the L valley. This is the point at which Ge transforms from indirect bandgap material to direct bandgap material. It is worth pointing out that in Ref. [1], a biaxial strain of 2.33% on a {100} plane is achieved, making the 1.7% strain required for the transition feasible in real application.

In Table 3.2, the calculation results are presented for the commonly used orientation. In Table 3.2, strain at transition point (STP) and bandgap at transtion point (BTP) are defined as "N/A" when no amount of strain will be sufficient enough to achieve the indirect-direct transition before the bandgap decreases to zero and/or

Table 3.2: Calculation results of strained Ge and comparison with reported values: STP and BTP.

Orientation	STP	BTP	Reported STP	Reported BTP
Uniaxial				
⟨100⟩	6.2%	0.29eV		
⟨110⟩	N/A	N/A		
⟨111⟩	3.7%	0.50eV	4.2%[62]	0.34eV[62]
Biaxial				
{100}	1.7%	0.49eV	2%[63], 1.7%[1]	0.48eV[63], 0.47eV[1]
{110}	2.1%	0.45eV		
{111}	4.0%	0.10eV		
Hydrostatic				
	0.86%	0.636eV		

L valley is pushed below valence band maximum along the specific orientation.

Of the three types of strain, hydrostatic strain is preferred, because the transition can be achieved with the lowest amount of strain and the remaining bandgap very much preserved. However, the major problem lies in how to engineer this kind of strain, given that the tensile strain is required in all directions, thus the material must be stretched in all directions at once.

For the other two types, the application of the strain can be engineered practically. Biaxial strain can be applied on a film if it is deposited on a substrate with a larger lattice constant[52] or through the fabrication of nanomembranes[1]. In addition, the film needs to be thin enough before the strain is released through the

formation of dislocations. The fabrication of nano wires gives rise to the possibility of applying uniaxial strain to a material[53].

3.3.2 Strain Along Arbitrary Orientation

As mentioned in Chapter 1, a Si substrate is not perfectly cut along a chosen orientation (such as a {100} plane), but cut with a miscut angle. This miscut angle passes onto the grown structure atop; in our case, a Ge layer or nanowire. The engineered applied strain on the Ge epilayer is subsequently misaligned with the chosen orientation. The effect of this alignment on the indirect-direct bandgap transition phenomenon will be investigated in this section.

hydrostatic strain is the only one of the three types of strain (uniaxial, biaxial and hydrostatic) to have a uniform strain along all directions; thus, only uniaxial and biaxial strain are considered in terms for the effect of arbitrary orientation.

To visualize the arbitrary orientation more easily, a projection of the Miller indices of the orientation is applied.

Taking uniaxial strain as an example, the Miller index of any arbitrary direction is expressed by a combination of three integers, noted as $\langle lmn \rangle$. Considering the symmetry of the Ge crystal, it is reasonable to assign to n the maximum absolute value of l,m, and n, as expressed as follows:

$$max(|l|, |m|, |n|) = |n| \tag{3.9}$$

The Miller index of this arbitrary direction can now be rewritten:

$$\frac{\langle lmn \rangle}{max(l,m,n)} = \frac{\langle lmn \rangle}{n} = \langle \frac{l}{n} \frac{m}{n} 1 \rangle \tag{3.10}$$

where:

$$\begin{aligned} -1 \leq \frac{l}{n} &\leq 1 \\ -1 \leq \frac{m}{n} &\leq 1 \end{aligned} \tag{3.11}$$

After applying the aforementioned method, any arbitrary direction can be projected onto a plane as shown in Fig. 3.2. After the projection, the first two numbers of the indices will be the coordinates in the square, and the third number will always be 1. To be more specific, the center of the square corresponds to the $\langle 001 \rangle$ family, the corners correspond to the $\langle 111 \rangle$ family, while the mid-points of the sides correspond to the $\langle 011 \rangle$ family. Finally, the shaded triangle in the figure is the irreducible wedge of all the unique orientations. Therefore, all other points in the square can be represented by the points in the shaded triangle and be treated as a family (e.g. [124], [214], $[\bar{1}24]$, $[1\bar{2}4]$ and so on, all belong to the family $\langle 124 \rangle$).

The same analogy can be applied to Miller indices for planes. Several examples of the projection are illustrated in Fig. 3.3.

Similarly, the center of the square corresponds to the $\{0,0,1\}$ family, the corners correspond to the $\{1,1,1\}$ family, while the mid-points of the sides correspond to the $\{0,1,1\}$ family.

Using the method described above, the BTP and STP under uniaxial strain and biaxial strain under arbitrary orientation are calculated. The results are mapped

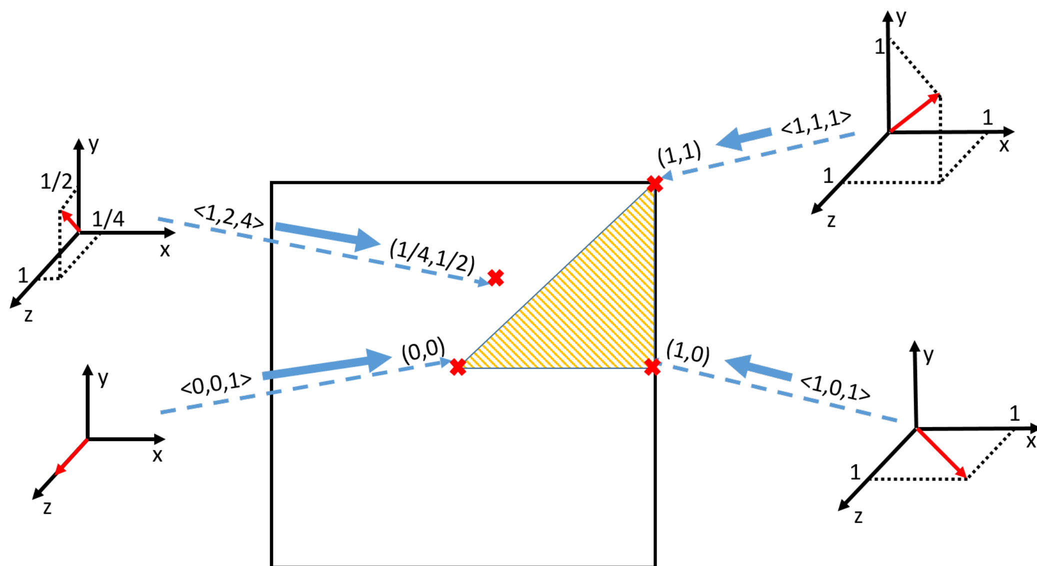

Figure 3.2: Projection from Miller indices for directions of 2D coordinates inside a square with the range of $-1 \leq x \leq 1$ and $-1 \leq y \leq 1$. Several examples of the projection are also illustrated.

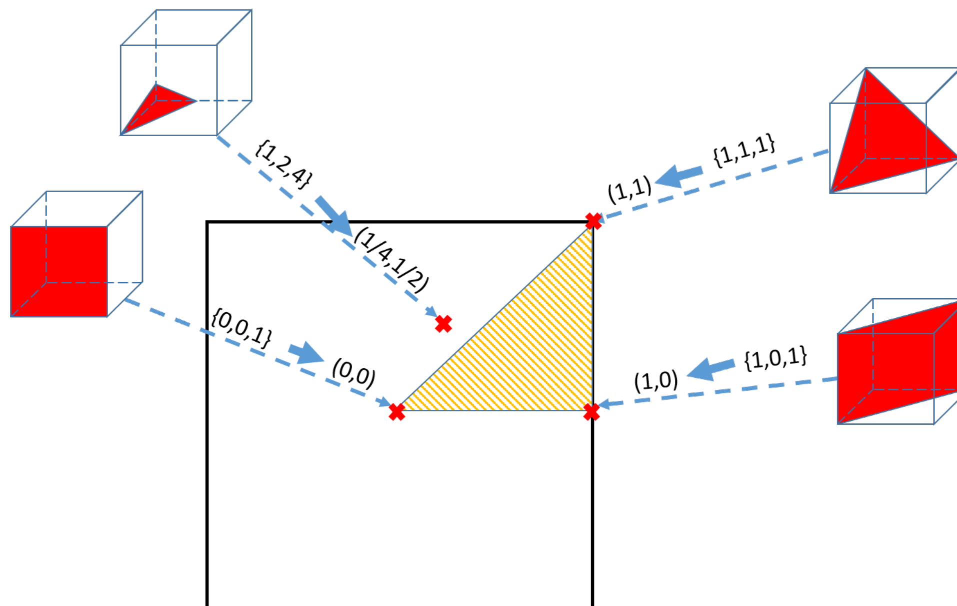

Figure 3.3: Projection from Miller Indices for planes to 2D coordinates inside a square with the range of $-1 \leq x \leq 1$ and $-1 \leq y \leq 1$. Several examples of the projection are also illustrated.

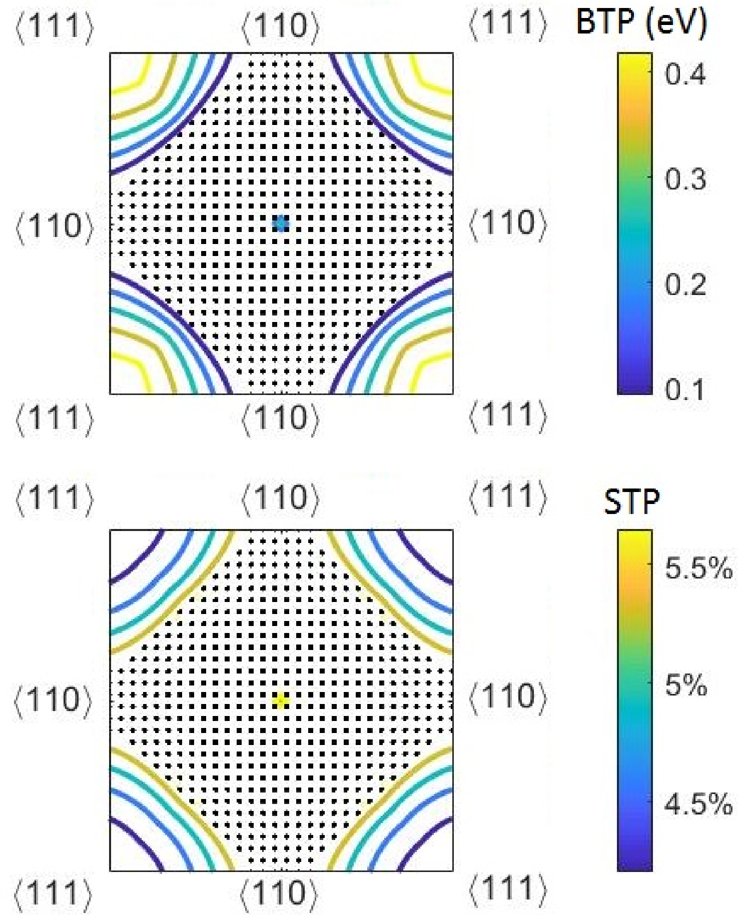

Figure 3.4: BTP and STP vs. different orientations of the plane under uniaxial strain. The values of the contour curve represent the values of BTP (top) or STP (bottom) at the orientation represented by the coordinates of the point. The unit for BTP is eV. The center of the graph has the Miller index of $\langle 001 \rangle$.

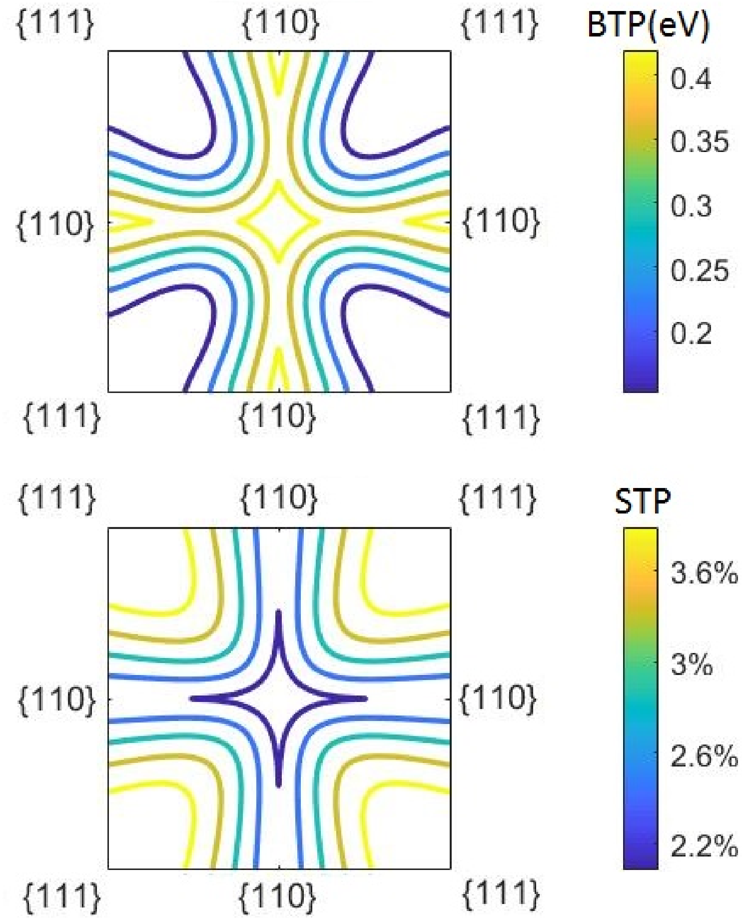

Figure 3.5: BTP and STP vs. different orientations of the crystal direction under biaxial strain. The values of the contour curve represent the value of BTP (top) or STP (bottom) at the orientation represented by the coordinates of the point. The unit for BTP is eV. The center of the graph has the Miller index of {001}.

onto a contour graph on a square ranging from $-1 \leq x \leq 1$ and $-1 \leq y \leq 1$. The simulation results are shown in Fig. 3.4 and Fig. 3.5.

The simulation results displayed in Fig. 3.4 and Fig.3.5 also show the optimal orientations for both biaxial and uniaxial strain cases, as discussed in the previous section. $\langle 111 \rangle$ is the optimal direction for applying uniaxial strain to achieve the transition, and $\{100\}$ is the optimal plane for applying biaxial to achieve the transition. Additionally, the dotted region in Fig. 3.4 means that the orientation represented by the coordinates in the region cannot achieve the indirect-direct transition before either the direct or the indirect bandgap hits zero.

For both uniaxial and biaxial cases, the transition at the optimal orientation is sensitive to any misalignment, as evidenced by the STP increasing and the BTP decreasing with rather noticeable slopes in Fig. 3.4 and Fig. 3.5 when the point moves away from the optimal orientation. To quantify this change, Fig. 3.6 and Fig. 3.7 are plotted using the results from Fig. 3.4 and Fig. 3.5.

Fig. 3.6 contains the calculated BTP and STP values on the specific path in Fig. 3.4. The x axis of the plot in Fig. 3.6 represents the selected path of the directions ($\langle 100 \rangle$-$\langle 111 \rangle$-$\langle 110 \rangle$), where $\langle 111 \rangle$ is the optimal direction for achieving the transition for applying uniaxial strain. When tilting from the optimal direction of $\langle 111 \rangle$ towards $\langle 100 \rangle$, the average slopes of BTP and STP are 19.8meV/degree and 0.138%/degree, with a cutoff angle of approximately 25.0°. When tilting from $\langle 111 \rangle$ towards $\langle 110 \rangle$, the average slopes of BTP and STP versus angle are approximately 17.6meV/degree and 0.117%/degree, with the cutoff angle of 28.1°. At the $\langle 100 \rangle$ direction, the material is expected to achieve the transition at the strain level of

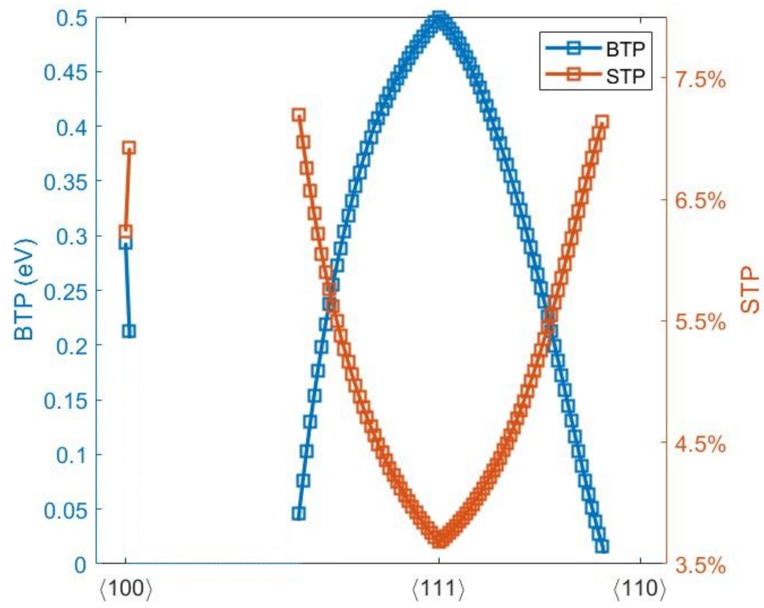

Figure 3.6: BTP and STP under uniaxial strain on path $\langle 100\rangle$-$\langle 111\rangle$-$\langle 110\rangle$. $\langle 111\rangle$ is the optimal direction for achieving the indirect-direct transition for applying uniaxial strain.

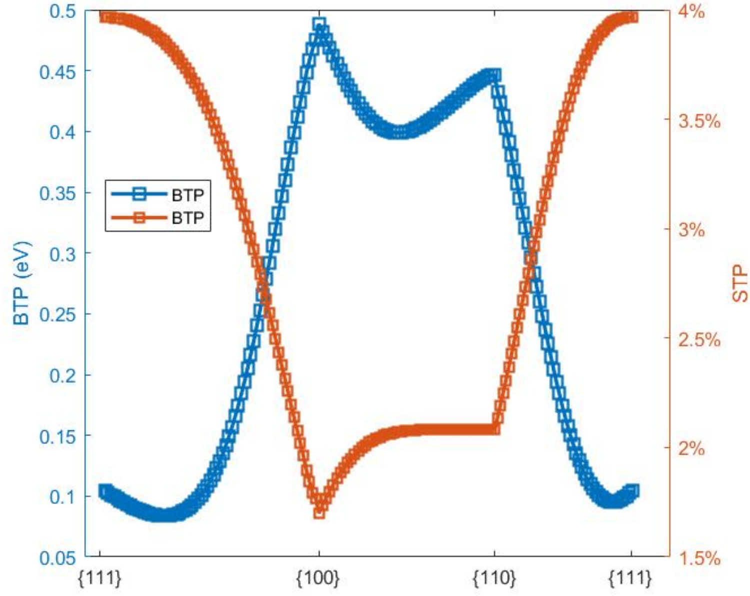

Figure 3.7: BTP and STP under biaxial strain on path {111}-{100}-{110}. {100} is the optimal plane for achieving the indirect-direct transition for applying biaxial strain.

8.28% and a BTP of 0.123 eV. However, this transition point behaves as an isolated point on the curve in Fig. 3.6. This means that the transition phenomenon at this direction is extremely sensitive to misalignment.

Fig. 3.7 contains the calculated BTP and STP values on the specific path in Fig. 3.5. The x axis in Fig. 3.7 represents the selected path of the directions {111}-{100}-{110}, where {100} is the optimal direction for achieving the transition for applying uniaxial strain. When tilting from the optimal direction {100} towards {111}, the average slopes of BTP and STP are 15.3meV/degree and 0.076%/degree. When tilting from {100} towards {110}, the average slopes of BTP and STP versus angle are approximately 9.9 meV/degree and 0.049%/degree. In contrast to the uniaxial cases, when biaxial strain is applied to any arbitrary plane, the material is

expected to produce the indirect-direct transition at sufficient amount of strain.

Both uniaxial and biaxial strain cases share some similarities with the indirect-direct transition phenomenon around the optimal orientation, which has a relatively high sensitivity to the misalignment with respect to optimal orientation. Nonetheless, in the biaxial strain case, if the applied plane is not chosen as the optimal $\{100\}$ plane, but the $\{110\}$ plane, then the transition curve of BTP and STP, as is shown in Figure. 3.7, is relatively smooth and flat around the $\{110\}$ point, indicating a rather high resistance against the possible misalignment along this specific orientation. In addition, the BTP at $\{110\}$ is only 0.02eV smaller than that of $\{100\}$ and the STP at $\{110\}$ is only 0.3% higher than that of $\{100\}$. The sacrifice is minimum to switch the plane to apply the biaxial strain on $\{110\}$ rather than $\{100\}$ to gain a better stability of the indirect-direct transition phenomenon.

Chapter 4

Band Structure of Germanium-Tin (GeSn) alloy

Other than applying strain to Ge to transform it from an indirect bandgap material to a direct material, this transition can also be achieved by alloying Ge with Sn.

The band structure of a GeSn alloy is considered a deviation from the band structure of a pure Ge material, with two factors contributing to the change: 1) the change of the lattice constant of the alloy from pure Ge in the form of hydrostatic strain, and 2) the change of the potential resulting from the alloying of Sn atoms into Ge materials.

As discussed and showed in the previous chapter, the EPM can provide accurate bandgaps once a proper pseudopotential is determined. The EPM is able to provide the correct bandgap energy for group IV crystalline materials, including Ge and Sn[6]. In this chapter, we build on the success of the EPM and present a method that combines EPM and strain and perturbation theory. This approach calculates the band structure of the Ge-Sn alloy and the influence of the fraction of Sn on the bandgap.

In this method, we take advantage of the efficient computational requirement of the EPM. The change of the lattice constant of the alloy is included in the EPM calculation as a form of hydrostatic strain. The EPM calculation gives the band

Table 4.1: Form factors for the calculation using EPM of Sn. $|\vec{G}|^2$ are in unit of $(2\pi/a_{Sn})^2$, where a_{Sn} is the lattice constant of Sn[7].

lattice constant	Form factor			
a_{Sn}	$\vert\vec{G}\vert^2$	3	8	11
6.489$\AA$	$V_s(\vert\vec{G}\vert)$	-0.19Ry	0.008Ry	0.04Ry

structure and wave functions of the alloy under the effects of strain. In addition, we treat the difference in the potential introduced by Sn as a perturbation of the system. By comparing the energy difference resulting from the combination of changing lattice constant and potential perturbation, the relationship between the bandgap and the fraction of Sn in the alloy can be obtained.

4.1 Band Structure Calculation for Germanium (Ge) and Tin (Sn) using the Empirical Pseudopotential Method (EPM)

The band structure calculation of Ge is conducted in Chapter 2 and the result is shown again here in Fig. 4.1 (top).

By utilizing the EPM described in Chapter 2, we can perform the band structure calculation on Sn using the form factors listed in Table 4.1. The calculated band structure for Sn is presented in Fig. 4.1 (bottom).

As shown in Fig. 4.1, Ge is an indirect bandgap material with the conduction band minimum located at the L point; while Sn is a semiconductor with zero bandgap, with the conduction band minimum in touch with the valence band maximum at the Γ point, while the conduction at the L point is still above that at the

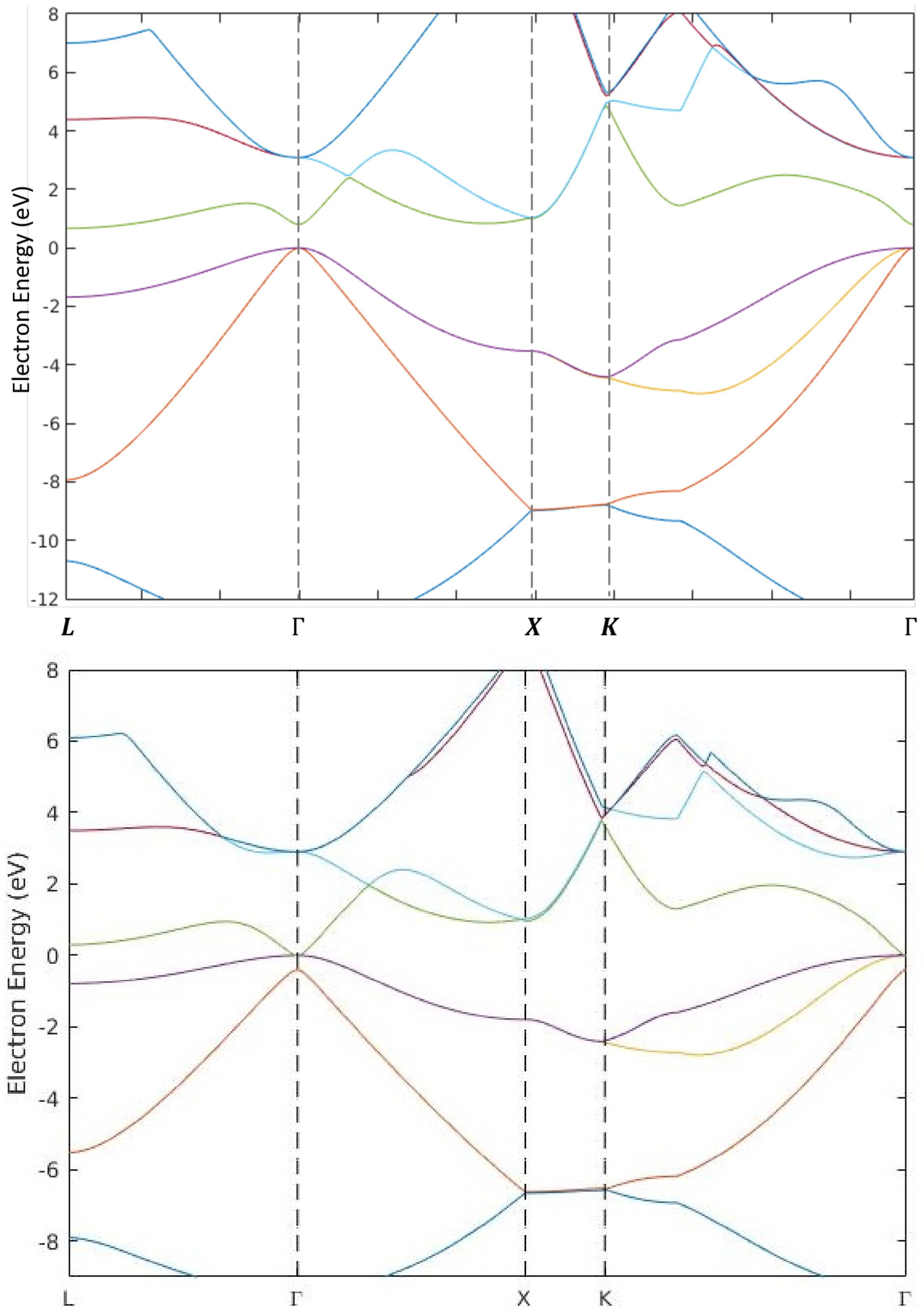

Figure 4.1: Top: Calculation results of the band structure of Sn. Bottom: Calculation results of the band structure of Ge.

Γ point. The sharp point of the conduction band minimum at the Γ point in the Sn material is expected to lower the conduction band at the Γ point in Ge by alloying Ge with Sn. Intuitively speaking, with an increasing Sn fraction, the Γ point in the conduction band of the Ge band structure will eventually become lower in energy than the L point in the conduction band, thus making Ge-Sn alloy a direct bandgap material.

4.2 Volume Change for Germanium-Tin (GeSn) alloy

We first consider the effect of the introduction of volume change on the alloy band structure.

Sn alloyed with Ge causes a change in the lattice constant, which introduces a volume change to the crystal. Vagard's Law states that the lattice constant of an alloy is a linear interpolation of the two component elements with respect to their mole fraction. Practically, there is a deviation from this linear interpolation and a second order correction is necessary to accurately describe the lattice constant of the alloy[14, 19]. The relationship between the lattice constant of GeSn and χ, where χ is a fraction of Sn to the total number of atoms in the alloy, is expressed as[17]:

$$a_{GeSn}(\chi) = a_{Ge} \cdot (1 - \chi) + \theta \cdot \chi(1 - \chi) + a_{Sn} \cdot \chi \tag{4.1}$$

where θ is called the bowing parameter, which is the coefficient for the second order correction for Vegard's Law.

The change in lattice constant is present in all directions in the crystal. Thus

this change can be expressed in the form of a hydrostatic strain, which is given in Eq. (4.2) and Eq. (4.3). As well as the mole fraction of Sn, the bowing parameter θ also determines the strain, which is a coefficient for the second order correction to the linear approximation of the change in lattice constant with respect to χ. However, different values of the bowing parameter are found in the literature. Those extracted from experiments range from 0.00882Å [17] to 0.221Å[19]. There are also various published bowing parameter values based on first principle calculations[48].

Variation in published bowing parameters exists, despite the use of the same growth method (as in Ref. [17] and Ref. [19]) or calculation method (as in Ref. [48] and Ref. [49]). The reason for this variation is unknown. In Table 4.2, some published bowing parameters are presented alongside the method used to obtain the values.

Because of the wide range of values reported for different measurements and calculation methods, we treat the bowing parameter as an independent quantity in the band structure calculations of the Ge-Sn alloy. Thus, in addition to ascertaining the effects of Sn concentration on Ge bandgap, we also used our work to evaluate the proposed values of the bowing parameter. The lattice constant $a_{GeSn}(\chi)$ in Eq. (4.1) is therefore re-expressed as $a_{GeSn}(\chi, \theta)$.

The volume change is expressed in the form of hydrostatic strain, the tensor form of which can be expressed as follows:

Table 4.2: Reported bowing parameter (θ) and the corresponding used method.

Bowing Parameter(Å)	Fabrication/Calculation Method
0	Vegard's Law Chemical Vapor Deposition (CVD)[50]
0.00882	Molecular Beam Epitaxy (MBE)[17]
0.0713	DFT calculation with Local Density Approximation (LDA)[48]
0.166	CVD[14]
0.211	MBE[19]
0.3	LDA DFT calculation[49]

$$\bar{\bar{\epsilon}}(\chi, \theta) = \begin{pmatrix} \epsilon_{xx}(\chi, \theta) & 0 & 0 \\ 0 & \epsilon_{yy}(\chi, \theta) & 0 \\ 0 & 0 & \epsilon_{zz}(\chi, \theta) \end{pmatrix} \tag{4.2}$$

where,

$$\epsilon_{xx}(\chi, \theta) = \epsilon_{yy}(\chi, \theta) = \epsilon_{zz}(\chi, \theta) = \frac{a_{GeSn}(\chi, \theta) - a_{Ge}}{a_{Ge}} \tag{4.3}$$

The strain tensor $\bar{\bar{\epsilon}}$ is, therefore, also a function of parameters χ and θ. As a result of the strain, the lattice is distorted. Subsequently, the lattice vectors ($\vec{a}_{1,2,3}$) and reciprocal lattice vectors ($\vec{b}_{1,2,3}$) change accordingly. The changes in both sets of vectors are expressed in Eq. (4.4) and Eq. (4.5).

$$\vec{a'}_{1,2,3}(\chi,\theta) = (1+\bar{\bar{\epsilon}}(\chi,\theta))\,\vec{a}_{1,2,3} \quad (4.4)$$

$$\vec{b'}_{1,2,3}(\chi,\theta) = 2\pi\frac{\vec{a'}_{2,3,1}\times\vec{a'}_{3,1,2}}{\vec{a'}_{1,2,3}\cdot(\vec{a'}_{2,3,1}\times\vec{a'}_{3,1,2})} \quad (4.5)$$

4.3 Accounting for Potential Energy Changed from Tin (Sn) Substitution

In addition to changing volume, substituting Sn atoms for a fraction of the Ge atoms will also change the potential energy of the valence electrons due to their different nuclear and electronic charges.

Previous research highlights that approximately 90% of Sn is alloyed into Ge substitutionally[19]. Therefore, the perturbation resulting from the substitution of Sn is actually the potential difference between a Ge atom and a Sn atom at one Ge site in the lattice. For the first order perturbation theory described above to work, the pseudo-potentials of a single Ge atom and a single Sn atom are needed. As both Ge and Sn are in group IV, and the pseudo-potential method is adequate to produce the right information about the energy band structure, the perturbation is considered to be the pseudo-potential difference between Ge and Sn.

Tables 2.2 and 4.1 give the form factors needed to calculate the band structure of both Ge and Sn. These form factors are essentially the Fourier coefficients due to the periodicity of the zinc-blende structure for Ge and Sn, which can thus be used to reconstruct the space dependent pseudopotential of the crystal. However, the space dependent pseudopotential extracted through the "inverse" Fourier transformation

can only give the pseudopotential of the periodic crystal. In order for our method to work, we need to reconstruct the space dependent pseudopotential for just a single atom from the periodic pseudopotential, so that we can extract the difference between a single Ge atom and a single Sn atom. This difference can then be treated as the perturbation to a pure Ge crystal.

4.3.1 Genetic Algorithm for Single Atom Pseudopotential

The single atom pseudopotential is obtained by applying a genetic algorithm. The flowchart for implementing this is shown in Fig. 4.2.

The genetic algorithm mimics life's evolutionary process. The ”life” tested in the ”environment” is a single atom pseudopotential. The ”environment” that ”life” depends on to survive is the space-dependent pseudopotential of the crystal. The chosen process is evaluated by a fitness parameter, which determines the extent to which a ”life” is adapted to the ”environment”. After the chosen process, the parent ”lives” are to pass on their DNA to the next generation of ”lives”. The probability of a parent's DNA being passed onto its child is determined by the fitness parameter. The higher the fitness, the greater the probability of having its DNA passed on. A single atom pseudopotential is discretized by sampling the pseudopotential at equal intervals, from the nucleus to a cutoff radius. This set of sampled pseudopotential is considered its ”DNA”.

A more detailed description is listed below:

Step 1: The first step of the genetic algorithm is to initialize a large pool of in-

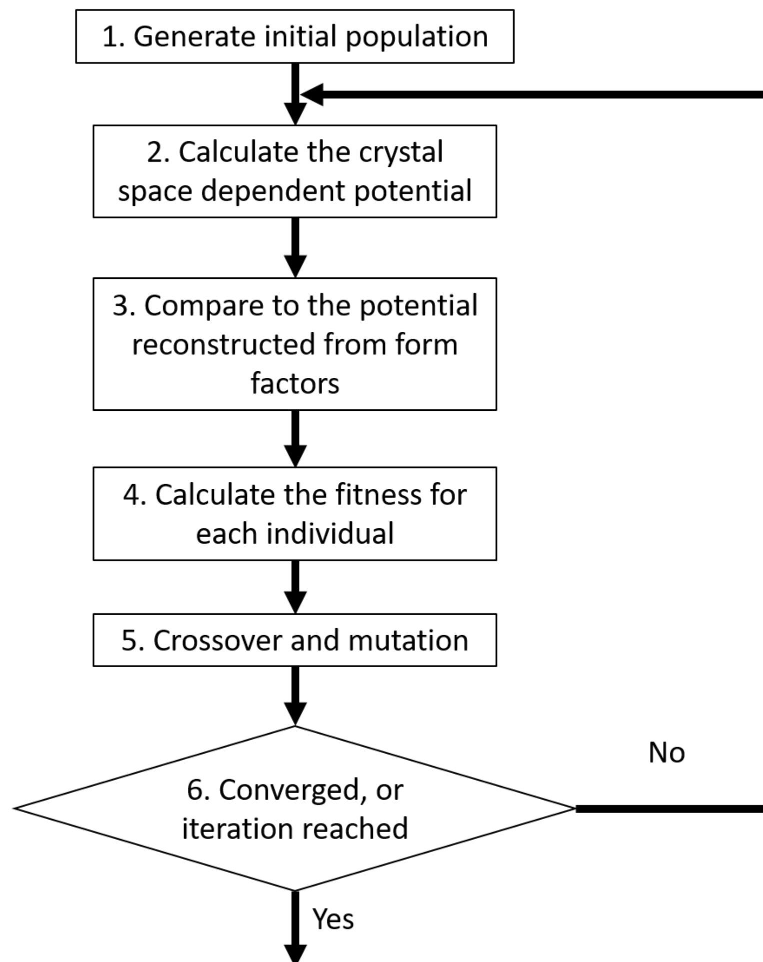

Figure 4.2: Flowchart of the genetic algorithm for extracting single atom pseudopotential.

dividuals with randomized DNA series. The bigger the pool, the greater the variety, which gives a better chance for the species to find its best fit to the environment. Too large of a pool will slow down the evolution process. However, if a pool is too small, although the process is faster, the initial variety of DNA will put a constraint on the speed of convergence. In this simulation, an initial population of 1000 is chosen.

Step 2: Each single atom potential is used to calculate the crystal potential. The crystal lattice is discretized within the primitive zone using a $20 \times 20 \times 20$ mesh. At each mesh point, the total potential is the sum of the single atom potentials of all nearby atoms within the cut-off radius. For atoms beyond the cut-off radius, their potential is considered to be zero. In this simulation, the cut-off radius is chosen as the lattice constant of the Ge crystal.

Step 3: The calculated crystal potentials are compared to the testing crystal potential calculated using the form factors at each mesh point.

Step 4: The inverse of the sum of the total absolute value of the difference between the two crystals' potentials is calculated and treated as the fitness parameter for each individual. All fitness parameters are normalized to the sum of the fitness parameters of each member of the population.

Step 5: During the crossover process, the normalized fitness parameter is the probability of the member to be selected as a parent. For each child, two parents are randomly chosen based on their fitness parameters. The "DNA" for the child is the average of both parents' "DNA". To increase the variety of the "DNA" pool, each inherited child has a possibility of its "DNA" being mutated. For this

simulation, a mutation rate of 10% is selected. To increase the convergence of the simulation, the mutation method at first is chosen as each gene of the "DNA" will be altered randomly between 0 and 0.1 eV. Later on when the simulation is close to convergence, the method will be changed to that only one gene of the "DNA" is altered by 0.01eV every time.

Step 6: After each iteration, the convergence criteria are tested. If the criteria are met, the simulation is terminated. If not, steps 2 - 6 are repeated until convergence or maximum iteration. For this simulation, the convergence criterion is chosen that the maximum difference between the calculated crystal potentials and the testing crystal potentials at all the mesh points is below 0.5 eV.

During the process described above, the single-atom pseudopotentials for Ge and Sn are obtained, respectively. The RMS values for the differences are 0.77meV for Ge lattice and 0.82meV for Sn lattice. Fig. 4.3 presents the pseudopotentials of Ge and Sn as well as the difference between the two (ΔV).

4.3.2 First-Order Perturbation Theory Accounting for Potential Energy Changed from Tin (Sn) Substitution

For an unperturbed Hamiltonian H_0, the time-independent Schrödinger equation gives rise to a series of eigenstates $\phi_n^{(0)}$ with corresponding eigenvalues $E_n^{(0)}$, where the superscript (0) indicates quantities that are for the unperturbed system, as seen in Eq. (4.6). After the introduction of the perturbation ΔV, the first-order correction to the unperturbed energy can be calculated using first-order perturba-

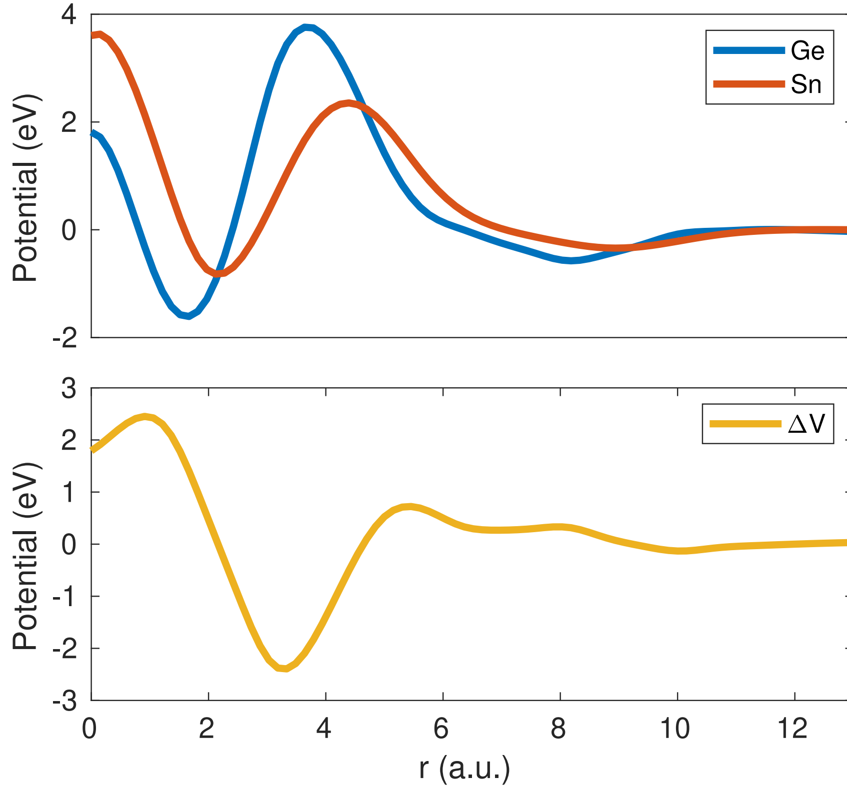

Figure 4.3: Pseudo-potential of Ge and Sn and the potential difference between Sn and Ge (ΔV) versus radial distance from the nucleus.

tion theory, in the form of Eq. (4.7).

$$E_n^{(0)} = \langle \phi_n^{(0)} | H_0 | \phi_n^{(0)} \rangle \tag{4.6}$$

$$E_n^{(1)} = \langle \phi_n^{(0)} | \Delta V | \phi_n^{(0)} \rangle \tag{4.7}$$

The wave function (namely $\phi_n^{(0)}$) needed in Eq. (4.7) is obtained by solving Eq. (2.5), using EPM with the lattice constant a_{GeSn} adjusted according to Eq. (4.1) with specified mole fraction χ and bowing parameter θ. Eq. (2.5) is solved at k-points in the first BZ, which gives $E_n^0(k)$ and $\phi_n^0(k)$. The obtained wave function $\phi_n^{(0)}$

and the extracted perturbation ΔV are then substituted in Eq. (4.7) to calculate the energy difference resulting from the perturbation. The solution coming out of Eq. (4.7) is an energy shift in the unperturbed band structure.

4.4 Results and Analysis

The substitution of Sn atoms into the Ge lattice influences the band structure, which mainly consists of two parts: 1) the induced hydrostatic "strain" caused by the volume change and 2) the potential difference between a Sn atom and a Ge atom at each Ge substitutional site in the crystal.

4.4.1 Volume Change

The relationships between the energy bandgaps (both direct and indirect) and the hydrostatic strain are shown in Fig. 4.4, where the intercept of the two curves indicates the indirect-direct bandgap transition.

As shown in Fig. 4.4, both direct and indirect bandgaps decrease with increasing hydrostatic strain (or volume change in our case). Intuitively speaking, the increased volume due to the alloying of Sn causes the separation between Ge atoms to be bigger. The bigger spacing between atoms results in more loosely bound valence electrons and thus a smaller bandgap. We calculated the bandgap, including the effects of volume change, using the method described previously in this chapter. From the calculations, we observe that the indirect-direct transition is expected to occur at a strain level of 0.86% (corresponding to the intercept of the two curves).

As mentioned above, the bowing parameter may differ from sample to sample, which results in the difference in Sn fraction required to achieve this specific volume change (the "induced" hydrostatic strain). In Fig. 4.4(inset), the fraction of alloyed Sn required to cause the 0.86% hydrostatic strain is plotted versus the bowing parameter, which is the same results as presented in Table 3.2 for the hydrostatic strain case. For the bowing parameters ranging from 0 Å to 0.3 Å, the resulting Sn fraction varies from 5.85% to 4.36%, to introduce the 0.86% hydrostatic strain to achieve the indirect to direct transition.

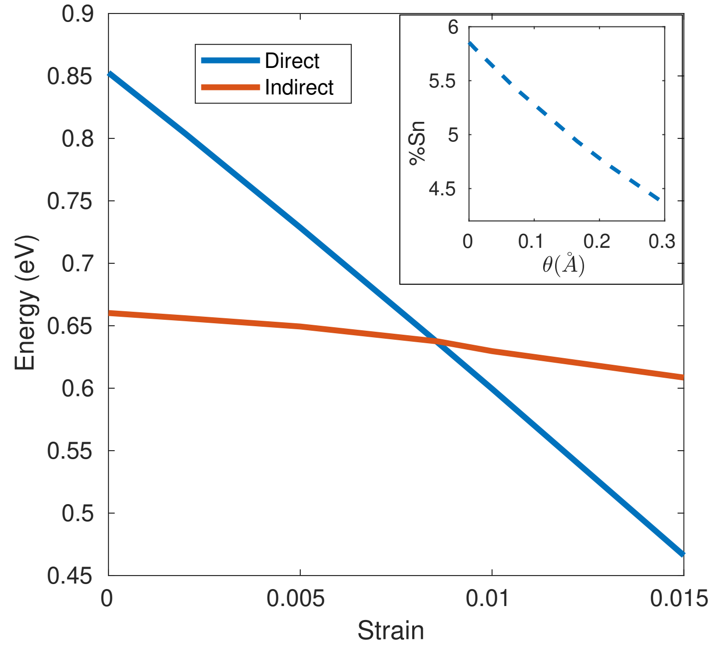

Figure 4.4: The direct and indirect bandgaps versus the tensile hydrostatic strain is plotted. The intercept of the two curves indicates the transition point from the indirect to direct bandgap which is at 0.0086 (0.86%) strain. At this point the bandgap is 0.636eV. In the inset, the fraction of Sn required to achieve this particular volume change versus the bowing parameter is shown.

In Fig. 4.5, we show the Ge band structure of pure Ge as calculated by the

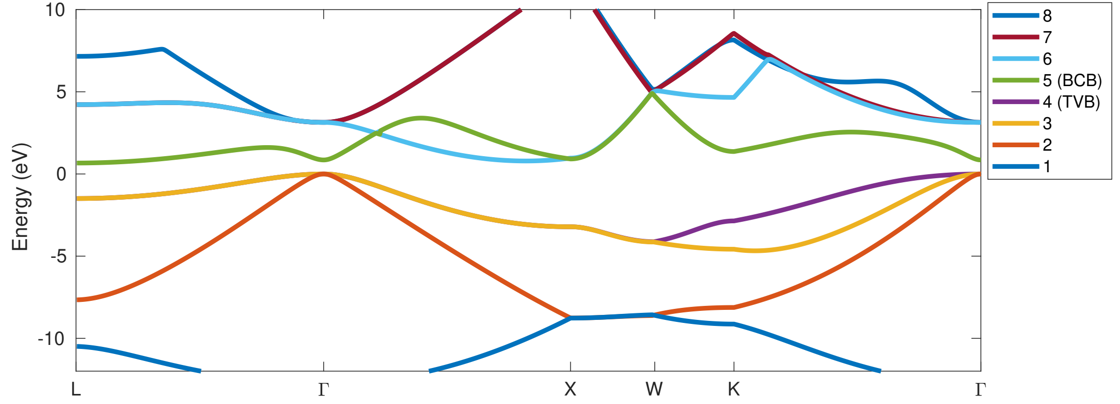

Figure 4.5: Band structure of the Ge lattice without volume change and perturbation (top), Legends 1-4 represent the four top-most valence bands and legends 5-8 represent the four bottom-most conduction bands with No.4 being the top valence band (denoted "TVB") and No.5 being the bottom conduction band (denoted "BCB")

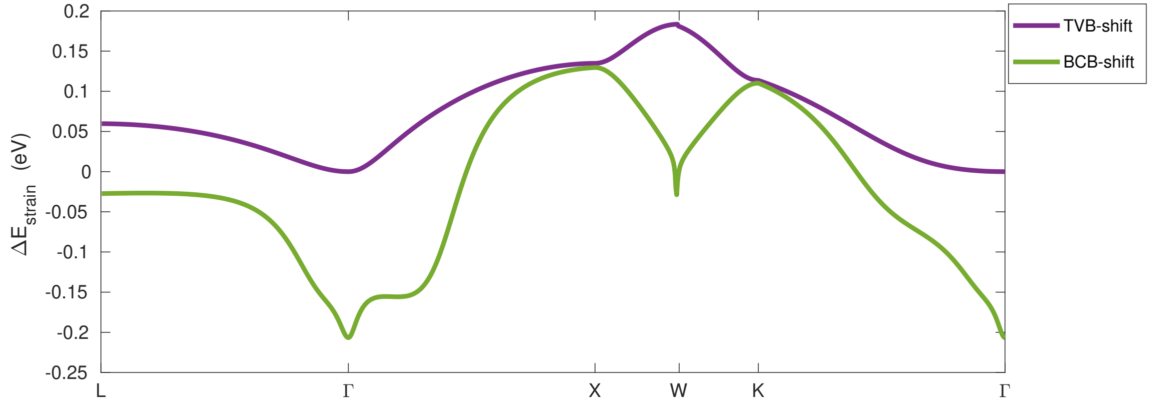

Figure 4.6: Band shift (or energy change) of TVB and BCB solely due to volume change with respect to the original band structure (middle) with 4.67% of Sn and bowing parameter of 0.166Å.

EPM. In Fig. 4.5, the curves labeled "1" - "4" are the valence bands, while those labeled "5" - "8" are the conduction bands. Band number "4" is the top-most valence band (TVB), while band number "5" is the bottom-most conduction band

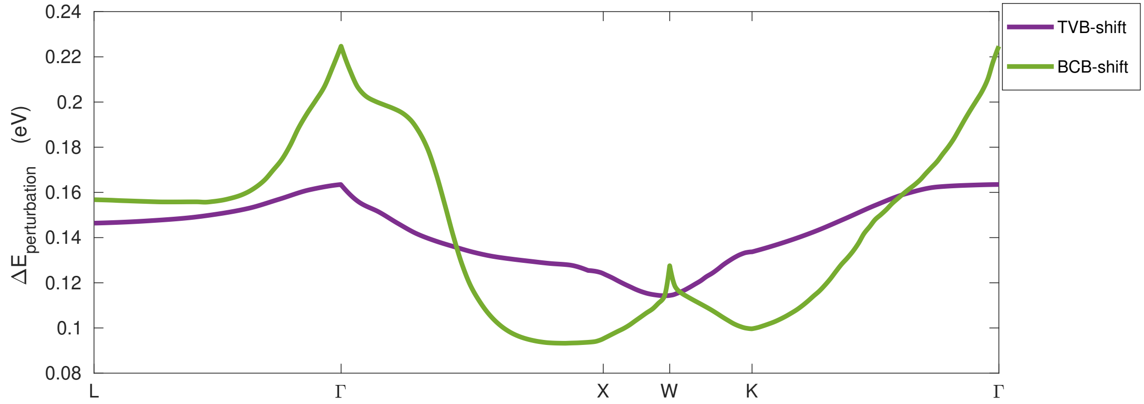

Figure 4.7: Band shift (or energy change) of TVB and BCB solely due to perturbation with respect to the original band structure (bottom) with 4.67% of Sn and bowing parameter of 0.166Å.

(BCB), and these are the bands we are concerned with for the SWIR absorption.

Fig. 4.6 shows the changes in the band structure along the high symmetry directions due to the volume change, introduced by alloying Ge with 4.67% Sn with a bowing parameter of 0.166Å. We see from Fig. 4.6 that this level of Sn fraction reduces the energy of the conduction band at the Γ point by ∼0.2eV, while reducing energy at the original minimum or the L point by only 0.02eV, which helps achieve the transition from indirect to direct. With higher mole fraction of Sn, the induced hydrostatic strain will be sufficient enough to make the transition. This, of course, is without the consideration of the potential difference between a Ge atom and a Sn atom, which will be discussed in the next section.

4.4.2 Potential Difference between Germanium (Ge) and Tin (Sn)

In this section we discuss the effect of the change in potential energy of the valence electrons that results from the substitution of a small percentage of Ge by Sn atoms.

The specific band shift we calculated as due to the potential difference is typically a few tenths of an eV, and is shown in Fig. 4.7. (Note that the total band structure of the GeSn alloy is the summation of Fig. 4.5, Fig. 4.6 and Fig. 4.7.)

The curve labeled "BCB-Shift" in Fig. 4.7 shows how the BCB changes with respect to the original band structure (Fig. 4.5), according to the methodology described in Section 4.3. Under the example case of 4.67% of Sn with bowing parameter of 0.166Å, the influence of the potential difference between Ge and Sn pushes the conduction minimum up at both the Γ and L points, raising the Γ point by 0.225eV and the L point by 0.157eV. This means that the potential difference counteracts the influence of the volume change on the band structure, but not enough to totally diminish the influence of the volume change. This, of course, results in a higher fraction of Sn being required to achieve the indirect-direct bandgap transition.

Reviewing the shapes of the potentials of Ge, Sn and the perturbation (ΔV) that were already shown in Fig. 4.3, the Sn potential has a shallower, yet narrower, potential well when compared to that of Ge. Intuitively speaking, a shallower potential well tends to decrease the separation of the electron energy levels, while on the other hand, a narrower potential well tends to separate the energy levels further apart. The two effects appear to counteract each other. Which effect is dominant

depends firmly on the shape of the perturbation, and therefore could differ from case to case. Here, the localization effect of the perturbation is larger than the lowering of the Ge potential well, thus causing an increase of the bandgaps.

4.4.3 Combined Volume Change and Perturbation Effects

In Fig. 4.8, the bandgap (both direct and indirect) variation with respect to the fraction of alloyed Sn is plotted, taking into account both the volume change and potential difference, with three specific bowing parameters ($\theta = 0\mathring{A}, \theta = 0.15\mathring{A}, \theta = 0.3\mathring{A}$). Fig. 4.8 illustrates that the Sn fraction required to achieve the indirect-direct bandgap transition decreases when bowing parameter increases. The relationship between the required Sn fraction at the transition point and the bowing parameter is plotted in Fig. 4.9 (solid curve). The simulation results show that the required Sn fraction ranges from 5.81% to 8.75% as the bowing parameter ranges from 0.3Å to 0Å, respectively. Fig. 4.9 also shows (dashed curve) the change of BTP versus the bowing parameter. This curve reveals that there is a negligible change in the transition point bandgap as the bowing parameter varies, and the BTP remains at approximately 0.62eV for different bowing parameter values.

4.4.4 Comparison with Reported Experiments

There have been several experimental data reported concerning the fraction of Sn required to achieve the indirect-direct transition. These data are either obtained entirely from experiments or partially based on experimental data with the help of

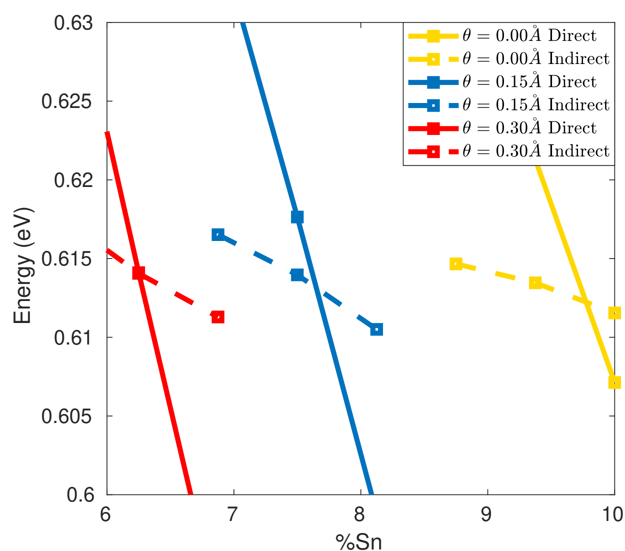

Figure 4.8: The direct (solid) and indirect (dashed) bandgap with respect to different fraction of alloyed Sn. Three specific cases ($\theta = 0\AA, \theta = 0.15\AA, \theta = 0.3\AA$) are plotted.

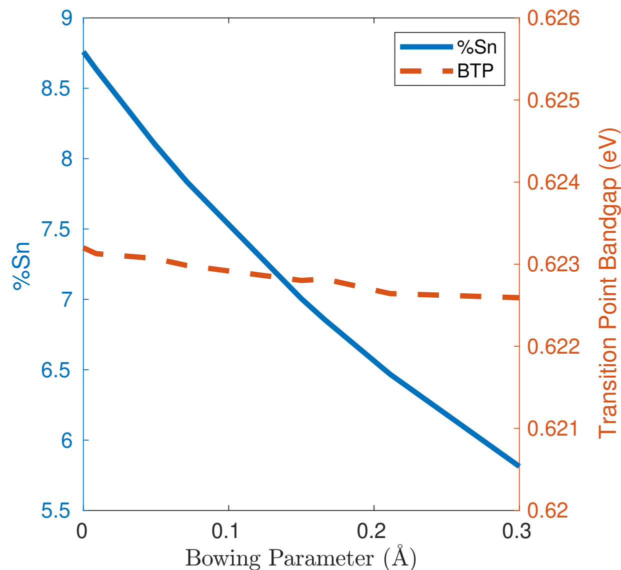

Figure 4.9: The minimum fraction of Sn required to achieve the indirect-direct transition and the BTP vs. bowing parameter.

interpolation.

Ref. [51] reports a value (6%) for the Sn content required to achieve the transition, as well as the range of possible error ($< 11\%$). This measurement overlaps with the results of the present work (ranging from 5.81% to 8.75%). The specific agreement between the results is unknown due to the lack of information about the bowing parameter of the samples measured in Ref. [51].

Ref. [20] provides measurements of Sn fractions, lattice constants (vertical and lateral), residual strain and the direct bandgap of various samples. The researchers observed that samples with a Sn fraction $> 9\%$ give photoluminescence signals similar to those of materials with a direct bandgap.

To further compare the results of this experiment and our work, we calculated the direct bandgap using their reported sample parameters, and compared the values we obtained to the reported measurements of the direct bandgap in Ref. [20].

In Ref. [20], the lattice constants (both parallel and perpendicular to the substrate crystal plane), the mole fraction of Sn, and the residual strain are reported. With this information, we used the method described in Section 4.4.1 to obtain an estimation of the bowing parameter. After performing the calculations using Ref. [20] data as input, we extracted a bowing parameter for their material of approximately 0.056Å.

Having obtained the bowing parameter, and using the reported Sn fraction and the residual strain, we calculated the direct bandgap of each sample measured in Ref. [20]. In Table 4.3, the Ge-Sn alloy samples measured in Ref. [20] are listed with the fraction of Sn, as well as the biaxial strain and direct energy bandgaps

Table 4.3: Comparison of the measurements of the samples reported in Ref. [20] and the calculated values of this work using the EPM with the inclusion of volume change and perturbation.

	Reported Values from Ref. [20]			Calculation from this work	
Sample No.	%Sn	residue biaxial strain	$E_{meas.}$ [a] (eV)	$E_{calc.}$ [b] (eV)	Relative difference
1	10.3	-0.52%	0.562	0.591	5.13%
2	11.5	-0.41%	0.548	0.552	0.75%
3	13.0	-0.71%	0.515	0.531	3.04%

[a] $E_{meas.}$ represents the measured value of the direct bandgap of the samples reported in Ref. [20]

[b] $E_{calc.}$ represents the calculated value of the direct bandgap using the method from this work.

(labeled $E_{meas.}$). Alongside we show our calculated direct bandgaps (labeled $E_{calc.}$), as well as the relative difference between our calculations and the measurements.

The corresponding direct bandgap values between the measurements and our calculations have relative differences of less than 6%, with the lowest relative error being only 0.75%. This agreement between our calculation and the reported experimental measurements provides a reasonable verification of our method.

Chapter 5

Scattering Mechanisms for Monte Carlo (MC) Simulation

Previous chapters focus on the band structure engineering of Ge, which discuss the two methods, applying strain and alloying with Sn, that can transform Ge from an indirect bandgap material to a direct bandgap one, so that Ge can be further utilized in SWIR detector application.

Starting from this chapter, we will discuss the other post-Si material, GaN. GaN has a high breakdown voltage and relatively high carrier mobility[28]. These properties give GaN an advantage in the realm of high power application.

GaN can also form a heterostructure with AlGaN, which can give rise to a 2DEG layer at the interface without intentionally doping either material. The 2DEG layer has an even higher mobility compared to the that of the bulk GaN, which allows the heterostructure to be utilized for the application of the high electron mobility transistors (HEMT).

In this chapter, there will be detailed descriptions of the scattering mechanisms and the means of calculating the scattering rate for each mechanism.

A scattering mechanism describes how an electron can transfer from one state (denoted $\vec{k}$) to another state (denoted $\vec{k'}$). During a phonon related scattering event, an electron is expected to either gain or lose energy, by either absorbing or emitting a phonon, depending on the type of scattering mechanism. Eq. 5.1 describes the

transition rate $S(\vec{k},\vec{k'})$ from state $\vec{k}$ to state $\vec{k'}$[54].

$$S(\vec{k},\vec{k'}) = \frac{2\pi}{\hbar}|\langle\vec{k'}|H'|\vec{k}\rangle|^2\delta(E_{\vec{k'}} - E_{\vec{k}} \mp \hbar\omega) \tag{5.1}$$

where,

H' is the perturbation potential;

$E_{\vec{k}}$ and $E_{\vec{k'}}$ are the corresponding energy for state $\vec{k}$ and $\vec{k'}$, respectively.

$\hbar\omega$ is the energy changed during the scattering event.

The δ function in Eq. 5.1 expresses the conservation of energy. The minus sign indicates an absorption of a phonon with energy of $\hbar\omega$ while the plus sign indicates an emission of a phonon with energy of $\hbar\omega$. For future reference, wherever there is a "$\pm$" or "$\mp$" sign, the upper sign is for absorption and the lower sign is for emission.

If integrating $S(\vec{k},\vec{k'})$ over all possible final states $\vec{k'}$ which satisfy the conservation of energy, we can obtain the scattering rate $W(\vec{k})$, which is more commonly used in MC simulations. This is expressed in Eq. 5.2[54]:

$$\begin{aligned} W(\vec{k}) &= \frac{\Omega}{(2\pi)^3}\int S(\vec{k},\vec{k'})d\vec{k'} \\ &= \frac{2\pi}{\hbar}\frac{\Omega}{(2\pi)^3}\int |\langle\vec{k'}|H'|\vec{k}\rangle|^2\delta(E_{\vec{k'}} - E_{\vec{k}} \mp \hbar\omega)d\vec{k'} \end{aligned} \tag{5.2}$$

where,

Ω is the volume of the crystal.

In the MC simulation for GaN, several scattering mechanisms are considered. The dominant mechanisms for bulk GaN are: acoustic scattering, piezoelectric scattering, polar optical scattering, impurity scattering and intervalley scattering. As for

2DEG, only acoustic scattering, piezoelectric scattering and polar optical scattering are considered. Impurity scattering is neglected for two reasons: (1) the density of 2DEG is very high which provides a screening effect against the impurities; and (2) the formation of 2DEG does not require any intentional doping in the material, which lowers the possibility of being scattered by impurities. As for intervalley scattering, considering that the energy that 2DEG can obtain while remain inside the potential well is usually below 0.5eV, which is far below the lowest energy (>1.9eV) required to be scattered into higher valleys.

The following sections will describe the calculation of each scattering mechanism in detail.

5.1 Acoustic Phonon Scattering

The acoustic phonon scattering mechanism is caused by acoustic phonons, or longitudinal acoustic (LA) phonons, to be more specific. Phonons are essentially the vibration of the crystal, which periodically changes the potential of the lattice that the electrons feel. This perturbation is the cause of electron being scattered from one state to another.

5.1.1 Acoustic Phonon Scattering Rate for Bulk Electrons

The transition rate for acoustic phonon absorption/emission scattering is expressed in Eq. 5.3[23]:

$$S(\vec{k},\vec{k'}) = \frac{\pi \Xi_d^2 q^2}{\rho \omega_{\vec{q}} \Omega} \left(n_{\vec{q}} + \frac{1}{2} \mp \frac{1}{2} \right) \delta(\vec{k'} - \vec{k} \mp \vec{q}) \delta(E_{\vec{k'}} - E_{\vec{k}} \mp \hbar\omega_{\vec{q}}) \tag{5.3}$$

where,

Ξ_d is called the deformation potential, which has units of J. This indicates how much the phonons change the potential of the lattice;

$\vec{q}$ is the wave vector of the phonon;

q is the absolute value of $\vec{q}$;

$q^2 = (\vec{k'} - \vec{k})^2 = 2k^2(1 - cos\theta)$ with θ being the angle between $\vec{k'}$ and $\vec{k}$.

$\omega_{\vec{q}}$ is the angular frequency of the phonon's oscillation;

ρ is the density of the material;

$n_{\vec{q}}$ is the number of acoustic phonons, as given by the Bose-Einstein distribution;

The first and second δ functions in Eq. 5.3 express the conservation of momentum and energy, respectively, which are expressed in Eq. 5.4 and Eq. 5.5:

$$\vec{k'} = \vec{k} \pm \vec{q} \tag{5.4}$$

$$E_{\vec{k'}} = E_{\vec{k}} \pm \hbar\omega_{\vec{q}} \tag{5.5}$$

The $\pm$ sign denotes the absorption or emission of a phonon.

For parabolic and spherical energy bands, by substituting Eq. 5.4 into Eq. 5.5, we can combine the two δ-functions into a single one as follows:

$$\delta\left(\vec{k'}-\vec{k}\mp\vec{q}\right)\delta\left(E_{\vec{k'}}-E_{\vec{k}}\mp\hbar\omega_{\vec{q}}\right)=\delta\left(\frac{\hbar^2q^2}{2m^*}\pm\frac{\hbar^2kq\ cos\theta'}{2m^*}\mp\hbar\omega_{\vec{q}}\right) \tag{5.6}$$

where,

m^* is the effective mass of electrons;

θ' is the polar angle between $\vec{k}$ and $\vec{q}$;

Regarding acoustic phonons of small $\vec{q}$, the dispersion relationship between $\omega_{\vec{q}}$ and $\vec{q}$ is almost linear and can be expressed in the following expression:

$$\frac{\omega_{\vec{q}}}{q}=v_s=\sqrt{\frac{c_L}{\rho}} \tag{5.7}$$

where,

v_s is the velocity of longitudinal elastic waves;

c_L is the elastic constant of the material.

The above expression for the transition rate of acoustic scattering can be simplified, as acoustic phonon energy is much lower than the thermal energy at room temperature. Therefore, the acoustic phonon scattering can be considered no energy loss or gain if $\hbar\omega_{\vec{q}}$ is assumed to be zero. In this case, $n_{\vec{q}}$ can be approximated as $n_{\vec{q}}\approx k_BT_L/\hbar\omega_{\vec{q}}\approx n_{\vec{q}}+1$, with T_L being the temperature of the lattice. Eq. 5.3 can be written as follows:

$$
\begin{aligned}
S(\vec{k},\vec{k'}) &\approx \frac{\pi\Xi_d^2 q^2}{\rho\omega_{\vec{q}}\Omega}\cdot\frac{k_B T_L}{\hbar\omega_{\vec{q}}}\cdot\delta\left(\frac{\hbar^2 q^2}{2m^*}\pm\frac{\hbar^2 kq\ cos\theta'}{m^*}\right)\\
&= \frac{\pi\Xi_d^2 q^2}{\rho\omega_{\vec{q}}\Omega}\cdot\frac{k_B T_L}{\hbar\omega_{\vec{q}}}\cdot\frac{m^*}{\hbar^2 kq}\delta\left(\frac{q}{2k}\pm cos\ \theta'\right)\\
&= \frac{\pi\Xi_d^2 k_B T_L q}{\hbar\omega_{\vec{q}}^2\rho\Omega}\cdot\frac{k}{2E_{\vec{k}}}\cdot\delta\left(\frac{q}{2k}\pm cos\ \theta'\right)\\
&= \frac{\pi\Xi_d^2 k_B T_L}{\hbar c_L\Omega}\cdot\frac{k}{2qE_{\vec{k}}}\cdot\delta\left(\frac{q}{2k}\pm cos\ \theta'\right) \qquad (5.8)
\end{aligned}
$$

Substitute Eq. 5.8 into Eq. 5.2, we can calculate the scattering rate for acoustic scattering as follows:

$$
\begin{aligned}
W(\vec{k}) &= \frac{\Omega}{(2\pi)^3}\int S(\vec{k},\vec{k'})d\vec{k'}\\
&= \frac{\Xi_d^2 k_B T_L}{16\pi^2\hbar c_L}\cdot\frac{k}{E_{\vec{k}}}\cdot\int\frac{1}{q}\delta\left(\frac{q}{2k}\pm cos\ \theta'\right)d\vec{q} \qquad (5.9)
\end{aligned}
$$

The integration over $\vec{q}$ can be carried out in spherical coordinates:

$$
\begin{aligned}
I_q &= \int\frac{1}{q}\delta\left(\frac{q}{2k}\pm cos\ \theta'\right)d\vec{q}\\
&= \int_0^\infty\int_0^\pi\int_0^{2\pi}\frac{1}{q}\ \delta\left(\frac{q}{2k}\pm cos\ \theta'\right)\ q^2\ sin\theta'\ d\phi\ d\theta'\ dq\\
&= \int_0^\infty\int_{-1}^1\int_0^{2\pi} q\ \delta\left(\frac{q}{2k}\pm cos\ \theta'\right)\ d\phi\ d(cos\theta')\ dq \qquad (5.10)
\end{aligned}
$$

The integrations over ϕ and over θ' are straightforward. The limits of the integration over q is limited due to the existence of the δ function. We have assumed $\hbar\omega_{\vec{q}}\approx 0$, thus q_{min} and q_{max} can be obtained as follows:

$$\begin{aligned} q_{min} &= 0 \\ q_{max} &= 2k \end{aligned} \tag{5.11}$$

Thus we can obtain the following:

$$\begin{aligned} I_q &= 2\pi \int_{q_{min}}^{q_{max}} q \, dq \\ &= 2\pi(\frac{q_{max}^2}{2} - \frac{q_{min}^2}{2}) = 4\pi k^2 \end{aligned} \tag{5.12}$$

Therefore, the scattering rate can be obtained as follows:

$$\begin{aligned} W(\vec{k}) &= \frac{\Xi_d^2 k_B T_L}{16\pi^2 \hbar c_L} \cdot \frac{k}{E_{\vec{k}}} \cdot 4\pi k^2 \\ &= \frac{\pi \Xi_d^2 k_B T_L}{2\hbar c_L} N(E_{\vec{k}}) \end{aligned} \tag{5.13}$$

where:

$N(E_{\vec{k}})$ is the density of states, which has units of $m^{-3}J^{-1}$, as expressed in Eq. 5.14.

$$N(E_{\vec{k}}) = \frac{(2m^*)^{3/2}\sqrt{E_{\vec{k}}}}{2\pi^2\hbar^3} \tag{5.14}$$

Eq. 5.13 expresses both the absorption and emission of an acoustic phonon. The energy change during the acoustic scattering is assumed to be zero. Therefore, the total acoustic scattering rate is considered the sum of both absorption and emission, as is expressed in Eq. 5.15.

$$W(\vec{k}) = \frac{\pi \Xi_d^2 k_B T_L}{\hbar c_L} N(E_{\vec{k}}) \tag{5.15}$$

5.1.2 Acoustic Phonon Scattering Rate for 2D Electron Gas (2DEG)

For 2DEG, the electrons are confined in one direction (denoted z), while still considered free electrons in the other two directions (denoted x and y). The wave functions for 2DEG can be expressed as follows:

$$\Psi(\vec{r}) = \psi_n(z) e^{i\vec{k_{\parallel}} \cdot \vec{r_{\parallel}}} \tag{5.16}$$

where:

$\psi_n(z)$ is wave function in the z direction

$\vec{k_{\parallel}}$ is the wave vector in parallel to the xy plane

Due to the quantum confinement in the z direction, the transition rate from state $\vec{k}$ to state $\vec{k'}$ for 2DEG is different from that of the bulk electrons, as is expressed in Eq. 5.17, with the assumption that the energy change during scattering is zero (namely $\hbar\omega = 0$). The transition rate for acoustic phonon absorption/emission scattering for 2DEG is expression as follows[22]:

$$S_{m,n}(\vec{k'}, \vec{k}) = \frac{2\pi}{\hbar} \frac{\Xi_d^2 k_B T_L}{c_L \Omega} |G_{m,n}(q_z)|^2 \; \delta\left(\vec{k_{\parallel'}} - \vec{k_{\parallel}} \mp \vec{q_{\parallel}}\right) \; \delta\left(E_{\vec{k'}} - E_{\vec{k}}\right) \tag{5.17}$$

where,

q_z is the projection of $\vec{q}$ onto the z direction, which satisfies $\vec{q} = \vec{q_{\parallel}} + \vec{q_z}$;

m is the where initial state $\vec{k}$ resides, which is the mth subband;

n is the where initial state $\vec{k'}$ resides, which is the nth subband. The nth subband may be the same as the mth subband, indicating that the scattering event happens within the same subband;

$G_{m,n}(q_z)$ is the interference term between two subbands wave functions, $\psi_m(z)$ and $\psi_n(z)$. It is unitless and is expressed in Eq. 5.18.

$$G_{m,n}(q_z) = \int_{-\infty}^{\infty} \psi_m(z) e^{iq_z z} \psi_n(z) dz \tag{5.18}$$

The first δ function in Eq. 5.17 expresses the conservation of momentum on the xy plane, which differs from the one shown in Eq. 5.1.

The combination of the two δ functions is achieved in a manner similar to that described in the previous section:

$$E_{\vec{k}} = E_m + \frac{\hbar^2 (k_\parallel)^2}{2m^*} \tag{5.19}$$

$$E_{\vec{k'}} = E_n + \frac{\hbar^2 (k'_\parallel)^2}{2m^*} \tag{5.20}$$

E_m is the minimum energy of the mth subband;

E_n is the minimum energy of the nth subband;

Therefore $S_{m,n}(\vec{k'}, \vec{k})$ is rewritten as:

$$\begin{aligned} S_{m,n}(\vec{k'}, \vec{k}) &= \frac{2\pi}{\hbar} \frac{\Xi_d^2 k_B T_L}{c_L \Omega} |G_{m,n}(q_z)|^2 \\ &\times \delta\left(\frac{\hbar^2}{2m^*} q_\parallel^2 \pm \frac{\hbar^2}{m^*} k_\parallel q_\parallel cos\theta' + E_n - E_m \right) \end{aligned} \tag{5.21}$$

where θ' is the angle between $\vec{k_\parallel}$ and $\vec{q_\parallel}$.

The integration over $\vec{k'}$ to obtain the scattering rate is carried out in a different manner to that described in the previous section, as shown in the following equation:

$$
\begin{aligned}
W_{m,n}(\vec{k}) &= \frac{\Omega}{(2\pi)^3}\int S(\vec{k'},\vec{k})d\vec{k'} \\
&= \frac{\Omega}{(2\pi)^3}\frac{2\pi}{\hbar}\frac{\Xi_d^2 k_B T_L}{c_L\Omega}\int\int\int |G_{m,n}(q_z)|^2 \\
&\quad \delta\left(\frac{\hbar^2}{2m^*}q_\parallel^2 \pm \frac{\hbar^2}{m^*}k_\parallel q_\parallel cos\theta' + E_n - E_m\right) dq_z q_\parallel dq_\parallel d\theta' \\
&= \frac{1}{\hbar(2\pi)^2}\frac{\Xi_d^2 k_B T_L}{c_L}\int |G_{m,n}(q_z)|^2 dq_z \\
&\quad \int\int \delta\left(\frac{\hbar^2}{2m^*}q_\parallel^2 \pm \frac{\hbar^2}{m^*}k_\parallel q_\parallel cos\theta' + E_n - E_m\right) q_\parallel dq_\parallel d\theta' \qquad (5.22)
\end{aligned}
$$

The second integration in the above equation is carried out as follows:

$$
\begin{aligned}
I_q &= \int\int \delta\left(\frac{\hbar^2}{2m^*}q_\parallel^2 \pm \frac{\hbar^2}{m^*}k_\parallel q_\parallel cos\theta' + E_n - E_m\right) q_\parallel dq_\parallel d\theta' \qquad (5.23) \\
&= \int\int \delta\left(\frac{\hbar^2}{2m^*}q_\parallel^2 \pm \frac{\hbar^2}{m^*}k_\parallel q_\parallel cos\theta' + E_n - E_m\right) \frac{1}{|sin\theta|} q_\parallel dq_\parallel d(cos\theta') \\
&= \int\int \frac{m^*}{\hbar^2 k_\parallel q_\parallel}\delta\left(cos\theta' \pm \frac{m^*(E_n - E_m)}{\hbar^2 k_\parallel q_\parallel} \pm \frac{q_\parallel}{2k_\parallel}\right)\frac{1}{|sin\theta|} q_\parallel dq_\parallel d(cos\theta') \\
&= \frac{m^*}{\hbar^2 k_\parallel}\int\int \delta\left(cos\theta' \pm \frac{m^*(E_n - E_m)}{\hbar^2 k_\parallel q_\parallel} \pm \frac{q_\parallel}{2k_\parallel}\right)\frac{1}{|sin\theta|} dq_\parallel d(cos\theta') \\
&= \frac{m^*}{\hbar^2 k_\parallel}\int \frac{1}{|sin\left(\theta'(q_\parallel)\right)|} dq_\parallel
\end{aligned}
$$

where $\theta'(q_\parallel)$ is the value for θ' being evaluated at $q_\parallel$ by equaling the argument inside the δ function in Equ. 5.23 to 0, as shown below:

$$
cos\theta' \pm \frac{m^*(E_n - E_m)}{\hbar^2 k_\parallel q_\parallel} \pm \frac{q_\parallel}{2k_\parallel} = 0 \qquad (5.24)
$$

which gives the evaluated $cos\left(\theta'(q_\parallel)\right)$ as follows:

$$cos\left(\theta'(q_\parallel)\right) = \mp\frac{m^*(E_n - E_m)}{\hbar^2 k_\parallel q_\parallel} \mp \frac{q_\parallel}{2k_\parallel} \tag{5.25}$$

Continuing the integration:

$$\begin{aligned} I_q &= \frac{m^*}{\hbar^2 k_\parallel}\int \frac{1}{|sin\left(\theta'(q_\parallel)\right)|}dq_\parallel \\ &= \frac{m^*}{\hbar^2 k_\parallel}\int \frac{1}{\sqrt{1-|cos\left(\theta'(q_\parallel)\right)|^2}}dq_\parallel \\ &= \frac{m^*}{\hbar^2 k_\parallel}\int \frac{1}{\sqrt{1-|\frac{m^*(E_n-E_m)}{\hbar^2 k_\parallel q_\parallel}+\frac{q_\parallel}{2k_\parallel}|^2}}dq_\parallel \end{aligned} \tag{5.26}$$

Recall Equ. 5.19, and plug it into the I_q:

$$\begin{aligned} I_q &= \frac{m^*}{\hbar^2 k_\parallel}\int \frac{1}{\sqrt{1-|\frac{m^*(E_n-E_{\vec{k}})}{\hbar^2 k_\parallel q_\parallel}+\frac{k_\parallel}{2q_\parallel}+\frac{q_\parallel}{2k_\parallel}|^2}}dq_\parallel \\ &= \frac{m^*}{\hbar^2 k_\parallel}\cdot k_\parallel\ arcsin\left(\frac{q_\parallel^2 - k_\parallel\left(k_\parallel + 2\frac{m^*(E_{\vec{k}})}{\hbar^2 k_\parallel}\right)}{2^{\frac{3}{2}}\sqrt{\frac{m^* k_\parallel^2 (E_{\vec{k}})}{\hbar^2}}}\right)\Bigg|_{q_{\parallel,min}}^{q_{\parallel,max}} \end{aligned} \tag{5.27}$$

The limit for $q_\parallel$ is evaluated using Equ. 5.24, where the value for $cos\theta$ is limited between -1 and 1:

$$q_{\parallel,min} = \begin{cases} k_\parallel - \frac{\sqrt{2m^*(E_{\vec{k}}-E_n)}}{\hbar}, & E_n > E_m \\ -k_\parallel + \frac{\sqrt{2m^*(E_{\vec{k}}-E_n)}}{\hbar}, & E_n < E_m \end{cases} \tag{5.28}$$

$$q_{\parallel,max} = k_\parallel + \frac{\sqrt{2m^*(E_{\vec{k}}-E_n)}}{\hbar} \tag{5.29}$$

The square roots in the expressions for both $q_{\parallel,min}$ and $q_{\parallel,max}$ also imply that $E_{\vec{k}} > E_n$ needs to be satisfied for Equ. 5.28 and 5.29 to be valid.

By substituting Equ. 5.28 and 5.29 back into Equ. 5.27, we can obtain the expression for the integration:

$$
\begin{aligned}
I_q &= \frac{m^*}{\hbar^2 k_\parallel} \cdot k_\parallel \; arcsin \left(\frac{q_\parallel^2 - k_\parallel \left(k_\parallel + 2\frac{m^*(E_{\vec{k}})}{\hbar^2 k_\parallel} \right)}{2^{\frac{3}{2}} \sqrt{\frac{m^* k_\parallel^2 (E_{\vec{k}})}{\hbar^2}}} \right) \Bigg|_{q_{\parallel,min}}^{q_{\parallel,max}} \qquad (5.30) \\
&= \begin{cases} \frac{m^*}{\hbar^2 k_\parallel} \cdot k_\parallel \cdot \left[\frac{\pi}{2} - \left(-\frac{\pi}{2} \right) \right], & E_{\vec{k}} > E_n \\ 0, & E_{\vec{k}} < E_n \end{cases} \\
&= \begin{cases} \frac{\pi m^*}{\hbar^2}, & E_{\vec{k}} > E_n \\ 0, & E_{\vec{k}} < E_n \end{cases} \\
&= \pi^2 \cdot N_{2D}(E_{\vec{k}})
\end{aligned}
$$

where $N_n(E_{\vec{k}})$ is the 2D density of states of the nth subband, which has units of $m^{-2}J^{-1}$, as expressed as follows:

$$
N_{2D}(E_{\vec{k}}) = \begin{cases} \frac{m^*}{\pi \hbar^2}, & E_{\vec{k}} > E_n \\ 0, & E_{\vec{k}} < E_n \end{cases} \qquad (5.31)
$$

By carrying out the rest of the integration, we can obtain the scattering rate from the mth subband to the nth subband:

$$
W_{m,n}(\vec{k}) = \frac{\Xi_d^2 k_B T_L}{4\hbar c_L} \; \phi(m,n) \; N_n(E_{\vec{k}}) \qquad (5.32)
$$

where $\phi(m,n)$, which has units of m^{-1}, is given by the following:

$$\phi(m,n) = \int_{-\infty}^{\infty} |G_{m,n}(q_z)|^2 dq_z \tag{5.33}$$

5.2 Piezoelectric Scattering

As mentioned in the previous chapter, GaN is a piezoelectric material along the c-axis ($\langle 0001 \rangle$ direction). The lattice vibrations in the material can also cause polarization waves. The polarization waves can interact strongly with electrons, causing polar scattering of electrons. Polar scattering may be due to either acoustic or optical phonons. As mentioned previously, phonons are vibrations of the lattice. In a piezoelectric material, this vibrations can also change the potential of the lattice due to the reverse piezoelectric effect. Therefore, polar acoustic phonon scattering can also be called piezoelectric scattering, which is the term used in this paper. The scattering rate due to piezoelectric scattering mechanism is derived here, while polar optical scattering will be discussed further in the next section.

5.2.1 Piezoelectric Scattering Rate for Bulk Electrons

The energy change due to piezoelectric scattering is also assumed zero. The transition rate from state $\vec{k}$ to $\vec{k'}$ is expressed as follows[21]:

$$S(\vec{k'},\vec{k}) = \frac{2\pi}{\hbar}\frac{\hbar q^2}{\rho\Omega\omega}\left(\frac{eh_{pz}}{\epsilon_\infty}\right)^2\frac{k_BT_L}{\hbar\omega}\frac{1}{q^2+q_D^2}\delta\left(\vec{k'}-\vec{k}\mp\vec{q}\right)\delta\left(E_{\vec{k'}}-E_{\vec{k}}\right) \tag{5.34}$$

where:

e is the elementary charge;

h_{pz} is the piezoelectric constant of the material.

ϵ_∞ is the optical dielectric constant of the material

$1/q_D$ is known as the Debye length, given by $\sqrt{e^2 n_0/(\epsilon_s k_B T)}$, with n_0 being the equilibrium electron density at a temperature T.

The scattering rate can be obtained by integrating over all possible final state $\vec{k'}$.

$$
\begin{aligned}
W(\vec{k}) &= \frac{\Omega}{(2\pi)^3} \int S(\vec{k'}, \vec{k}) d\vec{k'} \\
&= \frac{2\pi}{\hbar} \frac{\hbar q^2}{\rho \Omega \omega} \left(\frac{e h_{pz}}{\epsilon_\infty} \right)^2 \frac{k_B T_L}{\hbar \omega} \frac{1}{q^2 + q_D^2} \int \delta \left(\vec{k'} - \vec{k} \mp \vec{q} \right) \delta \left(E_{\vec{k'}} - E_{\vec{k}} \right) d\vec{k'} \\
&= \frac{k_B T_L}{(2\pi)^2 \hbar c_L} \left(\frac{e h_{pz}}{\epsilon_\infty} \right)^2 \int \frac{1}{q^2 + q_D^2} \delta \left(\frac{\hbar^2 q^2}{2m^*} \pm \frac{\hbar^2 k q \ cos\theta'}{m^*} \right) d\vec{q} \qquad (5.35)
\end{aligned}
$$

where θ' is the polar angle between $\vec{k}$ and $\vec{q}$.

Integration over $\vec{k'}$ is switched to integration over $\vec{q}$ because it is more convenient in our case and because $d\vec{k'} = d\vec{q}$.

The integration in the equation above can be carried out under spherical coordinates:

$$\begin{aligned}
I_q &= \int \frac{1}{q^2+q_D^2}\delta\left(\frac{\hbar^2 q^2}{2m^*} \pm \frac{\hbar^2 kq\ cos\theta'}{m^*}\right) d\vec{q} \\
&= \int\int\int \frac{1}{q^2+q_D^2}\delta\left(\frac{\hbar^2 q^2}{2m^*} \pm \frac{\hbar^2 kq\ cos\theta'}{m^*}\right)\ q^2\ sin\theta'\ d\phi\ d\theta'\ dq \\
&= 2\pi \int\int \frac{q^2}{q^2+q_D^2}\delta\left(\frac{\hbar^2 q^2}{2m^*} \pm \frac{\hbar^2 kq\ cos\theta'}{m^*}\right)\ sin\theta'\ d\theta'\ dq \\
&= 2\pi \int\int \frac{q^2}{q^2+q_D^2}\frac{m^*}{\hbar^2 kq}\delta\left(\frac{q}{2k} \pm cos\ \theta'\right) d(cos\theta')dq \\
&= \frac{2\pi m^*}{\hbar^2 k}\int\int \frac{q}{q^2+q_D^2}\delta\left(\frac{q}{2k} \pm cos\ \theta'\right) d(cos\theta')dq \\
&= \frac{2\pi m^*}{\hbar^2 k} ln(q^2+q_D^2)\Big|_{q_{min}}^{q_{max}}
\end{aligned} \tag{5.36}$$

Both q_{min} and q_{max} are the same the ones in Equ. 5.11. Thus the integration gives:

$$\begin{aligned}
I_q &= \frac{2\pi m^*}{\hbar^2 k} ln(q^2+q_D^2)\Big|_{q_{min}}^{q_{max}} \\
&= \frac{2\pi m^*}{\hbar^2 k} ln\left(1+\frac{4k^2}{q_D^2}\right)
\end{aligned} \tag{5.37}$$

Thus the scattering rate is expressed as follows:

$$\begin{aligned}
W(\vec{k}) &= \frac{k_B T_L}{(2\pi)^2 \hbar c_L}\left(\frac{eh_{pz}}{\epsilon_\infty}\right)^2 \frac{2\pi m^*}{\hbar^2 k} ln\left(1+\frac{4k^2}{q_D^2}\right) \\
&= \frac{k_B T_L}{4\pi \hbar c_L}\left(\frac{eh_{pz}}{\epsilon_\infty}\right)^2 \frac{k}{E_{\vec{k}}}\ ln\left(1+\frac{4k^2}{q_D^2}\right)
\end{aligned} \tag{5.38}$$

5.2.2 Piezoelectric Scattering Rate for 2D Electron Gas (2DEG)

The transition rate from state $\vec{k}$ to $\vec{k'}$ is expressed as follows[22]:

$$
\begin{aligned}
S_{m,n}(\vec{k'},\vec{k}) &= \frac{2\pi}{\hbar}\frac{\hbar q^2}{\rho\Omega\omega}\left(\frac{eh_{pz}}{\epsilon_\infty}\right)^2\frac{k_BT_L}{\hbar\omega}\frac{1}{q^2+q_D^2} \\
&\quad\times|G_{m,n}(q_z)|^2\delta\left(\vec{k'_\parallel}-\vec{k_\parallel}\mp\vec{q_\parallel}\right)\delta\left(E_{\vec{k'}}-E_{\vec{k}}\right) \\
&= \frac{2\pi}{\hbar}\frac{k_BT_L}{\Omega c_L}\left(\frac{eh_{pz}}{\epsilon_\infty}\right)^2\frac{1}{q^2+q_D^2}|G_{m,n}(q_z)|^2 \\
&\quad\times\delta\left(\frac{\hbar^2}{2m^*}q_\parallel^2\pm\frac{\hbar^2}{m^*}k_\parallel q_\parallel cos\theta'+E_n-E_m\right)
\end{aligned}
\tag{5.39}
$$

where θ' is the angle between $\vec{k_\parallel}$ and $\vec{q_\parallel}$.

The scattering rate can be obtained by integrating over all possible final state $\vec{k'}$, as shown below:

$$
\begin{aligned}
W_{m,n}(\vec{k}) &= \frac{\Omega}{(2\pi)^3}\int S(\vec{k'},\vec{k})d\vec{k'} \\
&= \frac{\Omega}{(2\pi)^3}\frac{2\pi}{\hbar}\frac{k_BT_L}{\Omega c_L}\left(\frac{eh_{pz}}{\epsilon_\infty}\right)^2\int\int\int|G_{m,n}(q_z)|^2 \\
&\quad\times\frac{1}{q_\parallel^2+q_z^2+q_D^2}\delta\left(\frac{\hbar^2}{2m^*}q_\parallel^2\pm\frac{\hbar^2}{m^*}k_\parallel q_\parallel cos\theta'+E_n-E_m\right)q_\parallel dq_\parallel d\theta' dq_z \\
&= \frac{k_BT_L}{(2\pi)^2\hbar c_L}\left(\frac{eh_{pz}}{\epsilon_\infty}\right)^2\int\int\int|G_{m,n}(q_z)|^2\frac{q_\parallel}{q_\parallel^2+q_z^2+q_D^2}\frac{1}{|sin\theta'|} \\
&\quad\times\frac{m^*}{\hbar^2k_\parallel q_\parallel}\delta\left(cos\theta'\pm\frac{m^*(E_n-E_m)}{\hbar^2k_\parallel q_\parallel}\pm\frac{q_\parallel}{2k_\parallel}\right)dq_\parallel d(cos\theta')dq_z \\
&= \frac{k_BT_L}{(2\pi)^2\hbar c_L}\left(\frac{eh_{pz}}{\epsilon_\infty}\right)^2\frac{m^*}{\hbar^2k_\parallel}\int\int\int\frac{|G_{m,n}(q_z)|^2}{q_\parallel^2+q_z^2+q_D^2}\frac{1}{|sin\theta'|} \\
&\quad\delta\left(cos\theta'\pm\frac{m^*(E_n-E_m)}{\hbar^2k_\parallel q_\parallel}\pm\frac{q_\parallel}{2k_\parallel}\right)dq_\parallel d(cos\theta')dq_z \\
&= \frac{k_BT_L}{(2\pi)^2\hbar c_L}\left(\frac{eh_{pz}}{\epsilon_\infty}\right)^2\frac{m^*}{\hbar^2k_\parallel} \\
&\quad\int\int\int\frac{|G_{m,n}(q_z)|^2}{q_\parallel^2+q_z^2+q_D^2}\frac{1}{|sin\left(\theta'(q_\parallel)\right)|}dq_\parallel dq_z
\end{aligned}
\tag{5.40}
$$

where $sin\left(\theta'(q_{\|})\right)$ is evaluated by solving the equation as follows with $cos\theta'$ ranging from -1 to 1:

$$cos\theta' \pm \frac{m^*(E_n - E_m)}{\hbar^2 k_{\|} q_{\|}} \pm \frac{q_{\|}}{2k_{\|}} = 0 \tag{5.41}$$

The integration over $q_{\|}$ and q_z cannot be separated due to the existence of the term $1/(q_{\|}^2 + q_z^2 + q_D^2)$, therefore numerical integration is usually needed to evaluate Eq. 5.40.

5.3 Polar Optical Scattering

As mentioned in the previous section, polar optical scattering is due to the polarization waves caused by the optical phonons.

5.3.1 Polar Optical Scattering Rate for Bulk Electrons

The transition rate for polar optical scattering is expressed as follows[21]:

$$S(\vec{k'}, \vec{k}) = \frac{\pi e^2 \omega_0}{\epsilon_p \Omega} \frac{1}{q^2} \left[n(\omega_0) + \frac{1}{2} \mp \frac{1}{2} \right] \delta\left(\vec{k'} - \vec{k} \mp \vec{q}\right) \delta\left(E_{k'} - E_k \mp \hbar\omega_0\right) \tag{5.42}$$

where:

ω_0 is the angular frequency of the polar optical phonon;

$n(\omega_0)$ is the number of the optical phonons;

$1/\epsilon_p = 1/\epsilon_\infty - 1/\epsilon_s$, and ϵ_∞ and ϵ_s are the optical and static dielectric constants of the material, respectively.

The scattering rate can be obtained by integrating over all possible states $\vec{k'}$. Considering that $d\vec{k'} = d\vec{q}$, it is more convenient to integrate over $\vec{q}$, as expressed below:

$$\begin{aligned} W(\vec{k}) &= \frac{\Omega}{(2\pi)^3} \int \frac{\pi e^2 \omega_0}{\epsilon_p \Omega} \frac{1}{q^2} \left[n(\omega_0) + \frac{1}{2} \mp \frac{1}{2} \right] \\ &\quad \times \delta \left(\vec{k'} - \vec{k} \mp \vec{q} \right) \delta \left(E_{k'} - E_k \mp \hbar\omega_0 \right) d\vec{q} \\ &= \frac{\Omega}{(2\pi)^3} \frac{\pi e^2 \omega_0}{\epsilon_p \Omega} \left[n(\omega_0) + \frac{1}{2} \mp \frac{1}{2} \right] \\ &\quad \int \frac{1}{q^2} \, \delta \left(\frac{\hbar^2 q^2}{2m^*} \pm \frac{\hbar^2 kq \; cos\theta'}{m^*} \mp \hbar\omega_0 \right) d\vec{q} \end{aligned} \tag{5.43}$$

The δ function is dealt with in the manner as described in Sec. 5.1.1. The integration is carried out in a polar coordinate with θ' being the polar angle between $\vec{k}$ and $\vec{q}$.

$$\begin{aligned} I_q &= \int \frac{1}{q^2} \, \delta \left(\frac{\hbar^2 q^2}{2m^*} \pm \frac{\hbar^2 kq \; cos\theta'}{m^*} \mp \hbar\omega_0 \right) d\vec{q} \\ &= \int_0^{2\pi} \int_0^{\pi} \int_0^{\infty} \frac{1}{q^2} \, \delta \left(\frac{\hbar^2 q^2}{2m^*} \pm \frac{\hbar^2 kq \; cos\theta'}{m^*} \mp \hbar\omega_0 \right) q^2 sin\theta' dq d\theta' d\phi \\ &= \int_0^{2\pi} \int_0^{\pi} \int_0^{\infty} \frac{m^*}{\hbar^2 k} \frac{1}{q} \delta \left(cos\theta' - \frac{m^* \omega_0}{\hbar kq} \pm \frac{q}{2k} \right) dq d(cos\theta') d\phi \\ &= \frac{2\pi m^*}{\hbar^2 k} ln \left(\frac{q_{max}}{q_{min}} \right) \end{aligned} \tag{5.44}$$

The range of q is determined by the δ function's argument equaling zero and $cos\theta'$ ranging from -1 to 1, which gives the following:

$$q_{min} = k\left[1-\left(1\pm\frac{\hbar\omega_0}{E_{\vec{k}}}\right)^{1/2}\right] \tag{5.45}$$

$$q_{max} = k\left[1+\left(1\pm\frac{\hbar\omega_0}{E_{\vec{k}}}\right)^{1/2}\right] \tag{5.46}$$

5.3.2 Polar Optical Scattering Rate for 2D Electron Gas (2DEG)

The transition rate from $\vec{k'}$ to $\vec{k}$ is expressed as follows[22]:

$$\begin{aligned}
S_{m,n}(\vec{k'},\vec{k}) &= \frac{\pi e^2\omega_0}{\epsilon_p\Omega}\frac{1}{q^2}\left[n(\omega_0)+\frac{1}{2}\mp\frac{1}{2}\right]|G_{m,n}(q_z)|^2 \\
&\quad \times\delta\left(\vec{k'}-\vec{k}\mp\vec{q}\right)\delta\left(E_{k'}-E_k\mp\hbar\omega_0\right) \\
&= \frac{\pi e^2\omega_0}{\epsilon_p\Omega}\frac{1}{q^2}\left[n(\omega_0)+\frac{1}{2}\pm\frac{1}{2}\right]|G_{m,n}(q_z)|^2 \\
&\quad \delta\left(\frac{\hbar^2}{2m^*}q_{\|}^2\pm\frac{\hbar^2}{m^*}k_{\|}q_{\|}cos\theta'+E_n-E_m\mp\hbar\omega\right)
\end{aligned} \tag{5.47}$$

where $G_{m,n}(q_z)$ is the same as that described in Eq. 5.18 and θ' is the angle between $\vec{k_{\|}}$ and $\vec{q_{\|}}$.

The scattering rate is obtained by integrating over all possible k' states in the nth subband.

$$
\begin{aligned}
W_{m,n}(\vec{k}) &= \frac{e^2\omega_0}{8\pi^2\epsilon_p}\left[n(\omega_0)+\frac{1}{2}\mp\frac{1}{2}\right]\int\int\int\frac{1}{q_\parallel^2+q_z^2}|G_{m,n}(q_z)|^2 \\
&\times\delta\left(\frac{\hbar^2}{2m^*}q_\parallel^2 \pm \frac{\hbar^2}{m^*}k_\parallel q_\parallel cos\theta' + E_n - E_m \mp \hbar\omega\right) dq_z q_\parallel dq_\parallel d\theta' \\
&= \frac{m^*}{\hbar^2 k_\parallel}\frac{e^2\omega_0}{8\pi^2\epsilon_p}\left[n(\omega_0)+\frac{1}{2}\mp\frac{1}{2}\right]\int\int\int\frac{1}{q_\parallel^2+q_z^2}|G_{m,n}(q_z)|^2 \\
&\times\delta\left(\frac{q_\parallel}{2k_\parallel}\pm cos\theta' + \frac{m^*}{\hbar^2 k_\parallel q_\parallel(E_n - E_m \mp \hbar\omega)}\right) dq_z dq_\parallel d\theta' \\
&= \frac{m^*}{\hbar^2 k_\parallel}\frac{e^2\omega_0}{8\pi^2\epsilon_p}\left[n(\omega_0)+\frac{1}{2}\mp\frac{1}{2}\right]\int_{q_\parallel^{min}}^{q_\parallel^{max}}\frac{F_{m,n}(q_\parallel)}{|sin\ \theta'(q_\parallel)|}dq_\parallel \qquad (5.48)
\end{aligned}
$$

where,

$$F_{m,n}(q_\parallel) = \int_{-\infty}^{\infty}\frac{1}{q_\parallel^2+q_z^2}|G_{m,n}(q_z)|^2 dq_z \qquad (5.49)$$

The integration over $q_\parallel$ and q_z cannot be separated due to the existence of the term $1/(q_\parallel^2+q_z^2)$, therefore numerical integration is usually needed to evaluate Eq. 5.48.

5.4 Impurity Scattering

The perturbation potential for impurity scattering is expressed as a screened Coulombic potential, thus the transition rate is expressed as follows[21, 24, 23]:

$$S(\vec{k'},\vec{k}) = \frac{2\pi}{\hbar}\frac{N_I Z^2 e^4}{\Omega\epsilon_s^2}\frac{\delta(E_{\vec{k'}} - E_{\vec{k}})}{(q^2+q_D^2)^2} \qquad (5.50)$$

where,

Ze is the charge on the impurity atom;

N_I is the impurity concentration;

$q^2 = (\vec{k'} - \vec{k})^2 = 2k^2(1 - cos\theta)$ with θ being the angle between $\vec{k'}$ and $\vec{k}$.

The scattering rate of impurity scattering can be obtained by integrating over all possible $\vec{k'}$ states, as expressed below:

$$\begin{aligned}
W(\vec{k}) &= \frac{\Omega}{(2\pi)^3}\frac{2\pi}{\hbar}\frac{N_I Z^2 e^4}{\Omega\epsilon_s^2}\int_0^{2\pi}\int_0^{\pi}\int_0^{\infty}\frac{(k')^2 sin\theta\delta(E_{\vec{k'}} - E_{\vec{k}})}{\left(2k^2[1 - cos\theta] + q_D^2\right)^2}dk'd\theta d\phi \\
&= \frac{\Omega}{(2\pi)^3}\frac{2\pi}{\hbar}\frac{N_I Z^2 e^4}{\Omega\epsilon_s^2}2\pi\int_1^{-1}\frac{sin\theta}{\left(2k^2[1 - cos\theta] + q_D^2\right)^2}d\theta \\
&\quad \times \int_0^{\infty}(k')^2\delta\left(\frac{\hbar^2(k')^2}{2m^*} - \frac{\hbar^2 k^2}{2m^*}\right)dk' \\
&= \frac{N_I Z^2 e^4}{2\pi\hbar\epsilon_s^2} \times \frac{2}{q_D^2(4k^2 + q_D^2)} \times \frac{m^* k}{\hbar^2} \\
&= \frac{\pi N_I Z^2 e^4}{\hbar\epsilon_s^2}\frac{N(E_{\vec{k}})}{q_D^2(4k^2 + q_D^2)}
\end{aligned} \tag{5.51}$$

5.5 Intervalley Scattering

For the GaN MC simulation, multiple valleys (Γ_1, Γ_3 and U) are included. Γ_1 is the lowest valley, where low energy electrons sit in k-space. When electrons gain sufficient energy, they can be scattered into higher valleys by optical phonon scattering.

The transition rate from $\vec{k}$ to $\vec{k'}$ is expressed as follows[23]:

$$
\begin{aligned}
S_{i,j}(\vec{k'},\vec{k}) &= \frac{\pi D_{ij}^2 Z_j}{\rho\omega_{ij}\Omega}\left[n(\omega_{ij}+\frac{1}{2}\mp\frac{1}{2})\right] \\
&\times\ \delta(\vec{k'}-\vec{k}\mp\vec{q})\ \delta\left(E_{j,\vec{k'}}-E_{i,\vec{k}}\mp\hbar\omega_{ij}-\Delta E_{ji}\right) \\
&= \frac{\pi D_{ij}^2 Z_j}{\rho\omega_{ij}\Omega}\left[n(\omega_{ij}+\frac{1}{2}\mp\frac{1}{2})\right] \\
&\quad \delta\left(\frac{\hbar^2 k^2}{2}\left(\frac{1}{m_j^*}-\frac{1}{m_i^*}\right)\pm\frac{\hbar^2 kq}{m_j}cos\theta'+\frac{\hbar^2 q^2}{2m_j}\mp\hbar\omega_{ij}+\Delta E_{ji}\right) \quad (5.52)
\end{aligned}
$$

where,

i and j represent the initial valley and the final valley, respectively;

m_i^* and m_j^* are the effective masses of electrons in valley i and valley j, respectively;

D_{ij} is the intervalley deformation potential, which describes the optical phonon that can scatter electrons from valley i to valley j;

θ' is the polar angle between $\vec{k}$ and $\vec{q}$;

Z_j is the number of equivalent final valleys;

ΔE_{ij} is the energy difference from the bottom of valley j to the bottom of valley i;

The scattering rate can be obtained by integrating over possible final states in valley j:

$$
\begin{aligned}
W(\vec{k}) &= \frac{\Omega}{(2\pi)^3}\int S(\vec{k'},\vec{k})d\vec{k'} \\
&= \frac{D_{ij}^2 Z_j}{8\pi^2\rho\omega_{ij}}\left[n(\omega_{ij}+\frac{1}{2}\mp\frac{1}{2})\right]\int\delta\left(\frac{\hbar^2k^2}{2}\left(\frac{1}{m_j^*}-\frac{1}{m_i^*}\right)\right. \\
&\quad \left.\pm\frac{\hbar^2kq}{m_j}cos\theta'+\frac{\hbar^2q^2}{2m_j}\mp\hbar\omega_{ij}+\Delta E_{ji}\right)d\vec{q} \qquad (5.53)
\end{aligned}
$$

where the integration over $\vec{q}$ can be carried out in a polar coordinate:

$$
\begin{aligned}
I_q &= \int\delta\left(\frac{\hbar^2k^2}{2}\left(\frac{1}{m_j^*}-\frac{1}{m_i^*}\right)\pm\frac{\hbar^2kq}{m_j}cos\theta'+\frac{\hbar^2q^2}{2m_j}\mp\hbar\omega_{ij}+\Delta E_{ji}\right)d\vec{q} \\
&= \int_0^{2\pi}\int_0^{\pi}\int_0^{\infty}\delta\left(\frac{\hbar^2k^2}{2}\left(\frac{1}{m_j^*}-\frac{1}{m_i^*}\right)\right. \\
&\quad \left.\pm\frac{\hbar^2kq}{m_j}cos\theta'+\frac{\hbar^2q^2}{2m_j}\mp\hbar\omega_{ij}+\Delta E_{ji}\right)q^2sin\theta'dqd\theta'd\phi \\
&= 2\pi\int_{-1}^{1}\int_0^{\infty}\frac{m_j}{\hbar^2kq}\delta\left(\frac{k}{2q}\left(1-\frac{m_j}{m_i}\right)\pm cos\theta'\right. \\
&\quad \left.+\frac{q}{2k}+\frac{m_j}{\hbar^2kq}(\Delta E_{ji}\mp\hbar\omega_{ij})\right)q^2dqd(cos\theta') \\
&= \frac{\pi m_j}{\hbar^2k}\left(q_{max}^2-q_{min}^2\right) \qquad (5.54)
\end{aligned}
$$

where θ' is the polar angle between $\vec{k}$ and $\vec{q}$, and q_{max} and q_{min} are obtained by equating the argument of the δ function with $cos\theta'$ ranging from -1 to 1, which are given as follows:

$$
\begin{aligned}
q_{max} &= k+k\left[\frac{m_j}{m_i}-\frac{m_j}{m_i}\frac{\Delta E_{ji}\mp\hbar\omega_{ij}}{E_{\vec{k}}}\right]^{1/2} \qquad (5.55) \\
q_{max} &= k-k\left[\frac{m_j}{m_i}-\frac{m_j}{m_i}\frac{\Delta E_{ji}\mp\hbar\omega_{ij}}{E_{\vec{k}}}\right]^{1/2} \qquad (5.56)
\end{aligned}
$$

Thus:

$$\begin{aligned} I_q &= \frac{2\pi k^3}{E_{\vec{k}}}\left(\frac{m_j}{m_i}\right)^{3/2}\left[1-\frac{\Delta E_{ji}\mp\hbar\omega_{ij}}{E_{\vec{k}}}\right]^{1/2} \\ &= 4\pi^3 N_j(E_{\vec{k}}\pm\hbar\omega_{ij}-\Delta E_{ji}) \end{aligned} \tag{5.57}$$

where N_j is the density of state in valley j.

Therefore, the scattering rate is expressed as follows:

$$\begin{aligned} W(\vec{k}) &= \frac{D_{ij}^2 Z_j}{8\pi^2\rho\omega_{ij}}\left[n(\omega_{ij}+\frac{1}{2}\mp\frac{1}{2})\right]4\pi^3 N_j(E_{\vec{k}}\pm\hbar\omega_{ij}-\Delta E_{ji}) \\ &= \frac{\pi D_{ij}^2 Z_j}{2\rho\omega_{ij}}\left[n(\omega_{ij}+\frac{1}{2}\mp\frac{1}{2})\right]N_j(E_{\vec{k}}\pm\hbar\omega_{ij}-\Delta E_{ji}) \end{aligned} \tag{5.58}$$

5.6 Scattering Angle Selection

The calculation of the scattering rates for different mechanisms determines the probability of each mechanism occurring during the scattering event. After a scattering event, an scattering angle is also needed, which determines the direction that the electron is scattering into[54].

Recall Equ. 5.2, which describes the scattering rate for bulk electrons. It is also repeated here:

$$\begin{aligned} W(\vec{k}) &= \frac{\Omega}{(2\pi)^3}\int S(\vec{k},\vec{k'})d\vec{k'} \qquad (5.59) \\ &= \frac{2\pi}{\hbar}\frac{\Omega}{(2\pi)^3}\int|\langle\vec{k'}|H'|\vec{k}\rangle|^2\delta(E_{\vec{k'}}-E_{\vec{k}}\mp\hbar\omega)d\vec{k'} \end{aligned}$$

As shown in all the detailed derivations of all the bulk scattering mechanisms, Equ. 5.59 is carried out in spherical coordinates:

$$
\begin{aligned}
W(\vec{k}) &= \frac{2\pi}{\hbar}\frac{\Omega}{(2\pi)^3}\int |\langle\vec{k'}|H'|\vec{k}\rangle|^2\delta(E_{\vec{k'}} - E_{\vec{k}} \mp \hbar\omega)d\vec{k'} \qquad (5.60)\\
&= \int\int\int \frac{\Omega}{\hbar(2\pi)^2}|\langle\vec{k'}|H'|\vec{k}\rangle|^2\delta(E_{\vec{k'}} - E_{\vec{k}} \mp \hbar\omega)\ (k')^2\ sin\theta\ d\phi\ d\theta\ dk'\\
&= \int_0^{\pi}\left(2\pi\int \frac{\Omega}{\hbar(2\pi)^2}|\langle\vec{k'}|H'|\vec{k}\rangle|^2\delta(E_{\vec{k'}} - E_{\vec{k}} \mp \hbar\omega)\ (k')^2\ sin\theta\ dk'\right)d\theta
\end{aligned}
$$

Integration over ϕ is straight forward since the argument of the integration does not have ϕ dependence. The outer integration of the equation above is the integration over θ. If we replace the definite integration over θ from 0 to π by an indefinite integration, then $W(\vec{k})$ becomes $W(\theta,\vec{k})$, a function of θ and $\vec{k}$, as in:

$$
W(\theta,\vec{k}) = \int_0^{\theta} F(\theta,\vec{k})d\theta \qquad (5.61)
$$

where:

$$
F(\theta,\vec{k}) = \left(2\pi\int \frac{\Omega}{\hbar(2\pi)^2}|\langle\vec{k'}|H'|\vec{k}\rangle|^2\delta(E_{\vec{k'}} - E_{\vec{k}} \mp \hbar\omega)\ (k')^2\ sin\theta\ dk'\right) \qquad (5.62)
$$

To get the scattering angle, a random number r is generated between 0 and 1. By solving:

$$
r = \frac{W(\theta,\vec{k})}{W(\vec{k})} = \frac{\int_0^{\theta} F(\theta,\vec{k})d\theta}{\int_0^{\pi} F(\theta,\vec{k})d\theta} \qquad (5.63)
$$

we can obtain a value for θ, which is the scattering angle corresponding to the randomly generated number r.

A similar method can also be applied to obtain the scattering angle for 2D scattering, except that the integration is carried out in polar coordinates:

$$
\begin{aligned}
W_{m,n}(k) &= \frac{\Omega}{(2\pi)^3}\int S(\vec{k'},\vec{k})d\vec{k'} \\
&= \int\int\int \frac{\Omega}{(2\pi)^3} S(\vec{k'},\vec{k})dq_z q_{\|} dq_{\|} d\theta \\
&= \int_0^{\pi}\left(\int\int \frac{\Omega}{(2\pi)^3} S(\vec{k'},\vec{k})dq_z q_{\|} dq_{\|}\right) d\theta \\
&= \int_0^{\pi} F_{m,n}(\theta,\vec{k})d\theta \qquad (5.64)
\end{aligned}
$$

Again, we replace the definite integration over θ from 0 to π by an indefinite integration, then $W_{m,n}(\vec{k})$ becomes $W_{m,n}(\theta,\vec{k})$:

$$
W_{m,n}(\theta,\vec{k}) = \int_0^{\theta} F_{m,n}(\theta,\vec{k})d\theta \qquad (5.65)
$$

Then the scattering angle can be obtained by solving the equation as follows:

$$
r = \frac{W_{m,n}(\theta,\vec{k})}{W_{m,n}(\vec{k})} = \frac{\int_0^{\theta} F_{m,n}(\theta,\vec{k})d\theta}{\int_0^{\pi} F_{m,n}(\theta,\vec{k})d\theta} \qquad (5.66)
$$

where r is a randomly generated number between 0 and 1.

Considering that it may not the possible to get an analytical expression for $F(\theta,\vec{k})$, numerical evaluation may be necessary to solve Equ. 5.63 and 5.66.

5.7 Summary

Now that we have all the formulas to calculate the scattering rates for all the scattering mechanisms, we can implement the MC method described in Chapter 1. By summing up the scattering rates from all the contributing mechanisms, we

can determine the flight time for the electron to drift under the influence of the applied electric field between scattering events. The percentage of each scattering rate determines the probability for a corresponding scattering event to happen at the end of the flight time.

The following chapters will describe the implementation of the MC method to investigate the electron transport in both bulk and 2DEG system.

Chapter 6

Investigation of Electron Transport in Bulk Gallium Nitride (GaN)

In this chapter, the electron transport properties in bulk GaN material is investigated by using MC method. The process of implementing the MC method is introduced in Chapter 1, as shown in the flowchart in Fig. 1.6. The formulas for calculating the scattering rates for all the mechanisms included in the MC simulation are described in detail in the previous chapter. In addition, to investigate the high electric field performance of bulk GaN, a three-valley model is applied, which consists of one conduction band minimum valley (denoted "Γ_1") and two higher energy valleys (denoted "Γ_3" and "U"). The three valleys are illustrated in the conduction band structure diagram for GaN as shown in Fig. 6.1. The parameters for the three valleys are listed in Table. 6.1, alongside the scattering mechanism parameters used in our MC simulation.

6.1 Calculation of the Scattering Rates and Analysis

As is mentioned previously, for our MC simulation for bulk GaN, the included scattering mechanisms are: acoustic scattering, piezoelectric scattering, polar optical scattering, impurity scattering and intervalley scattering.

The scattering rates for all the included mechanisms are calculated using the formulas described in the previous chapter and the parameters presented in Table

Table 6.1: Material properties of GaN and parameters for three-valley model for MC[39].

Material Parameter			
Mass density: ρ (kg/m^3)	6150		
Longitudinal sound velocity: v_s (m/s)	6560		
Acoustic Deformation Potential: Ξ_d (eV)	8.3		
Static dielectric constant: ϵ_s	8.9		
High frequency dielectric constant: ϵ_∞	5.35		
Piezoelectric constant: h_{pz} (C/m^2)	0.5		
Optical phonon energy: $\hbar\omega_0$ (meV)	91.2		
Intervalley deformation potential*: $D_{iv}(10^9 eV/cm)$	1		
Intervalley phonon energies: $\hbar\omega_0$ (meV)	91.2		
Valley	Γ_1	Γ_3	$L-M$
Effective mass (m_0)	0.2	1	1
Intervalley energy separation (eV)	0	2	2.1
Nonparabolicity (eV^{-1})	0.189	0.065	0.029

*Note: D_{iv} applies for all the D_{ij}'s in Equ. 5.58 for intervalley scattering rate calculation.

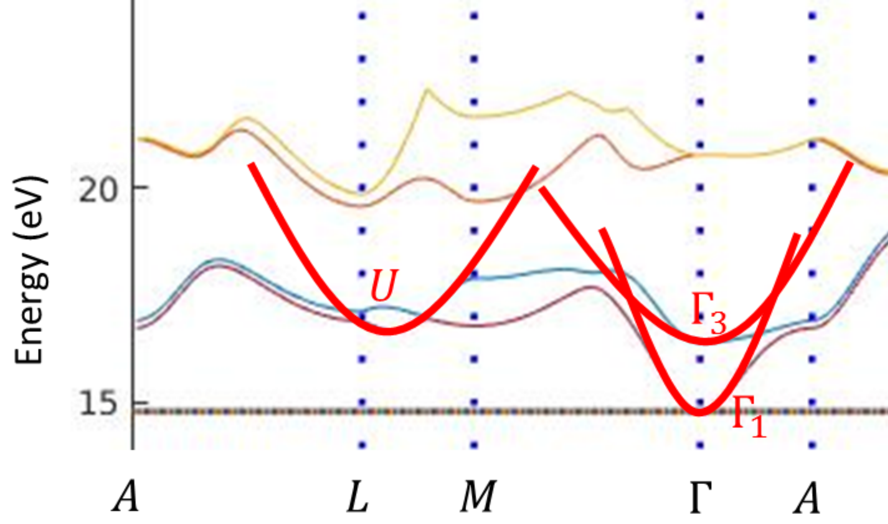

Figure 6.1: EPM calculated conduction band structure with the illustration of the three-valley model ("Γ_1", "Γ_3" and "U") for MC simulation.

6.1. The calculation results are shown in Fig. 6.2 for all the included mechanisms with the exception of impurity scattering, which is shown in Fig. 6.3 on its own to compare the difference with different doping concentrations being considered. The x axes in all graphs in Fig. 6.2 and 6.3 are electron energy with the reference as the bottom of Γ_1 valley.

Of all the scattering mechanisms included, polar optical scattering S_{pop} (absorption and emission) is the dominant mechanism when the electron energy is above 0.1 eV. S_{pop} peaks around $10^{14}s^{-1}$ at about 0.3 eV, then decays with further increasing electron energy. Acoustic phonon scattering S_{ac} shows a consistently increasing trend with respect to the increasing electron energy and it is the second most dominant scattering mechanism overall. Piezoelectric scattering S_{pz} decreases significantly with increasing electron energy and becomes negligible after the electron energy increases above 0.1 eV.

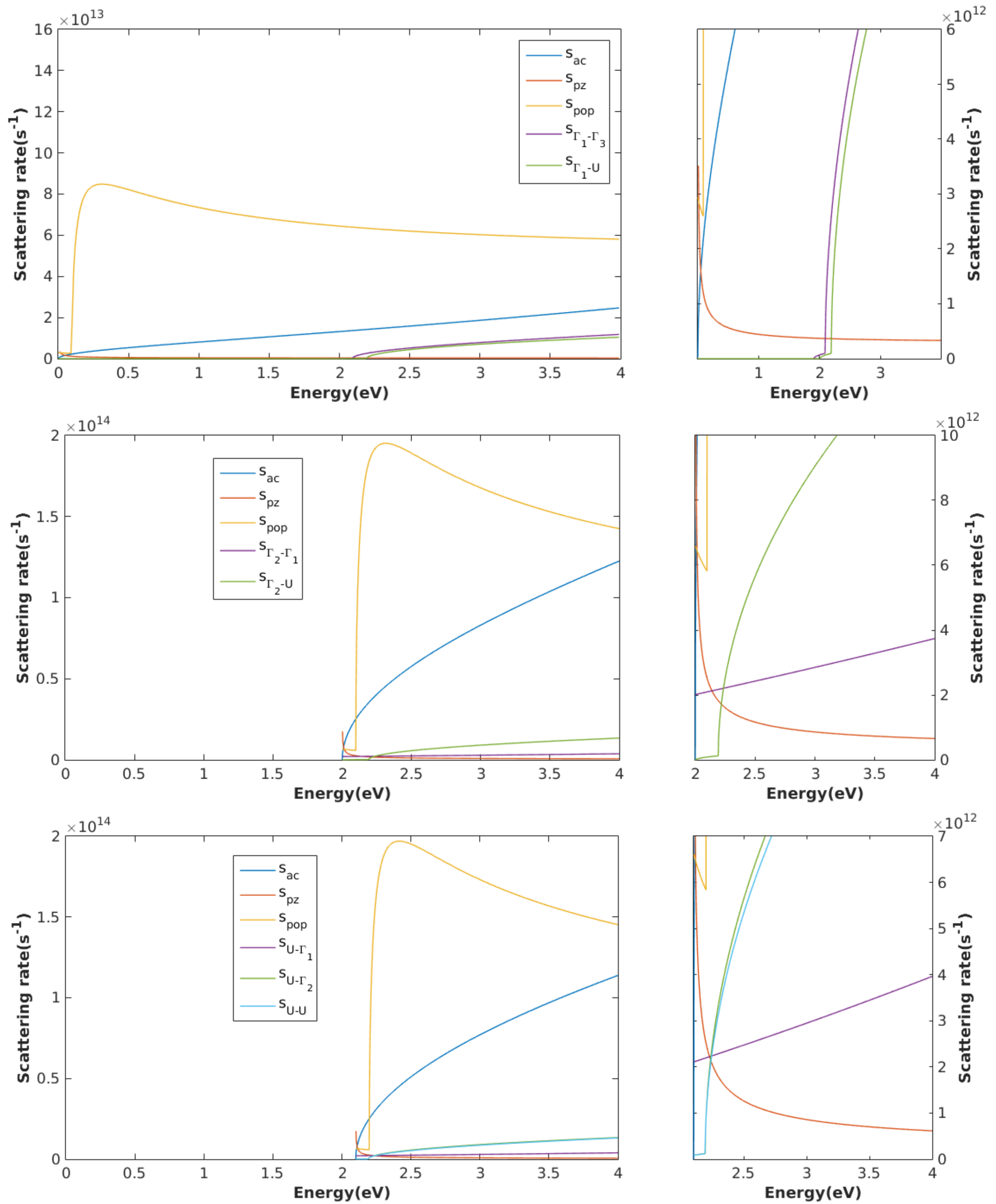

Figure 6.2: The calculated scattering rates vs. electron energy for Γ_1 valley, Γ_3 valley and U valley. The left-side graphs are a full range sweep of the electron energy(0-4eV), with y axes set to the same range. The right-side graphs are zoom-in of the left side graphs.

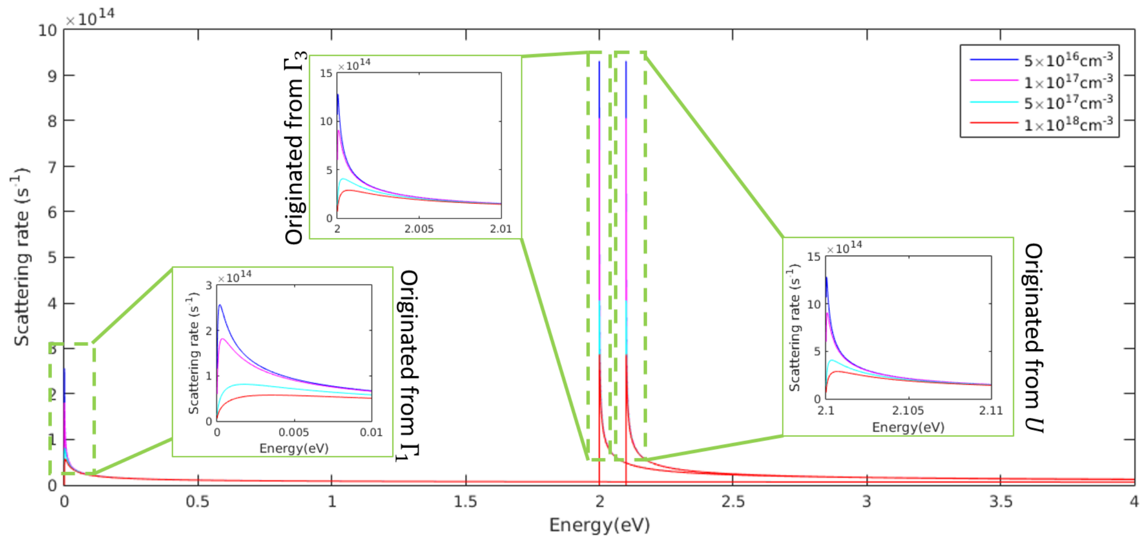

Figure 6.3: The calculated impurity scattering rates vs. electron energy for Γ_1 valley, Γ_3 valley and U valley under different impurity concentrations.

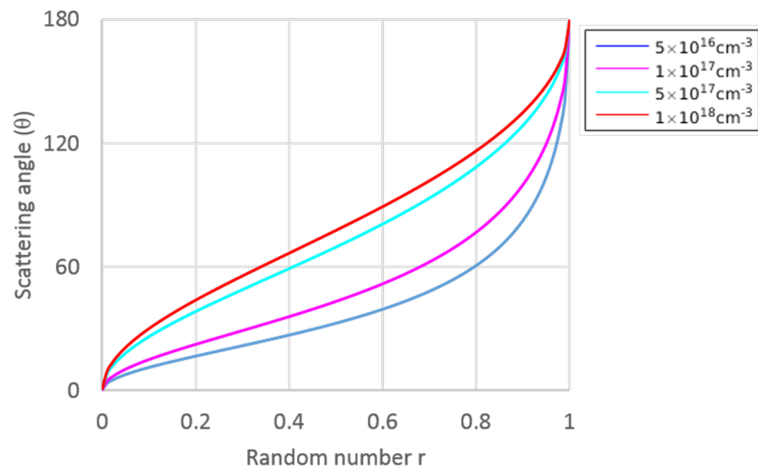

Figure 6.4: The calculated impurity scattering angle vs. generated random number for Γ_1 valley at electron energy of 0.002 eV under different impurity concentrations.

The impurity scattering rates are dependent on the impurity concentration and the carrier concentration. These two effects counteract each other. Higher impurity concentration provides more scattering centers in the lattice while higher carrier concentration provides heavier screening effect so the carriers won't be influenced by the impurities as much. The calculation results presented in Fig. 6.3 show that lower impurity concentration gives higher scattering rate, indicating that the screening effect of the carriers is playing stronger role at impurity scattering. The calculation results also show a fast decaying of the scattering rate after the electron energy is above 0.01 eV, which makes it more effective at low electric field simulation but negligible at high electric field.

However, in the case of impurity scattering, higher scattering rate at lower impurity concentration does not equal to lower drift velocity. To explain this, an example of the selection of scattering angle based on a randomly generated number between 0 and 1 is shown in Fig. 6.4, using method described in the previous chapter. This figure is for the impurity scattering with electron energy of 0.002 eV. Four cases of different impurity concentrations are presented and compared in the figure. We can observe in Fig. 6.4, that when the impurity concentration is high, it is more probable to have the electron being scattered at a wider angle, thus more probable to be scattered in the direction against the acceleration under the electric field. While when the impurity concentration is low, the electrons tend to be scattered in the same direction as that before the impurity scattering event. This conserves more acceleration rather than diminishes it as in the high impurity concentration case.

Whether the magnitude of the impurity scattering or the scattering angle selection can win over each other cannot be determined at this point. The effect of impurity scattering under different impurity concentration will be investigated in the following section as well.

6.2 Set up for Bulk Gallium Nitride (GaN) Monte Carlo (MC) Simulation

A single MC simulation is set up with a specific electric field as its input. The simulation begins with its first iteration with an initial total simulated time t_{total} of $10^{-9}s$. Each iteration adds 10% more to t_{total}, that is, t_{total} increases by 10% after each iteration. The convergence criterion is defined such that the average drift velocity does not change by more than 1% in five consecutive iterations. In addition to the strict convergence criterion, 100 repeated simulations are run for one input of electric field.

During the run of a single MC simulation, the information of the electron, such as momentum ($\vec{k}$), electron energy (E) and the valley that the electron is in, are updated and collected at equal interval time of $10^{-15}s$. The evolution of $\vec{k}$ is governed by the equation below:

$$\Delta\vec{k} = -\frac{e\vec{F}}{\tau} \tag{6.1}$$

where:

e is the elementary charge;

τ is the interval sampling time;

$\Delta\vec{k}$ is the change of momentum $\vec{k}$ during the time period of τ;

$\vec{F}$ is the applied electric field.

The electron energy can be calculated once the updated momentum ($\vec{k}$) is obtained:

$$E = \frac{\hbar^2\vec{k}^2}{2m_n^*} + E_{gn} \tag{6.2}$$

where:

Subscript n represents the valley that the electron is in at the time of sampling;

m_n^* is the effective mass of valley n;

E_{gn} is the bottom energy of valley n;

The instantaneous velocity at each sampling point of time is calculated using the equation expressed as follows:

$$\vec{v} = \frac{\hbar}{m_n^* \cdot [1 + 2\alpha(E - E_{gn})]} \cdot \vec{k} \tag{6.3}$$

where,

E is the total electron energy;

α is the nonparabolicity parameter of the valley.

The drift velocity used in the convergence criterion is the average of all the sampled values of instantaneous velocity. The valley occupation percentage for a specific valley is defined as the percentage of the sampling points that record the electron being in the chosen valley with respect to the total number of the sampling points.

6.3 Results and Analysis

Fig. 6.5 shows an example of the sampled values of the electron energy during the simulation of the applied electric field of 130kV/cm with the impurity concentration of $10^{17} cm^{-3}$. To better examine the curve, the region near 0.1 ns in Fig. 6.5 is enlarged and shown in the bottom figure. In this figure, the evolution of the electron energy is more clear and the scattering events that happen during this time window are marked with red crosses. In between scattering events, the electron energy changes parabolically, as expressed in Equ. 6.2. We can also observe the different behaviors of different scattering mechanisms. Some of the scattering events result in a sudden change of the energy. These scattering events are the ones associated with absorption or emission of optical phonons, such as polar optical scattering and intervalley scattering. While the others don't change the electron energy during the scattering event. Those are associated with the scattering mechanisms such as acoustic phonon scattering, piezoelectric scattering and impurity scattering.

Fig. 6.6 shows the plot of the average electron energy versus the electric field. The insets for Fig. 6.6 are the distribution of the electron energy (the probabil-

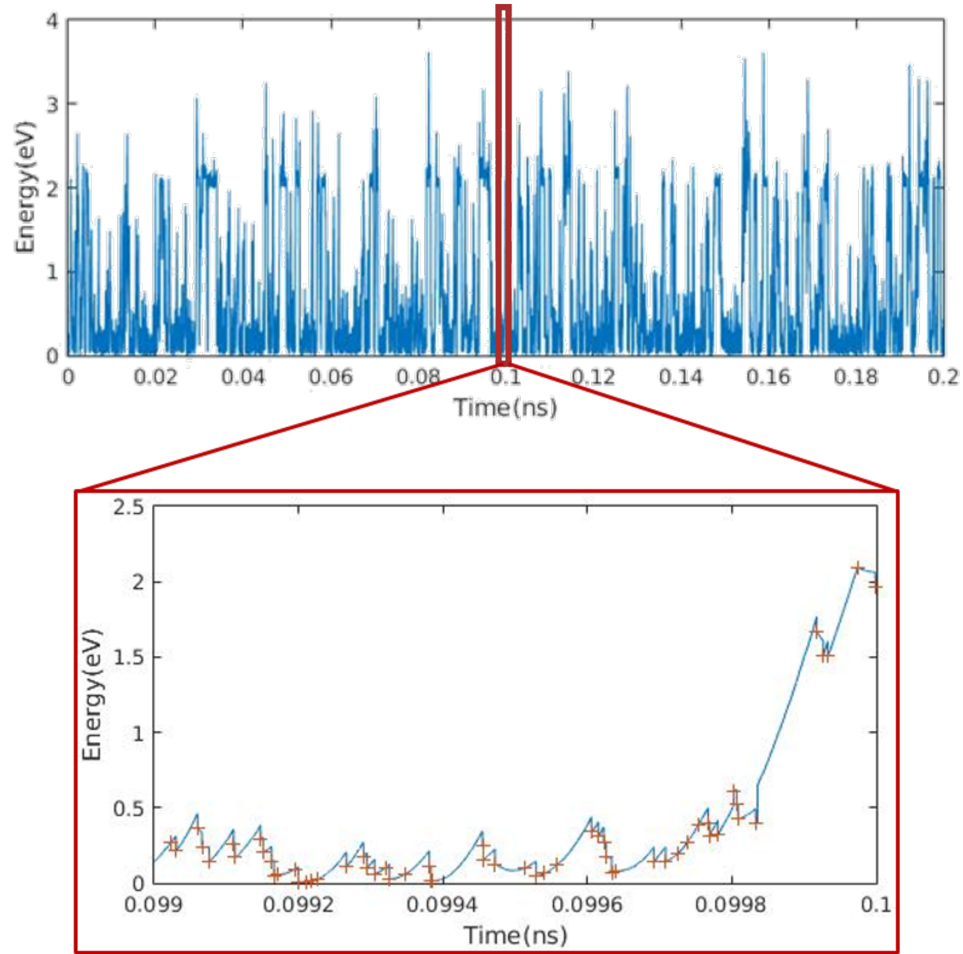

Figure 6.5: (Top) The electron energy versus simulation time (ranging from 0 to 0.2ns) at the electrical field of 130kV/cm with the impurity concentration of $10^{17}cm^{-3}$. (Bottom) Zoom-in of the top figure at around 0.1ns simulation time. Every red cross mark represents a scattering event.

ity density of electron energy) at chosen electric fields (10kV/cm, 130kV/cm and 300kV/cm). The distribution of the electron energy resembles a Boltzmann distribution. The inset for 10kV/cm is somewhat distorted, probably due to the limited number of scattering events happening during the simulation time at such a low electric field. When the electric field increases, the distribution curve is more spread out and shifts more towards higher energy. The electrons are also more likely to

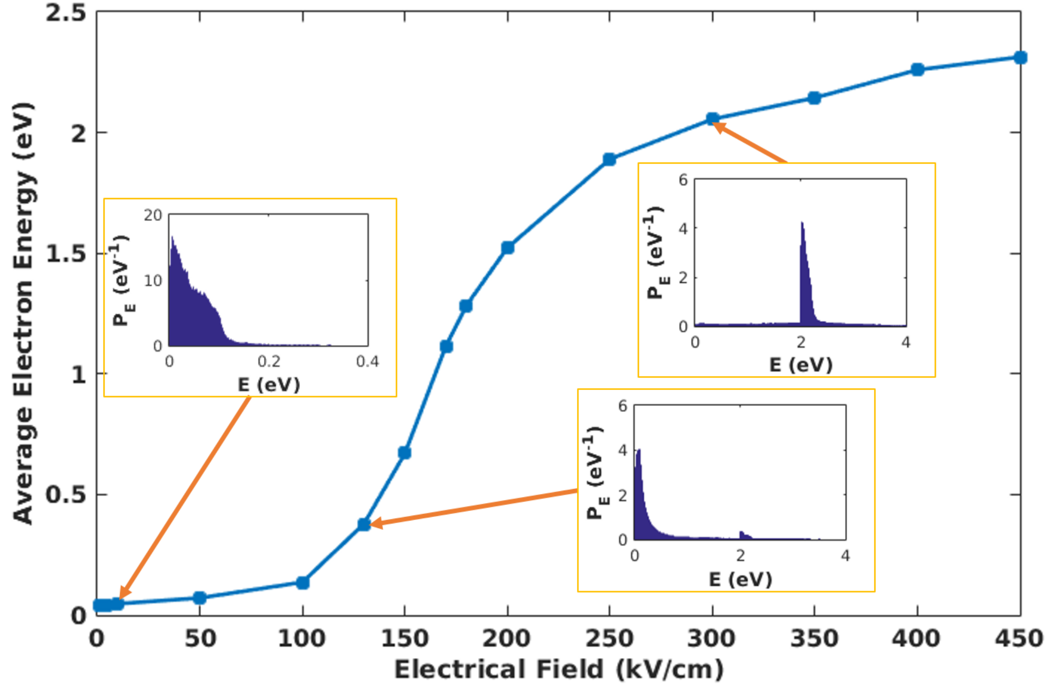

Figure 6.6: The average electron energy versus the electric field (full range: 0 - 450kV/cm) with the impurity concentration of $10^{17}cm^{-3}$. The insets are distributions of the sampled electron energies (the probability density of the electron energy) at selected electric field of 10kV/cm, 130kV/cm and 300kV/cm

be scattered into a higher valley, which can be observed as the minor "bump" at higher energy in the inserted plot in Fig. 6.6 extracted at 130kV/cm. The "bump" is located at around 2 eV, which corresponds to the bottom energy of Γ_3 valley. At this level of electric field, a new "Boltzmann-like" distribution begins to build up at the Γ_3 valley, which could also be mixed with the distribution at the U valley, considering that the difference between the bottoms of both valleys is only 0.1 eV. The "bump" continues to grow as the electric field increases, even becomes dominant at even higher electric fields, as shown in the inserted plot at 300 kV/cm in Fig. 6.6.

In Fig. 6.7, the valley occupation percentages for different valleys are plotted

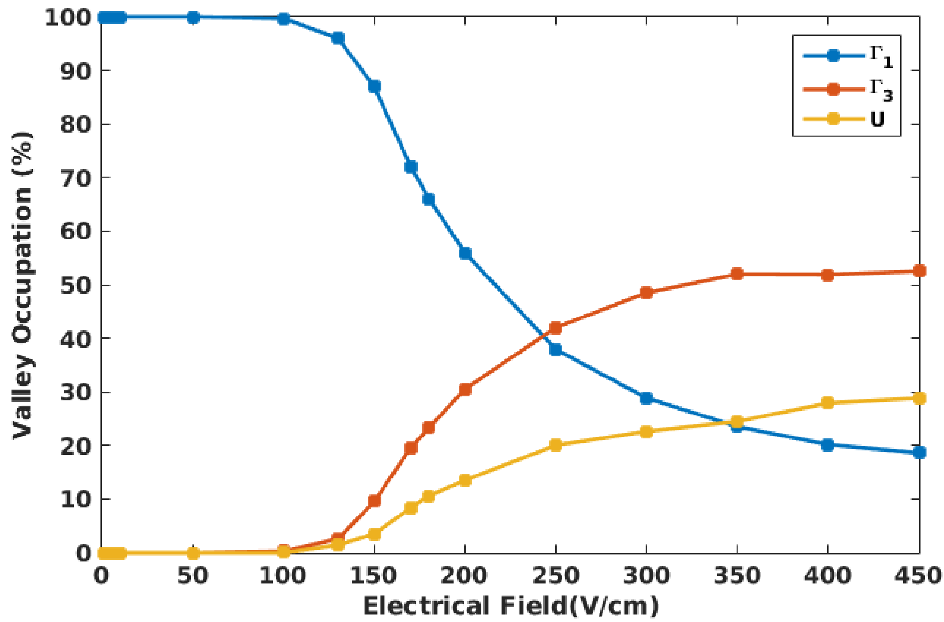

Figure 6.7: The valley occupation percentages for valleys Γ_1, Γ_3 and U versus the electric field (full range: 0 - 450kV/cm) with the impurity concentration of $10^{17}cm^{-3}$

with respect to different applied electric fields. At a low electric field, the average electron energy is too low for the electrons to be scattered into higher valleys, thus almost 100% of the time the electrons stay in the bottom-most Γ_1 valley. With an increasing electric field, the electrons are able to gain sufficient energy to be scattered into other valleys. At even higher electric fields, a population inversion occurs where more electrons stay at higher energy valleys. This coincides with the observation of the probability density of the sampled electron energy at 300kV/cm in the inset of Fig. 6.6, where the distribution mostly centers at 2eV, which is the bottom energy of valley Γ_3 and 0.1 eV away from the bottom of valley U.

Fig. 6.8 shows the plot of the drift velocity versus the electric field. The insets for Fig. 6.8 are the instantaneous velocity distributions (probability density

of the sampled values of instantaneous velocity) at selected electric fields (10kV/cm, 130kV/cm and 250kV/cm). At low electric fields (i.e. the inserted plot at 10kV/cm), the velocity distribution, which resembles a Gaussian shape, is centered around 0 with a minor shift in the negative direction as the electric field, as expressed in Equ. 6.1 and 6.3. With increasing applied electric field, the distribution is more spread out. As shown in the inset at the electric field of 130kV/cm, the distribution is shifted more towards the negative direction of the electric field. In addition, there is a minor second hump next to the main hump, this is due to the increase of the valley occupation percentages in valleys Γ_3 and U. This increase in valley occupation percentages in higher valleys is observed in Fig. 6.7, that at the electric field of 130kV/cm, the valley occupation percentages of valleys Γ_1 and U begin to show a significant increase when compared to that in the lower electric field. At higher electric fields, the electrons are scattered into other valleys, resulting in a sudden change of the reference of the momentum. This causes the shape of the velocity distribution at very high electric fields to be greatly distorted, which can be observed in the inset of Fig. 6.7 selected at the electric field of 250kV/cm.

The full range MC simulation shows a velocity overshoot behavior, with the peak velocity to be $2.83 \times 10^7 cm/s$ at the applied electric field of $130kV/cm$, and a saturation velocity of approximately $1.4 \times 10^7 cm/s$. The electric field at the peak velocity coincides with that where the valley occupation percentages begin to change significantly, as mentioned previously. Besides the change of the valley occupation percentages of the valleys, the bigger effect that is in play is that the effective mass in the higher valleys Γ_1 and U is larger than that in the Γ_1 valley. Having a higher

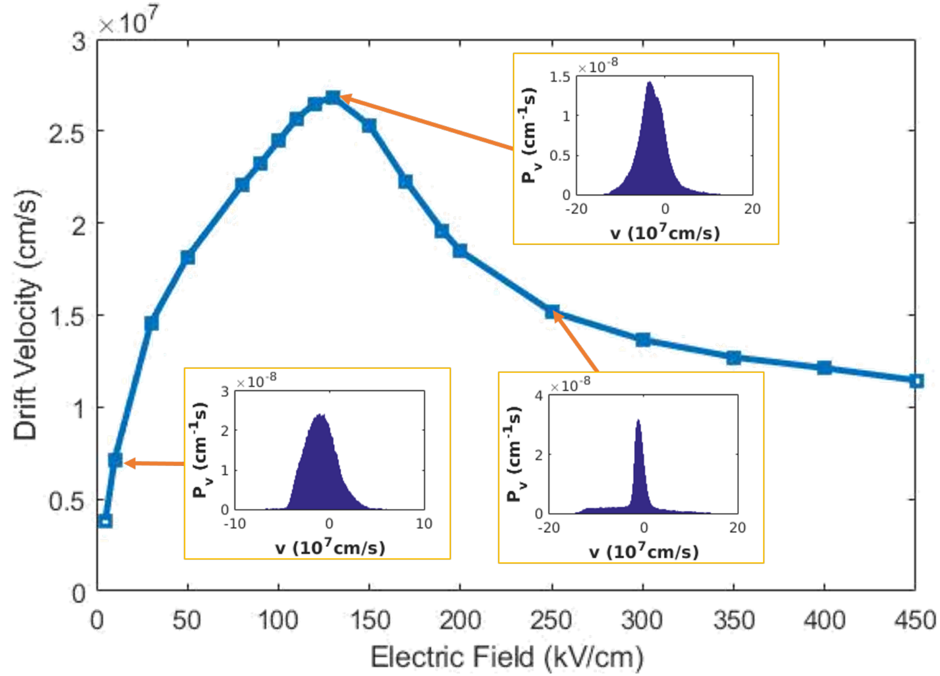

Figure 6.8: The drift velocity versus the electric field (full range: 0 - 450kV/cm) with the impurity concentration of $10^{17}cm^{-3}$. The insets are the distribution of the sampled instantaneous velocity (the probability density of the instantaneous velocity) during the simulation at selected electrical fields of 10kV/cm, 130kV/cm and 250kV/cm

effective mass means that the electron is more resistant to acceleration by the electric field when in higher valleys, thus resulting in a slowing down in velocity and the overshoot behavior in Fig. 6.8.

A comparison of the results in this work and the reported results in the literature is presented in Table 6.2.

Low-field mobility can also be obtained by extracting the slope of the curve of the drift velocity versus the electric field at the low field range. In Fig. 6.9, the values for mobility are extracted for different impurity concentration.

As mentioned previously, there are two competing effects for the impurity scat-

Table 6.2: Comparison of simulated results for GaN electron transport properties

Peak velocity (cm/s)	Saturation Velocity (cm/s)	Ref.
2.83×10^7 (@130kV/cm)	$1.3 \sim 1.4 \times 10^7$	this work
3×10^7 (@170kV/cm)	2×10^7	[55]
2.9×10^7 (@180kV/cm)	1.5×10^7	[56]
3×10^7 (@170kV/cm)	2×10^7	[57]

tering mechanisms. One is the magnitude of the scattering rate and the other is the scattering angle after the scattering events. Impurity scattering under low impurity concentration has higher scattering rate but tends to conserve the acceleration of the electron by scattering it into a smaller angle; while under high impurity concentration, the impurity scattering has lower scattering rate but tends to scatter the electron in a wider angle, thus more probable to scatter the electron in the opposite direction of acceleration.

Fig. 6.9 shows that, when impurity concentration is low, the scattering tends to conserve the acceleration, resulting in a higher mobility when compared to that with high impurity concentration, despite that the scattering rate is higher with low impurity concentration. This indicates that, in the case of impurity scattering, the smaller scattering angle conserves more acceleration than the lower scattering rate, which also makes the calculation of scattering angle a very important step in the MC simulation.

The simulation results are also compared to a collection of reported experimental data. This work's simulation results share a similar dependence on the impurity

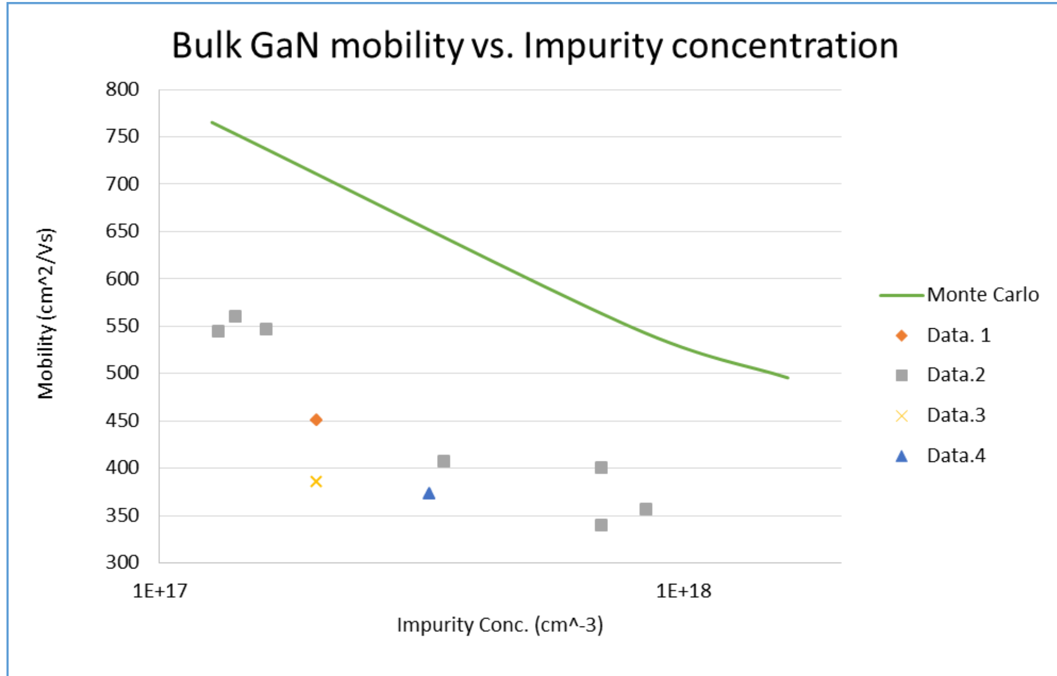

Figure 6.9: Bulk low-field mobility versus Impurity concentration extracted from MC simulation. The experimental data sets Data.1∼4 are mobility values taken from references [58],[59],[60] and [61]

concentration with the experimental data. There is also a overall up shift of the simulation results when compared to the experimental data. This is probably due to imperfections in the crystal that have not yet been accounted for in our simulations.

Chapter 7

Investigation of Electron Transport in 2D Electron Gas (2DEG)

The quantitative changes to the electron transport properties of 2DEG with respect to the change of the potential well shape is the subject of this part of the research. To understand the relationship, we first need to quantitatively describe the potential well, which is within the scope of the first 3 sections of this chapter.

After we establish the details of the shape of the potential well, we can then input this information into our developed MC simulator, with modifications to suit the quantized 2DEG wave functions. This will be explained in detail in the rest of this chapter.

7.1 Quantum Confinement of 2D Electron Gas (2DEG)

As mentioned in Chapter 1, the AlGaN/GaN heterostructure gives rise to the formation of a 2DEG layer at the interface. The accumulation of the electrons at the interface also results in a quantum confinement in the direction perpendicular to the interface. This confinement may cause changes in electron transport properties.

The most direct influence of the quantum confinement is the splitting of the conduction band into subbands, as illustrated in Fig. 7.1. Because of the splitting, the electrons no longer sit at the very bottom of the potential well, but at a certain offset above the potential well minimum. The density of states inside the potential

well becomes step-like rather than the smooth curve for the 3D density of states, as illustrated in Fig. 7.2.

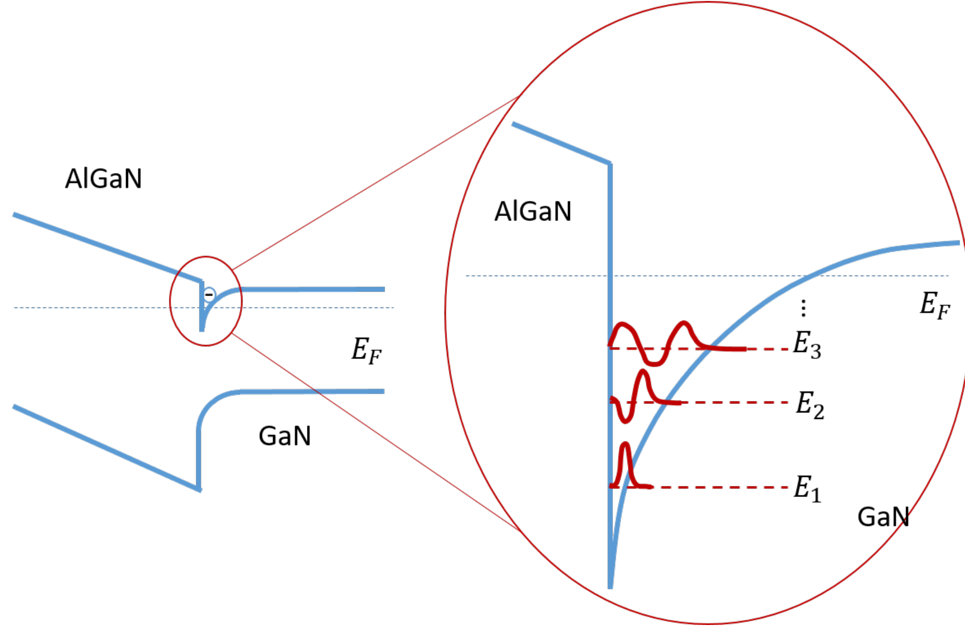

Figure 7.1: (left) Sketch of the band alignment of GaN/AlGaN heterostructure after the formation of 2DEG; (right) Zoom-in on the interface potential well and the illustration of the subband wavefunctions. E_F is the Fermi energy level, and E_1, E_2 and E_3 are the bottom energies of the 1st, 2nd and 3rd subbands.

The wave function is approximated by a product of a plane wave (φ_{xy}) parallel to the interface and a quantized component ($\varphi_n(z)$) with a dependence of z direction (defined as the direction perpendicular to the interface):

$$\Psi(\vec{r}) = \varphi_n(z)\varphi_{xy} = \varphi_n(z)e^{i(k_x x + k_y y)} \tag{7.1}$$

where:

n represents the nth subband;

k_x and k_y are the wave numbers for the x and y directions;

φ_{xy} is the xy component of the total wavefunction;

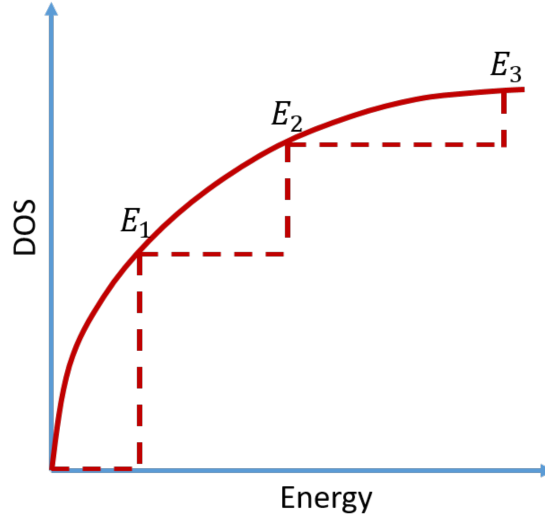

Figure 7.2: Sketch of the density of state: 3D (solid) vs 2D (dash)

$\varphi_n(z)$ is the z component of the total wavefunction at the nth subband.

The two components of the wave function are shown in Fig. 7.3. The wave function in the xy plane is assumed to be free and takes the form of plane waves, while the wave function in the z direction is determined by the shape of the potential well.

The confining potential energy resembles a triangular potential well with a transition energy level (E_t). The triangular potential well has a steepness (labeled S_{int}) of the side wall. S_{int} has units of J/m (or eV/nm for the convenience of expression in this work), which is essentially the magnitude of the electric field inside the potential well. E_t is defined as the energy level beyond which the electron is no longer confined along the z direction. A sketch of the potential well and its approximated triangular structure are shown together in Fig. 7.3.

We then substitute Equ. 7.1 into the one particle Schrödinger equation Equ. 2.1.

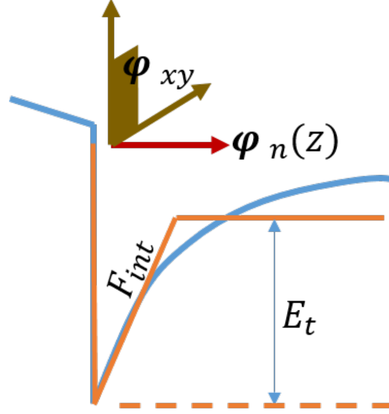

Figure 7.3: Sketch of the potential well for 2DEG at the heterostructure interface with approximated triangular potential well. S_{int} is the steepness of the triangular well and E_t is the transition energy level. The two components (φ_{xy} and $\varphi_n(z)$) of the wavefunction are also shown.

By applying separation of variables, the 3D Schrödinger equation is reduced to a 1D equation:

$$\left(-\frac{\hbar^2}{2m^*}\frac{d^2}{dz^2} + S_{int}z\right)\varphi_n(z) = E_n\varphi_n(z) \tag{7.2}$$

where:

m^* is the effective mass of electrons in GaN;

S_{int} is the steepness of the approximated triangular potential well with units of eV/nm;

E_n is the energy offset of the nth subband;

The total energy is expressed as:

$$E = E_n + \frac{\hbar^2}{2m^*}(k_x^2 + k_y^2) \tag{7.3}$$

The solution for the 1D Schrödinger equation is given as follows[64, 65, 66, 67]:

$$\varphi_n(z) = A \cdot Ai\left(\left(\frac{2m^* S_{int}}{\hbar^2}\right)^{\frac{1}{3}}\left(z - \frac{E_n}{S_{int}}\right)\right) \quad (7.4)$$

$$E_n = \left(\frac{\hbar^2}{2m^*}\right)^{\frac{1}{3}}\left(\frac{3\pi}{2}\frac{S_{int}}{n-\frac{1}{4}}\right)^{\frac{2}{3}} \quad (7.5)$$

where,

A is the normalization constant for the wave function;

$A_i(x)$ is the Airy function with argument of x;

m^* is the effective mass of electrons in GaN;

As mentioned above, the well is approximated by a triangular potential well, which is quantified by its steepness (S_{int}) and the transition energy level (E_t). S_{int} determines where the subbands start (namely the values of E_n). By comparing E_n's and E_t, one can determine how many subbands are included in the 2D triangular potential well. E_t is also used to determine what scattering mechanisms that the electron experiences under MC simulation. If the electron energy is below E_t, it is considered under 2D scattering, while above E_t is regarded as being in the 3D scattering realm.

Two examples are shown in Fig. 7.4 for subband selection. Case (a) has $S_{int} = 0.057eV/nm$ and $E_t = 0.45eV$; Case (b) has $S_{int} = 0.116eV/nm$, $E_t = 0.75eV$. After performing the calculation described in Equ. 7.4 and 7.5 to obtain different subbands, the results are presented in Fig. 7.4. As shown in the figure, the subbands that lie below E_t are selected for 2D MC, i.e. the bottom 3 subbands in Fig. 7.4(a) and the bottom 2 subbands in Fig. 7.4(b); while the ones sit above

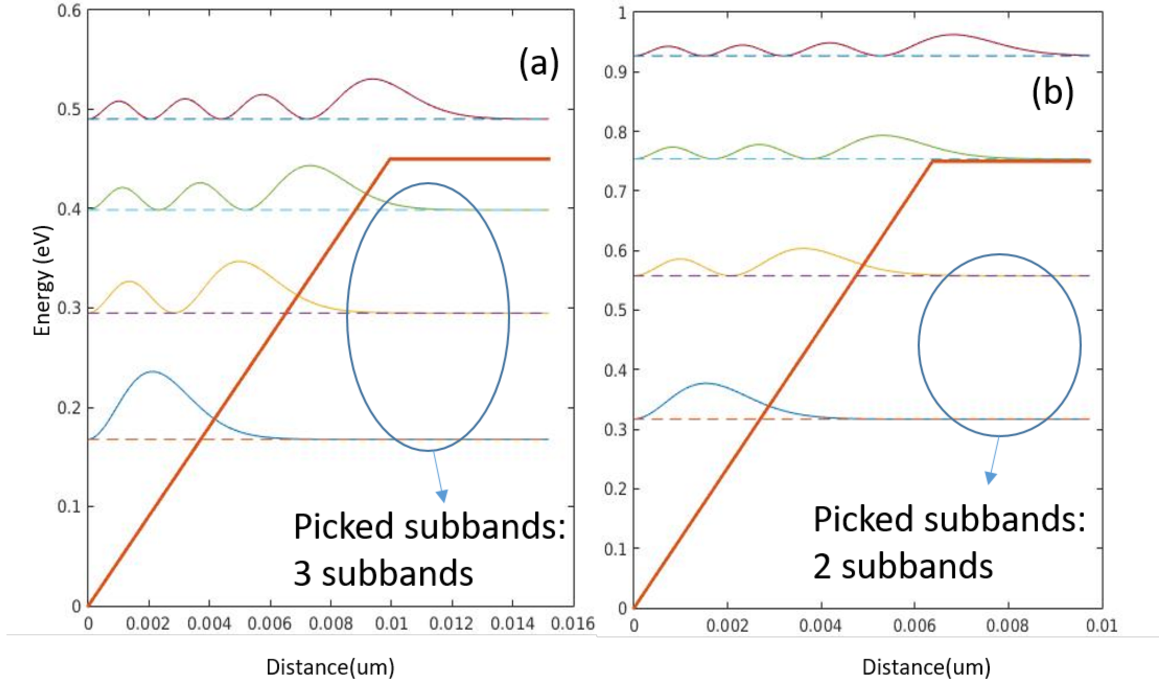

Figure 7.4: The approximated wave function $|\Psi|^2$ for two example triangular potential wells. The potential wells, which are the orange bold solid curves, are also shown together with the wavefunctions. The parameters for the two potential wells are: (a)$S_{int} = 0.057eV/nm$, $E_t = 0.45eV$; (b)$S_{int} = 0.116eV/nm$, $E_t = 0.75eV$.

E_t will be discarded and the electrons with energy higher than E_t will be simulated using bulk MC.

The MC method, which successfully simulated the electron transport for bulk GaN, is modified for use in the 2DEG simulation.

We gave a detailed description of how to calculate the scattering rates for different mechanisms in Chapter 5. To compare the scattering rates for 2D MC and bulk MC, we calculated the two most dominant scattering mechanisms (three if we split the polar optical scattering into absorption and emission components): acoustic phonon scattering and polar optical scattering, for both bulk MC and 2D

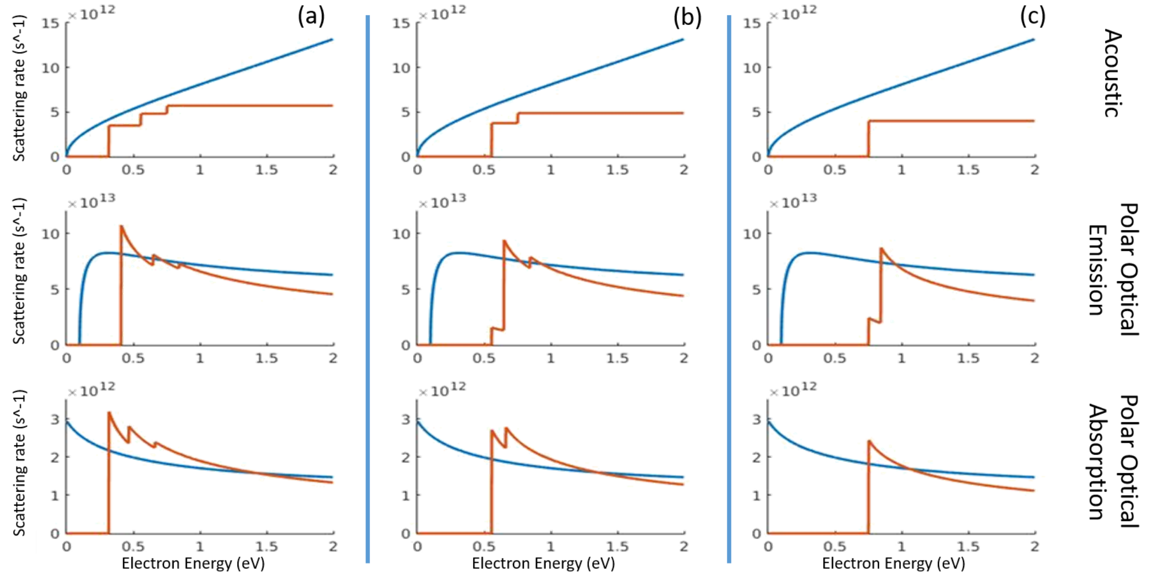

Figure 7.5: Scattering rate comparison between 3D scattering (blue) and 2D scattering (orange) with electrons residing in the 1st subband (a), 2nd subband (b) and 3rd subband, respectively. The 2D scattering rates are calculated for a triangular potential well with $S_{int} = 0.116eV/nm$ and inclusion of three subbands.

MC. A specific potential slope of $S_{int} = 0.116eV/nm$ with three included subbands is also applied to the calculation of 2D scattering rates. They are compared to each other side by side and are shown in Fig. 7.5.

As discussed in the previous section, the quantum confinement of the potential well reduces the density of states of the electrons, resulting in a step-like curve. The step-like property can also be observed in the scattering rate versus energy plot, as shown in Fig. 7.5, reflecting the sudden change in the orange curves for the 2D scattering rate versus electron energy.

The dominant scattering mechanism is polar optical emission for the 2DEG, as it is for bulk GaN. For all three scattering types, the 2D scattering rates drop below the 3D rates for sufficiently high electron energy. For the acoustic phonon scattering

mechanism, the 2D rate is consistently smaller than for the 3D rate. However, for the polar optical scattering, when electron energy is close to the bottom energy of the subbands, the 2D rates are actually higher than 3D rates.

Therefore, it cannot be concluded simply by looking at the scattering rate plot how quantum confinement affects the mobility of the electron, which indicates the necessity of further comparing the electron transport properties between bulk GaN and 2DEG.

7.2 Modeling of 2D Electron Gas (2DEG) Potential Well

The potential well formed at the interface of the heterostructure is largely a triangular shape. To address the quantum effect of the potential well, the shape of the well is approximated as a triangle with a threshold energy level, below which is the bounded region, and above which is the free electron region. Therefore there are two parameters to evaluate the potential well: 1) the slope of the potential well and 2) the height of the well.

To quantify the triangular potential well approximation, we need to determine its slope and height. We achieve this by calculating the carrier sheet density for a triangular well and equating this to the sheet density for the exact solution as given by the Poisson's equation, using the following methodology.

1. We first solve the Poisson's equation, for the AlGaN/GaN heterostructure, which gives the conduction band minimum energy as a function of position $E_c(z)$, where $z = 0$ at the interface and increases away from the interface into the GaN

region (as illustrated in Fig. 7.6).

2. The side wall of the potential well at the interface is approximated as an infinite wall.

3. The height of the well (labeled E_t in Fig. 7.6) extending into GaN is approximated by the difference between the bottom of the well and the band at the boundary of the GaN region.

4. We now calculate the slope of the well S_{int}.

4a). If the conduction band bends below the Fermi level (E_f), the slope (S_{int}) of the well is approximated using the Equ. 7.6, as shown in Fig. 7.6. We determine the slope of the well by equating the carrier sheet density (σ_{int}) at the interface given by the full Poisson's solution to that by the triangular well approximation, which in turn is given as follows:

$$\sigma_{int} = \int_0^{z_f} n_i \cdot e^{\frac{-(E_c(z)-E_f)}{kT}} dz = \int_0^{\frac{E_f - E_{c0}}{S_{int}}} n_i \cdot e^{\frac{-(zS_{int}+E_{c0}-E_f)}{kT}} dz \tag{7.6}$$

where,

$E_c(z)$ is the conduction energy minimum at location z;
z_f is the location z evaluated where $E_c(z) = E_f$;
n_i is the intrinsic carrier concentration of GaN;
E_f is the Fermi energy level of the heterostructure;
$E_{c_0} = E_c(z)$ at the interface of $z = 0$.

We then solve Equ. 7.6 for the slope (S_{int}).

4b). If the conduction band is above E_f, S_{int} is approximated as the first derivative of the conduction band minimum at the interface with respect to the

location z, as expressed in Equ. 7.7.

$$S_{int} = \frac{dE_c(z)}{dz}|_{z=0} \tag{7.7}$$

5. We then can calculate the width of the approximated well (labeled l_w in Fig. 7.6), which is obtained by dividing E_t by S_{int}, as in $l_w = E_t/S_{int}$.

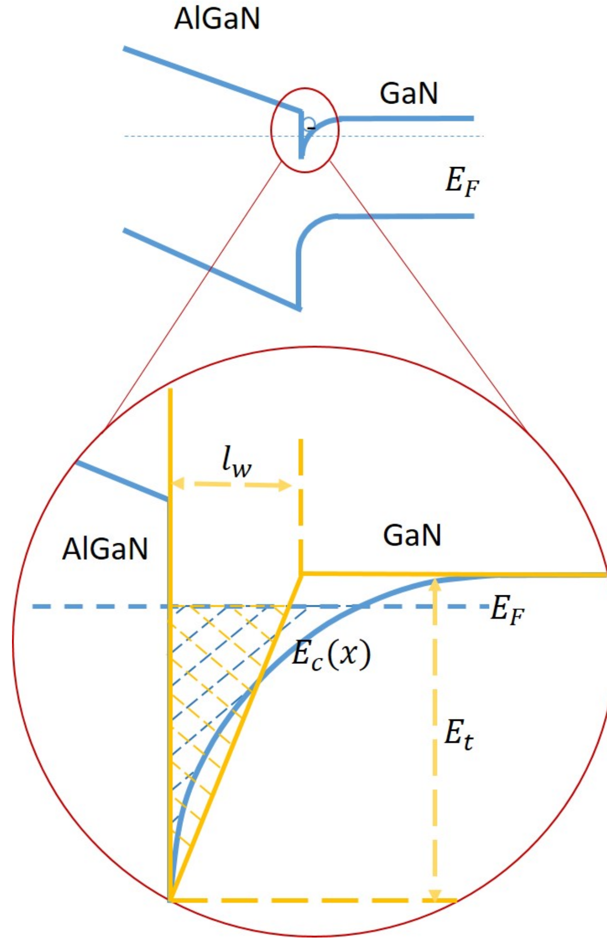

Figure 7.6: Band alignment for GaN/AlGaN heterostructure after the formation of 2DEG (top); zoom in on the interface potential well and the approximated well. The shaded areas of both the real potential well and the approximated well are of the same sheet carrier density, as is expressed in Equ. 7.6

Once we have ascertained the slope of the well, we can calculate the wave

functions and energy levels of the heterostructure potential well. By approximating the potential well near the interface as a triangular shaped well, the wave function of the electron inside the potential well can be expressed using Airy functions, as shown in Equ. 7.4 and Equ. 7.5, and again here.

$$E_n = \left(\frac{\hbar^2}{2m^*}\right)^{\frac{1}{3}} \left(\frac{3\pi}{2}\frac{S_{int}}{n-\frac{1}{4}}\right)^{\frac{2}{3}} \tag{7.8}$$

$$\psi_n(z) = A \cdot A_i\left(\zeta(z)\right) \tag{7.9}$$

$$\zeta(z) = \left(\frac{2m^* S_{int}}{\hbar^2}\right)^{\frac{1}{3}} \left(z - \frac{E_n}{S_{int}}\right) \tag{7.10}$$

Equ. 7.8 describes the separation of the subbands of the electrons inside the approximated potential well, while E_t determines how many subbands are inside the well. Equ. 7.9 expresses the wave function along the z direction, which is necessary for the calculation of the scattering rates associated with 2DEG.

7.3 Investigation of the Relationship Between 2D Electron Gas (2DEG) and Potential Well Structure Parameters

To establish the relationship between the sheet density of the 2DEG (σ_{int}) and the structural parameter of the potential well, a Poisson's equation solver is developed to calculate and evaluate the band alignment across the GaN/AlGaN heterostructure and the potential well at the interface.

To study the relationship between σ_{int} and the potential well structure parameters, a set of variables for the heterostructure is chosen to be evaluated. The

Table 7.1: GaN/AlGaN heterostructure parameters for Poisson's equation solver.

parameter name	value
x [b]	1 [a], 0.6, 0.2
L_{GaN} [c] (μm)	1.0[a], 1.2, 1.4, 2.0
L_{AlGaN} [d] (nm)	15, 20[a], 25 ,30
N_{int} [e] (cm^{-2})	10^{12}, 5×10^{12}, 8×10^{12}, 10^{13} [a], 2×10^{13}, 3×10^{13}, 4×10^{13}, 5×10^{13}
N_{Ga} [f] (cm^{-3})	10^{13},10^{14},10^{15}, 10^{16} [a], 10^{17}, 10^{18}

[a] Default values for the structure, when other parameters are changed according to the table.

[b] Mole fraction of Al in $Al_xGa_{1-x}N$

[c] GaN region length of GaN/AlGaN heterostructure

[d] AlGaN region length of GaN/AlGaN heterostructure

[e] Polarization induced interface charge sheet density

[f] GaN region body doping density

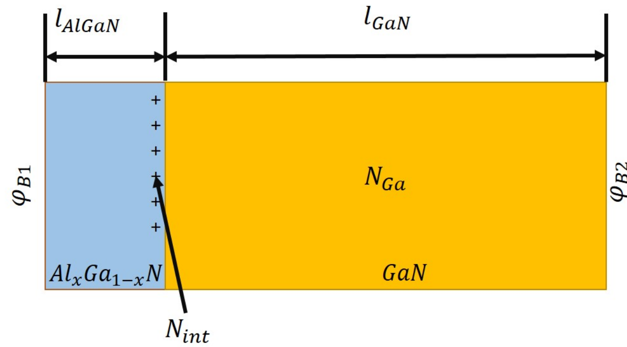

Figure 7.7: Schematic of the simulated AlGaN/GaN heterostructure

heterostructure parameters and the simulated variables are presented in Table 7.1. The parameters included in the simulations are: mole fraction of Al in AlGaN (x), GaN region thickness (L_{GaN}), AlGaN region thickness (L_{AlGaN}), interface fixed charge (N_{int}) and GaN region body doping concentration (N_{Ga}). The change in x mostly affects the permittivity of AlGaN. The inclusion of N_{int} is to mimic the effect of the polarization induced charge at the interface. The intentional doping in GaN is unnecessary but the background doping concentration in GaN can vary and is usually on the level of $10^{16}cm^{-3}$[68, 69, 70]. Therefore it is necessary to see how different body doping concentrations can affect the simulation. The schematic of the simulated GaN/AlGaN is shown in Fig. 7.7.

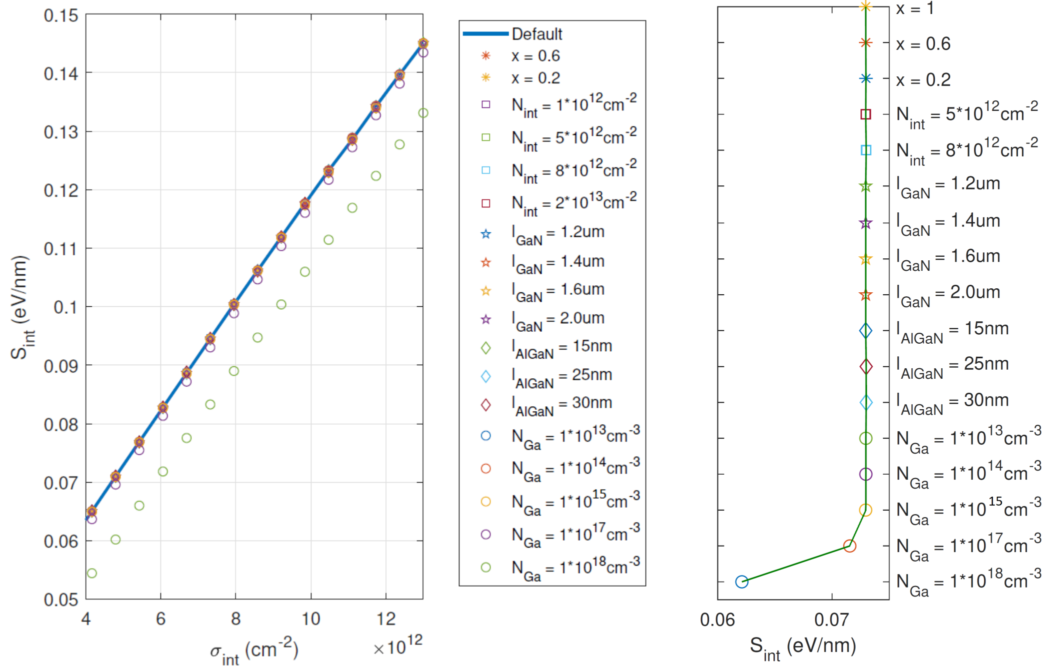

Figure 7.8: (feft): S_{int} vs. σ_{int}. Each curve is calculated with one parameter changing from the default value. The changed parameter is labeled as the legend of the curve. (right): S_{int} vs. selected parameters in the right graph with σ_{int} chosen at $3 \times 10^{12}cm^{-2}$.

In this simulation, the structural parameters of the heterostructure start with the default values given in Table 7.1, which are labeled with superscript [a]. After each calculation, the process of approximating the potential well mentioned in the previous section is conducted to obtain the information of the triangular potential well (S_{int}, E_t, l_w, and σ_{int}). By sweeping the boundary potential in the AlGaN region, a series of S_{int}, E_t, l_w, and σ_{int} can be obtained. Such a process is repeated by changing the value of one parameter at a time.

After the calculation, we plotted S_{int} versus σ_{int} to begin with in Fig. 7.8 (left) to see if there exists a correlation between σ_{int} and S_{int}.

In Fig. 7.8 (left), each curve represents the results for a specific set of structural parameters for the GaN/AlGaN heterostructure with sweeping of the boundary potential. We can observe in Fig. 7.8 (left) that all the curves overlap from simulation to simulation, with the only exceptions being when the altered parameter is N_{Ga}. This indicates a strong correlation between S_{int} and σ_{int} despite the change of most of the structural parameters presented in Table 7.1. The discrepancies between the simulations are plotted in Fig. 7.8 (right), with the y axis being the parameters changed for the simulation and x axis being the S_{int} values exacted at σ_{int} of $3 \times 10^{12} cm^{-2}$ from Fig. 7.8 (left). The significant deviation happens when N_{Ga} increases above $10^{17} cm^{-3}$, while the rest of the values stay at a constant level of approximately 0.072 eV/nm with negligible differences between them.

What needs to point out here is that the chosen parameters in Table 7.1 are not entirely unrelated to each other. This work treats them as independent parameters and changes their values individually. The relationships between the

chosen parameters are ignored in this work due to the reasoning as follows.

A fixed correlation between σ_{int} and S_{int} is obtained by our calculations. This fixed correlation stays true even if we treated the parameters independently, which is a stronger constrain on the fixed correlation. Therefore, it is reasonable to conclude that even we take into consideration that some of the parameters are related, we can still obtain the same fixed correlation.

The only parameter that can alter this correlation is the body doping concentration in the GaN region (N_{Ga}). Nonetheless, as mentioned previously, the GaN/AlGaN structure can achieve the 2DEG layer without any intentional doping in either region, and the background body doping of state-of-the-art GaN can reach below $10^{16} cm^{-3}$ level [68, 69, 70], which is below the level of N_{Ga} that begins to effect the fixed correlation between S_{int} and σ_{int}. The background doping concentration won't change for a specific manufacturing process and the intentional doping is not desirable for the GaN/AlGaN heterostructure based devices. Therefore, it is reasonable to assume that the body doping concentration of GaN region is a constant instead of a variable. For the simplicity of further discussion, the body doping concentration of N_{Ga} is fixed at $10^{16} cm^{-3}$ for further simulations.

For an unchanged N_{Ga}, S_{int} and σ_{int} are correlated with each other with negligible dependence on the structural parameters given in Table 7.1, with the exception of N_{Ga}.

In Fig. 7.9, both the depth and the width of the approximated triangular potential well (denoted E_t and l_w, respectively) are plotted versus σ_{int}. The process is similar to that in Fig. 7.8, albeit without the calculations altering N_{Ga} for the

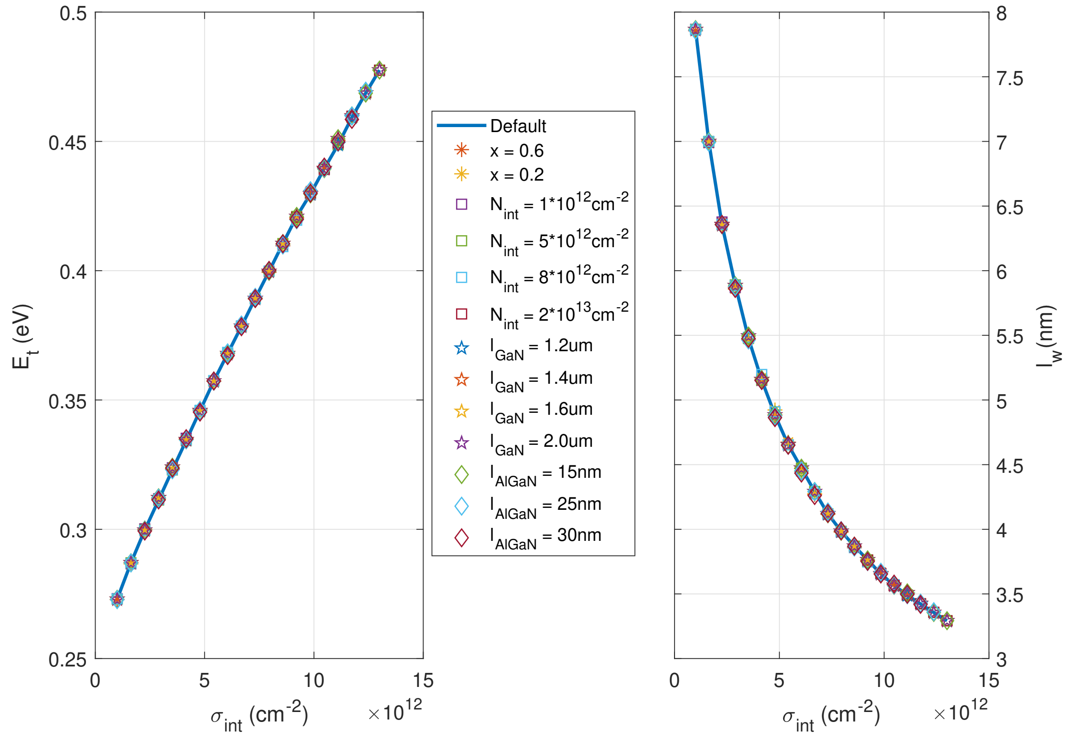

Figure 7.9: Left: E_t vs. σ_{int}. Right: l_w vs. σ_{int}. Each curve is calculated with one structural parameter changing from the default value. The curves with the solid line represent the results of the structure with the default parameters given in Table 7.1 and super-scripted with "a". The legend of each curve represents the altered parameter.

reasoning given above.

In the simulated case, the curves overlap with each other with negligible differences between one another for both E_t versus σ_{int} and l_w versus σ_{int}, indicating that both E_t and l_w have fixed correlations with σ_{int}. These two correlations also have little dependence on the parameters given in Table 7.1, with the exception of N_{Ga}, as it is for the correlation between S_{int} and σ_{int}. As shown in Fig. 7.9, E_t increases with increasing σ_{int} while l_w decreases with increasing σ_{int}. Based on Equ. 7.6, E_t

affects σ_{int} exponentially. Therefore, the increasing trend of E_t versus σ_{int} is more dominant than the decreasing trend of l_w versus σ_{int}.

7.4 Set up for 2D Electron Gas (2DEG) Monte Carlo (MC) Simulation

As mentioned above, the potential well height E_t divides the interface into two regions of energy. The region below E_t is considered to be inside the potential well, where scattering mechanisms are coupled with the 2D wave functions described in Equ. 7.9; while the region above E_t is the bulk, in which electrons are subjected to bulk, or 3D scattering mechanisms.

As the potential well and charge density at the interface are described and connected by Poisson's equation, the shape of the potential well is correlated to the charge density distribution. The correlation is partially shown in Fig. 7.10, where E_t is plotted against S_{int}. This curve provides values that can be used to quantitatively describe the approximated potential well, thus providing input into our 2D MC simulation.

In Fig. 7.10, the first three subbands energy are calculated using Equ. 7.8 and are plotted against S_{int}. Together with the three curves of subbands energy is the potential well height E_t, as mentioned above. The curve of E_t versus S_{int} can be obtained because both E_t and S_{int} have fixed correlations with σ_{int}. The two dashed vertical black lines in Fig. 7.10 divide the plot into three regions R1, R2 and R3. In R1, the potential well height curve (labeled 'E_t') sits above all three subband energy

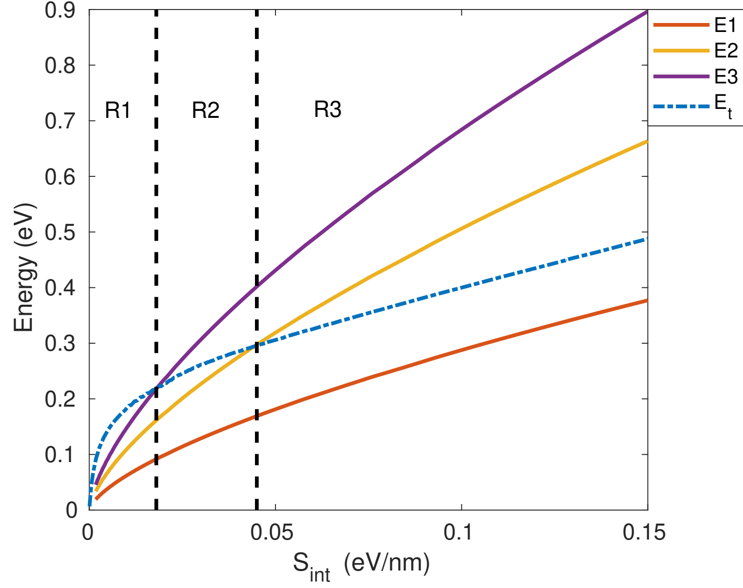

Figure 7.10: The first three subband energy levels $(E_1, E_2, E_3)$and E_t are plotted against their correlated S_{int}. The black dash lines are located at $S_{int} = 0.045eV/nm$ and $S_{int} = 0.018eV/nm$, dividing the graph into regions R1, R2 and R3.

curves (labeled 'E_1', 'E_2' and 'E_3', respectively). In this case, when conducting the MC simulation using S_{int} in region R1 as the potential well structural parameter, three subbands should be included in the simulation. Similarly, when using S_{int} in region R2, the bottom two subbands below E_t should be included in the MC simulation. Only the lowest subband is included in the MC simulation if choosing S_{int} from region R3.

The scattering mechanisms included in the MC simulation are: acoustic phonon scattering, polar optical scattering, piezoelectric scattering, impurity scattering (only for bulk MC) and intervalley scattering (only for bulk MC). The parameters for the included scattering mechanisms are given in Table 6.1. For our MC simulation, the primary sweep will be the electric field being applied parallel to the interface of the

heterostructure, ranging from 2kV/cm to 450kV/cm. Our secondary sweep is the potential well slope S_{int} ranging from 0.03 eV/nm to 0.23 eV/nm.

The correlation between the approximated potential well slope S_{int} and the potential well height E_t shown in Fig. 7.10 above is used in the MC simulation. This indicates that for a chosen S_{int}, there is only one corresponding E_t, thus making our secondary sweep of S_{int} sufficiently thorough to investigate the effects of the potential well shape on the electron transport properties of 2DEG.

A single MC simulation is constructed in a manner similar to that of the bulk MC simulation described in Chapter 6, albeit with two parameters used as input: a S_{int} as the potential well parameter and a specific electric field.

7.5 Results and Analysis

The simulations are divided into two major parts: 1) a high electric field simulation ($10kV/cm$ to $450kV/cm$) and 2) a low electric field simulation ($2kV/cm$ to $10kV/cm$).

7.5.1 High Electric Field Simulation

In Fig. 7.11, the drift velocity is plotted against a range of electric field from 10 to 450 kV/cm with selected potential well slopes S_{int} = 0.178, 0.072 and $0.030 eV/nm$, as well as the bulk MC simulation. The curves represent the average values of all the repeated simulations. The bar at each simulated point is the upper and bottom limits of all the repeated simulations.

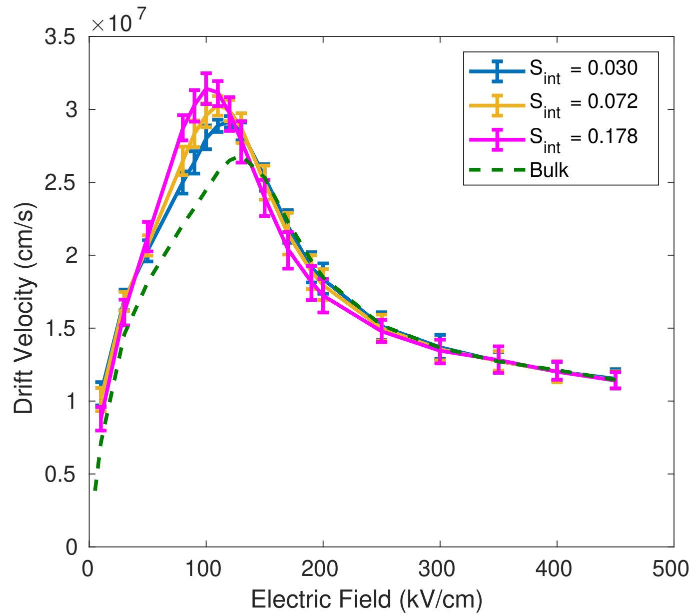

Figure 7.11: Velocity versus electric field at S_{int} = 0.03, 0.072, 0.178 eV/nm.

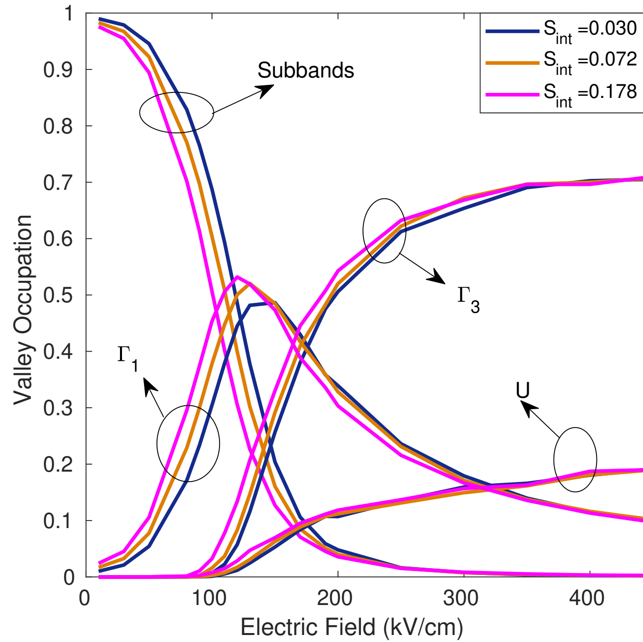

Figure 7.12: Valley occupation percentages versus electric field at S_{int} = 0.03, 0.072, 0.178 eV/nm and Bulk. The Γ_1 valley occupation only includes the electrons that are inside the Γ_1 valley but above E_t thus outside the potential well.

Comparing the three selected 2D MC cases to the bulk MC case, we observe an obvious shift upward of the drift velocity curves, especially in the range of $<$ $150kV/cm$. This indicates a higher drift velocity of 2DEG than that of free bulk electrons. When comparing between the three 2D MC cases, we observe that smaller S_{int} tends to give bigger drift velocity in the low electric field region ($< 50kV/cm$). When the electric field increases above $50kV/cm$, the larger S_{int} begins to give a bigger drift velocity.

The drift velocity is affected by S_{int} in a different way in the low electric field region ($< 50kV/cm$) than in the mid-region ($50 \sim 100kV/cm$). This can be explained if we revisit Fig. 7.10. By examining the difference between E_t and E_1, we see that ΔE=E_t-E_1 tends to decrease with increasing S_{int} within the range of interest ($S_{int} > 0.02eV/nm$). Although smaller S_{int} gives higher drift velocity in the low electric field region, electrons need to gain sufficient energy to leave the potential well (overcome ΔE) to further gain energy, thus achieving higher drift velocity. The larger ΔE for smaller S_{int} appears to be "trapping" the electron inside the potential well, preventing them from going out of the potential well to gain more velocity. This is shown in Fig. 7.12, where the subband occupation tends to decrease faster with increasing electric field, when S_{int} of such a curve is bigger.

Around the electric field of $\sim 100kV/cm$, the drift velocity curves reach a peak. This peak velocity is called the "overshoot velocity". The reason for such behavior is that the electrons begin to occupy the upper valleys (Γ_3 and U). As noted in Table 6.1, if electrons reside in the upper valleys, they have a bigger effective mass. This "heavier" effective mass causes electrons to have smaller velocity, with the same

energy, when compared to electrons with smaller effective mass. When the electron gains sufficient energy to surpass the lowest energy of the higher valleys, and is scattered into those valleys, the electron becomes "heavier" to be accelerated in the electric field, resulting in a decrease in the drift velocity versus electric field curve. A comparison of Fig. 7.11 and Fig. 7.12 reveals that the overshoot velocity happens in the same electric field where valley occupation percentages in valleys Γ_3 and U begin to increase significantly. The effects of different S_{int} on peak velocity, and the electric field in which the peak velocity occurs, are further shown in Fig. 7.13.

As shown in Fig. 7.13, peak velocity tends to increase and then flatten with increasing potential well slope S_{int}. Peak velocity stabilizes when $S_{int} > 0.11eV/nm$. Electric field at peak velocity, however, decreases and then flattens with increasing S_{int}.

When the electric field increases even higher ($> 250kV/cm$), the difference between cases with different S_{int} becomes increasingly smaller, until it is negligible at the highest simulated electric field ($450kV/cm$). At this level of electric field, almost all electrons are out of the potential well (as is shown in Fig. 7.12), in the range of $> 300kV/cm$. Since the electrons are out of the well, the effects of S_{int} on the drift velocity curves become negligible, thus explaining the "converging" behavior of the drift velocity curves in Fig. 7.11 in the high electric field region.

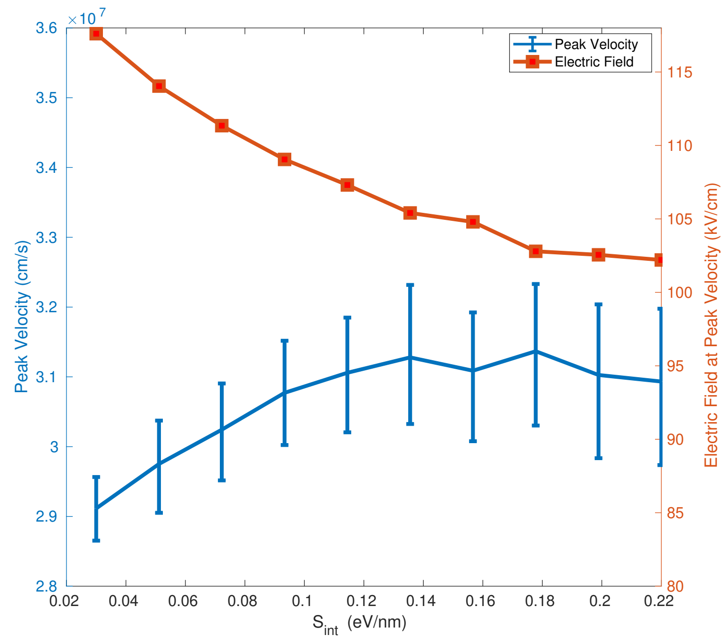

Figure 7.13: (Blue curve) interpolated peak velocity versus S_{int}. (Red curve) electric field to achieve peak velocity versus S_{int}.

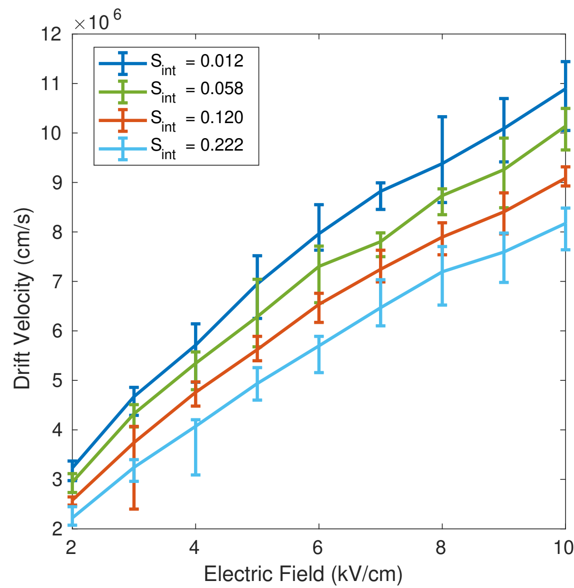

Figure 7.14: Drift velocity versus electric field at S_{int} = 0.012, 0.058, 0.120, 0.222 eV/nm.

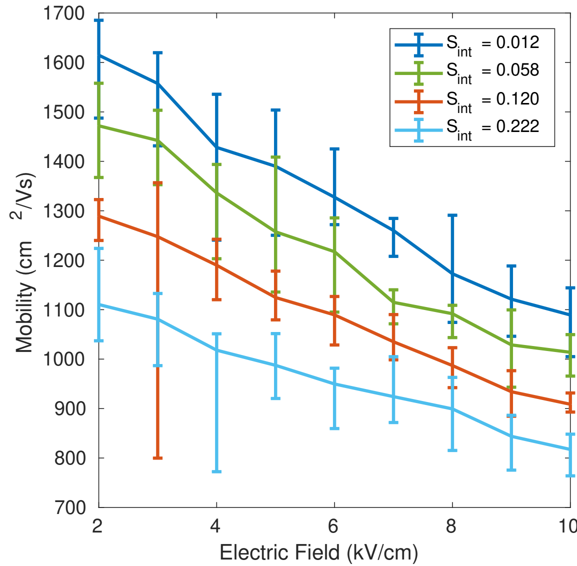

Figure 7.15: Mobility vs. electric field at S_{int} = 0.012, 0.058, 0.120, 0.222 eV/nm.

7.5.2 Low Electric Field Simulation

In Fig. 7.14, drift velocity is plotted against the applied electric field ranging from $2kV/cm$ to $10kV/cm$. Each point is the average value of multiple independent simulations and the error bar represents the range of all simulation results. Four cases with different S_{int} are selected with S_{int} = 0.012, 0.058, 0.120, 0.222 eV/nm, respectively. The effect of S_{int} on drift velocity in the low electric field range is briefly described in Section 7.5.1 and will be further discussed in this section.

In Fig. 7.14, we can again observe a continuous down shift of the drift velocity curve with increasing S_{int}. Fig. 7.15 shows mobility versus the electric field. The mobility is calculated by dividing the electric field by the drift velocity ($\mu = v/E$). Mobility tends to decrease with increasing electric field as well as with increasing S_{int}, as shown in Fig. 7.15.

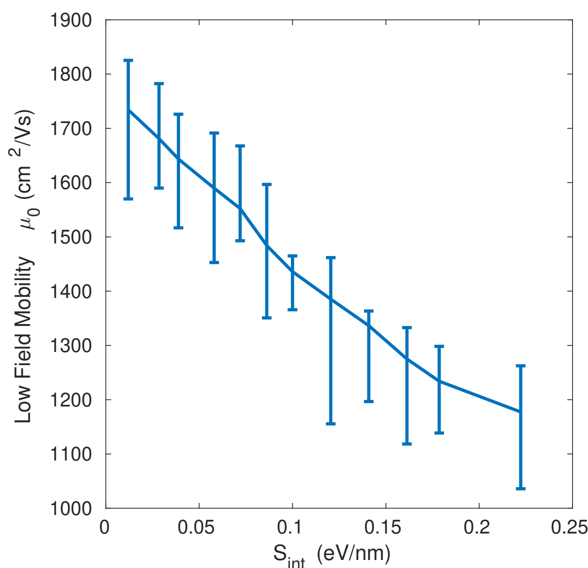

Figure 7.16: Low-field mobility (μ_0) vs. potential well slope (S_{int}).

A low field mobility μ_0 is extracted from Fig. 7.15 for each applied S_{int}. It is achieved by approximating each mobility versus electric field curve using linear interpolation and tracing back to where electric field equals 0 to get the value. The interpolated value is recorded as μ_0 for each 2D MC simulation with a given S_{int}. The results of μ_0 versus S_{int} are shown in Fig. 7.16. The error bar represents the range of results from multiple simulations. Fig. 7.16 shows that the low-field mobility μ_0 decreases with increasing S_{int}. The simulated S_{int} ranging from $0.03 \sim 0.23\ eV/nm$ gives a reasonable interface sheet density ranging from $\sim 5{\times}10^{10}$ to $\sim 2.5{\times}10^{13}cm^{-2}$, and the 2DEG layer has a μ_0 of $> 1170cm^2/Vs$, which is a significant increase when compared to bulk mobility which is evaluated at $\sim 800cm^2/Vs$ in our simulation.

As discussed in the previous sections, there is a fixed correlation between S_{int} and σ_{int}, which is shown in Fig. 7.8. Because of this correlation, we switched the x

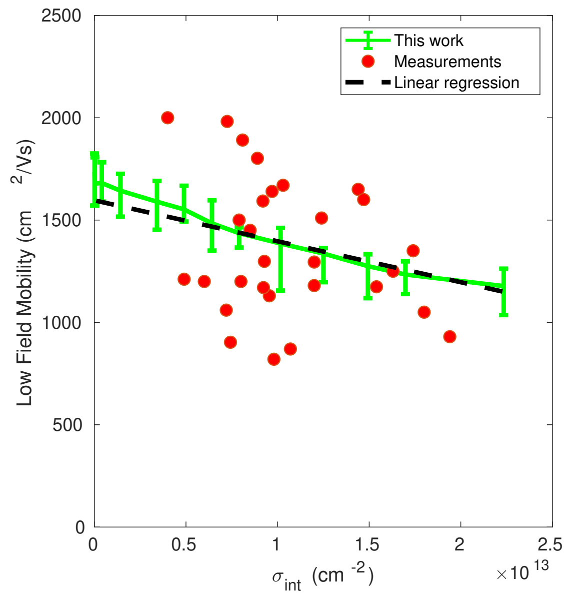

Figure 7.17: Low-field mobility (μ_0) vs. the density of 2DEG (S_{int}). The scattered points are experimental measurements reported in the literature[59, 61, 71, 72, 73, 74, 75, 76, 77, 78, 79, 80]. The dashed line is the linear regression of the experimental data.

axis in Fig. 7.16 from S_{int} to σ_{int}, which allows us to directly compare our simulation results with other experimentally measured low-field mobility with reported interface sheet carrier density[59, 61, 71, 72, 73, 74, 75, 76, 77, 78, 79, 80]. The rearranged μ_0 versus σ_{int} is plotted in Fig. 7.17. The experimental measurements are also plotted alongside our simulation in the figure as the scattered points. We also conducted a linear regression on the collected experimental measurements, which is presented as the dashed line in Fig. 7.17. A strong agreement is observed between our calculation and the linear regression of the collected data, especially in the high sheet density region ($\sigma_{int} > 5 \times 10^{12} cm^{-2}$).

Chapter 8

Gallium Nitride (GaN) Device Overview and Simulation

This work investigates the electron transport properties of 2DEG at the interface of the GaN/AlGaN heterostructure. In the last chapter, we conducted MC simulations on the 2DEG with consideration of the effects of the shape of the potential well. We mentioned in Chapter 1 that the superior material properties of the 2DEG at the interface of the GaN/AlGaN heterostructure is utilized in applications such as HEMTs. In this chapter, we use the simulation results from our in-house MC simulator, notably mobility, and implement them in our chosen TCAD simulator to investigate two of the GaN devices that include the GaN/AlGaN heterostructure: lateral HEMT and vertical Current Aperture Vertical Electron Transistor (CAVET). The TCAD simulator of our choice is the open source version of the Genius Semiconductor Device Simulator, which has the ability to conduct 2D device simulation; implement drift-diffusion model and a range of mobility models, and so on (source: https://github.com/cogenda/Genius-TCAD-Open).

The schematics of the two devices of interest are shown in Fig. 8.1 and Fig. 8.2. The devices share a similar stacking of the GaN/AlGaN heterostructure near the surface. A 2DEG layer is formed at the interface due to the process described in Chapter 1. A lateral HEMT shown in Fig. 8.1 uses this 2DEG layer as the channel to conduct from the source to the drain, and the current mostly flows laterally at the

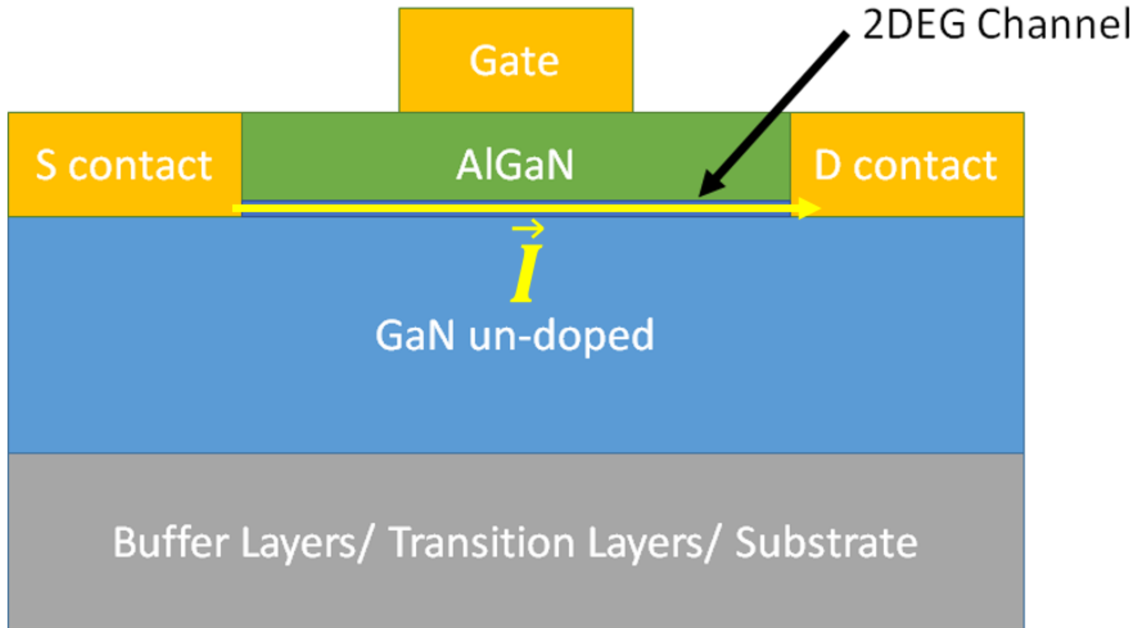

Figure 8.1: Schematic of a GaN/AlGaN based HEMT.

interface. A CAVET shown in Fig. 8.2 uses this 2DEG layer to connect the sources to the drift region. Because the drain is at the back side of the wafer, the current is drawn downwards towards the drain. The current is concentrated under the gate by adding a current blockling layer (CBL) between the unintentionally doped (UID) GaN layer and the drift region, with an aperture of n-type GaN to allow current to flow through, so that the gate can have better control over the on/off state of the device. The direction of the current flow when the device is on and conducting is also illustrated in both figures.

Both lateral and vertical GaN devices have their advantages and disadvantages. Lateral devices usually have low parasitic capacitance, thus we can expect lower conduction loss and lower switching losses[81]. They are also easier to fabricate. It is much easier for lateral devices to obtain bi-directional switching[82, 83]. However

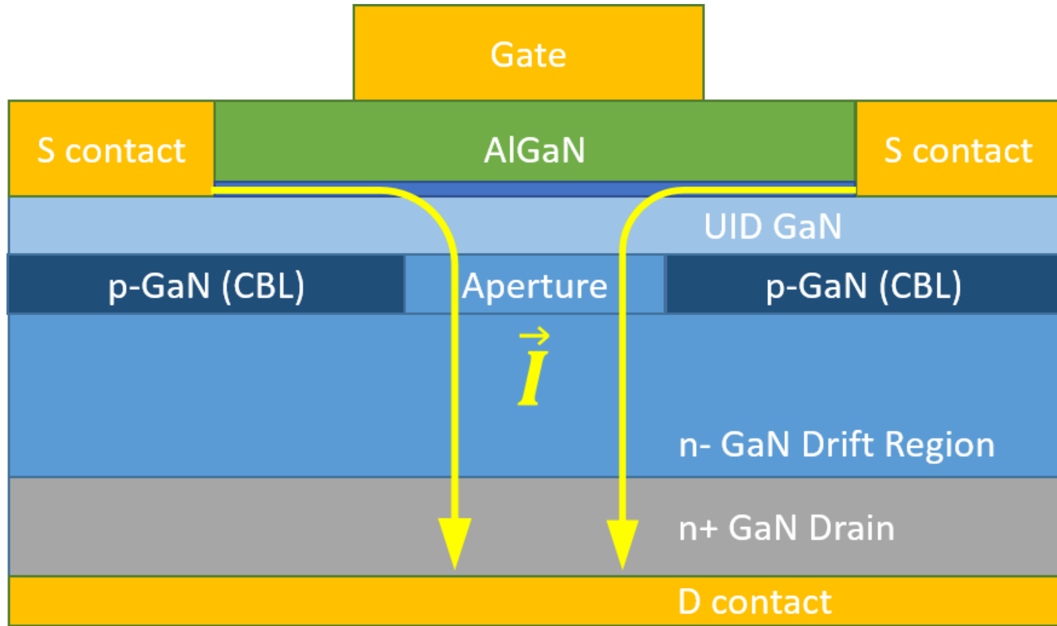

Figure 8.2: Schematic of a GaN/AlGaN based CAVET.

for lateral devices, increasing the breakdown voltage of the device causes an increase in chip sizes. Also, the current flows near the device surface, thus the surface quality affects the current flow. The existence of traps at the surface and interface is known to cause current collapse phenomenon and an increase in dynamic on-resistance[84].

While on the other hand, vertical devices require high quality native substrate (GaN substrate), which is very expensive at present. The fabrication of vertical devices is more complex than that of lateral devices. The advantages of the vertical devices are due to the increase in breakdown voltage increasing the thickness of the device rather than the chip sizes. This contributes to a higher power density. In addition, the current does not just flow on the interface, but also through the bulk region, which is expected to have less current collapse[81].

Table 8.1: Key parameters for the simulated HEMT.

Parameter	Label	Value
AlGaN layer thickness	t_{AlGaN}	30 nm
Gate to source length	l_{gs}	1 μm
Gate length	l_g	6 μ m
Gate to drain length	l_{gd}	2 μm

8.1 Device Simulation of High Electron Mobility Transistor (HEMT)

A device configuration for HEMT is set up in Genius. The meshing of the simulated device is shown in Fig. 8.3. The key parameters are presented in Table 8.1. The GaN region is doped with a concentration of $10^{16} cm^{-3}$ as a typical background doping concentration of the material. The AlGaN region is also doped $10^{16} cm^{-3}$ as an assumption that AlGaN shares a similar background doping concentration as that of GaN material. The thickness of the GaN layer is set at approximately 3 μm so that the connection of the substrate is considered sufficiently far from the GaN/AlGaN heterostructure interface. In addition, the bottom of the substrate is doped p-type with a concentration of $10^{15} cm^{-3}$ to ensure a good insulation from the surface active area. A sheet layer of fixed charge with a concentration of $10^{13} cm^{-2}$ is applied at the interface of the heterostructure to represent the polarization induced charge. The device width in the third dimension is set at 1 μm.

The first simulation is done on this structure to obtain the drain current I_d versus gate voltage V_{gs} characteristic. The plot is shown in Fig. 8.4. V_{gs} ranges from -15V to 0V, with a drain bias V_{ds} of 0.02V. As shown in Fig. 8.4, the threshold

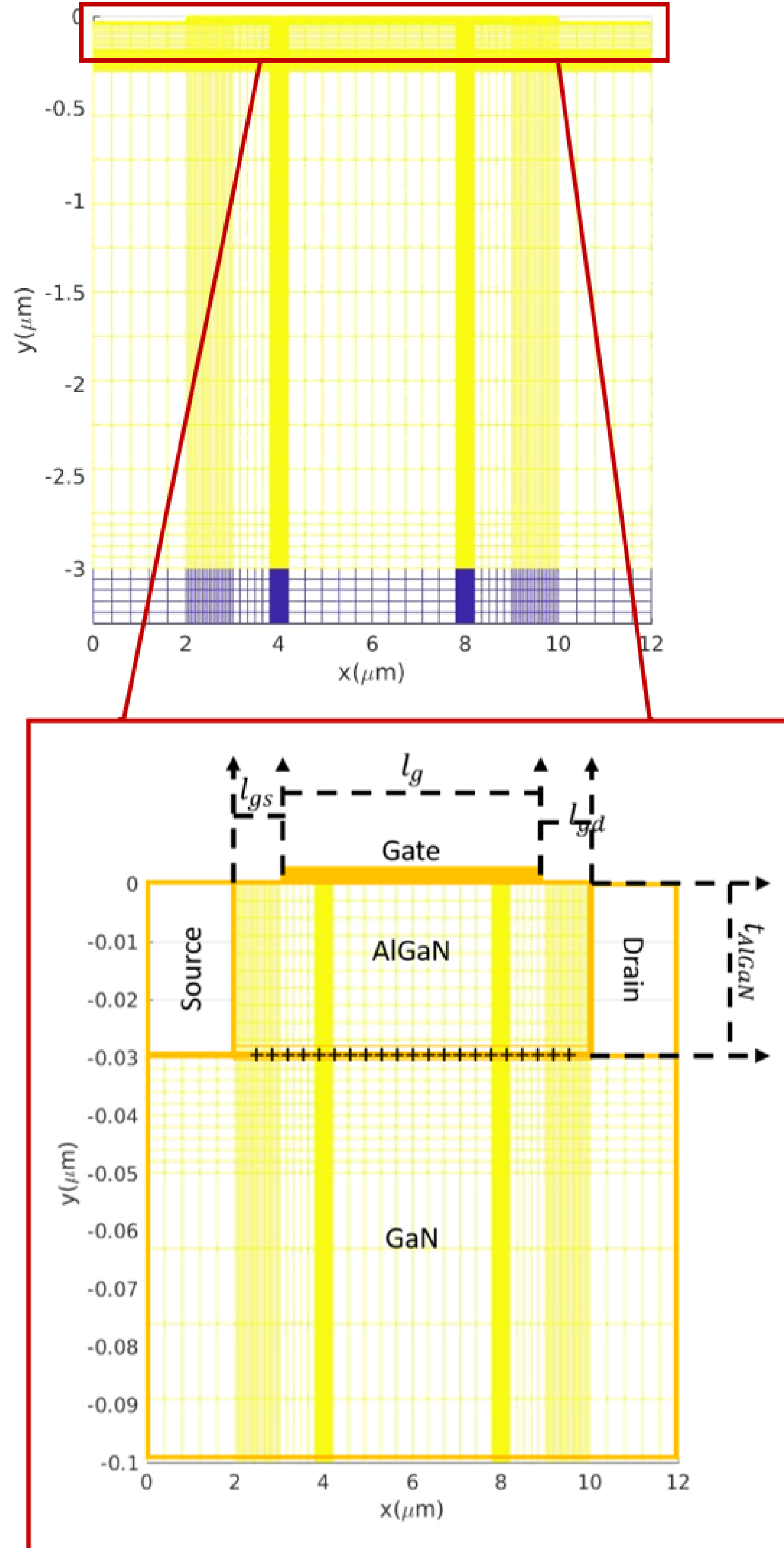

Figure 8.3: Meshing for the simulation of the lateral HEMT and illustration of the parameters presented in Table 8.1.

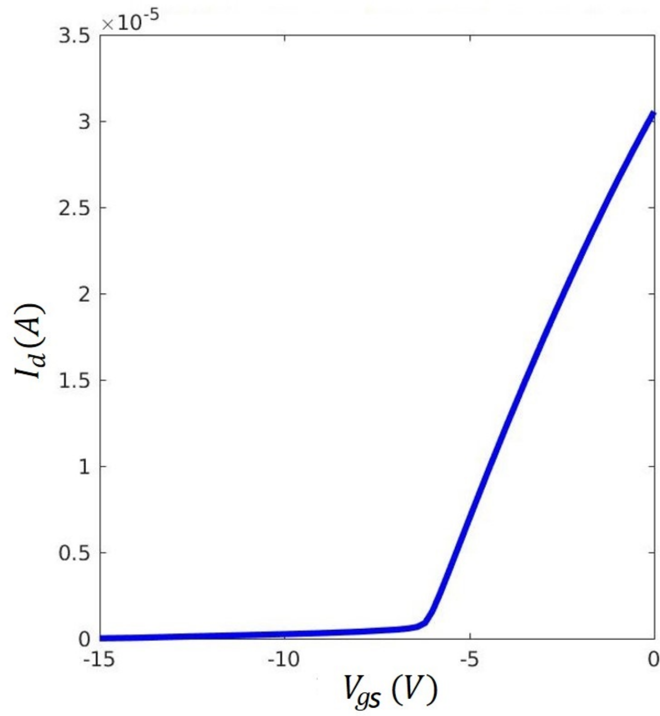

Figure 8.4: I_d versus V_{gs} characteristic of the simulated lateral HEMT with V_{ds}=0.02V.

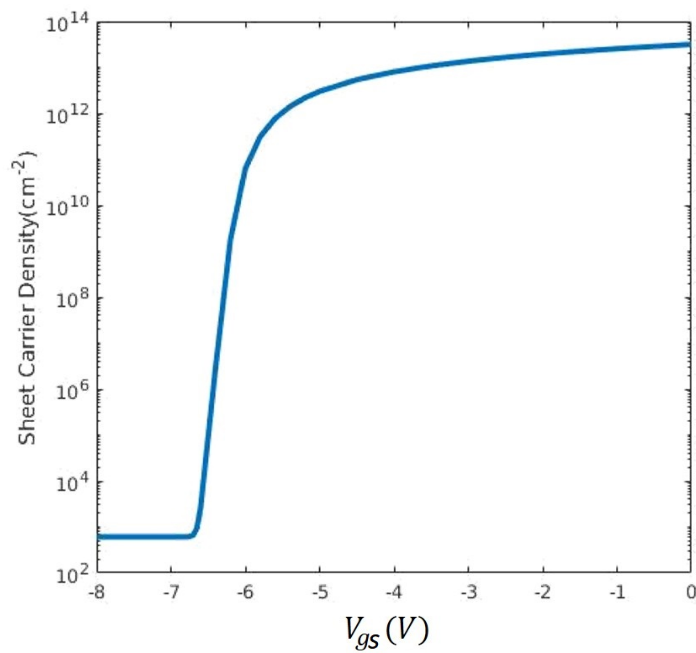

Figure 8.5: Sheet electron density at the heterostructure interface versus V_{gs} with V_{ds}=0.02V for the HEMT.

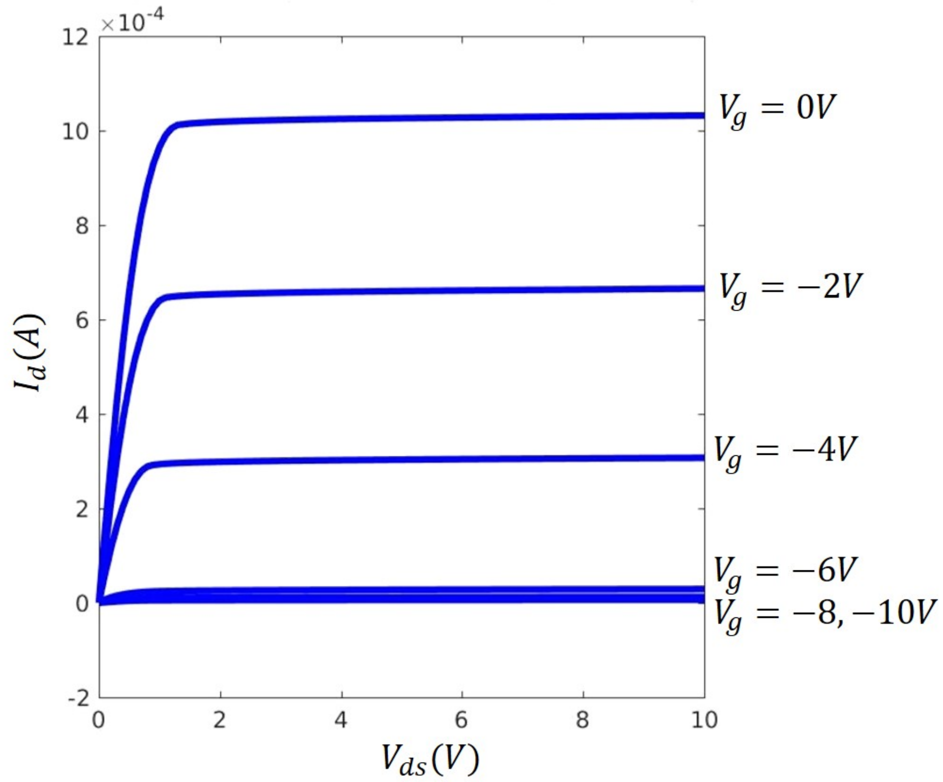

Figure 8.6: I_d versus V_{ds} at various gate voltages of V_{gs}=0V, -2V, -4V, -6V, -8V and -10V for the HEMT.

of the simulated device is approximately -6V, which indicates that this device is a normally-on device. The interface carrier sheet density is also extracted and shown in Fig. 8.5. At V_{gs} = 0V, the carrier sheet density is at the level of $10^{13} cm^{-3}$, indicating the existence of a conducting channel between the source and the drain.

A plot of I_d versus V_{ds} characteristics curves is also obtained. The results are presented in Fig. 8.6. V_{ds} ranges from 0V to 10V. Different curves represent different applied gate voltages, which range from 0V to -10V. This plot resembles a typical MOSFET I-V characteristics, with a linear region (low V_{ds}) and a saturation region (high V_{ds}).

To better examine the device, a set of electron carrier profiles is presented in

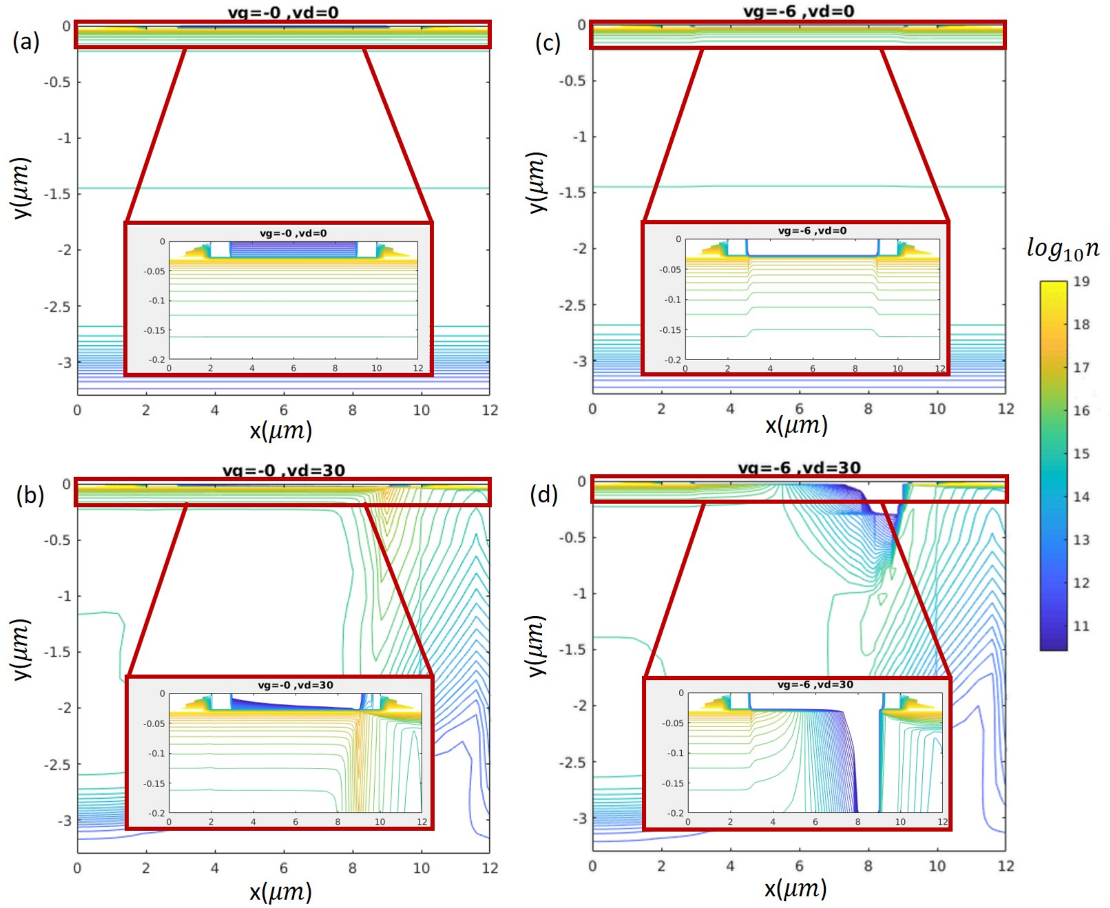

Figure 8.7: Electron concentration profiles for the HEMT under (a) $V_{gs} = 0V$ and $V_{ds} = 0V$; (b) $V_{gs} = 0V$ and $V_{ds} = 30V$; (c) $V_{gs} = -6V$ and $V_{ds} = 0V$; (d) $V_{gs} = -6V$ and $V_{ds} = 30V$

Fig. 8.7. Fig. 8.7 (a) represents the simulation results for $V_{gs} = 0$ and $V_{ds} = 0$; Fig. 8.7 (b) represents those for $V_{gs} = 0$ and $V_{ds} = 30V$; Fig. 8.7 (c) represents those for $V_{gs} = -6$ and $V_{ds} = 0V$; Fig. 8.7 (d) represents those for $V_{gs} = -6$ and $V_{ds} = 30V$. There is an inset for each figure, which is a zoom-in around the channel region. At gate voltage of 0V, the electron concentration under the gate is at the level of $10^{18} cm^{-3}$, as shown in Fig. 8.7 (a) and (b). The different between the two is that, in Fig. 8.7 (b), the channel region under the gate near the drain side

is depleted of electrons due to the applied high drain voltage. This depletion of electrons is called "pinch-off", and this is the reason for the saturation behavior of the I_d versus V_{ds} characteristics.

In Fig. 8.7 (c) , due to the -6V applied on the gate, the electron concentration under the gate is dropped to approximately $10^{15} cm^{-3}$. The channel is closed due to the low electron concentration. In Fig. 8.7 (d), under the drain voltage of 30V, the depletion of electrons is even more severe when compared with the situation shown in Fig. 8.7 (b). The large drain voltage is dropped across the widened depletion region in the channel at the drain side gate edge. Such an extreme voltage drop would also result in high electric field at this region, which is therefore a vulnerable point, prone to breakdown at high drain voltage. One possible solution to this breakdown is to extend the distance between the gate and the drain (l_{gd}). However, because this is a lateral device, increasing l_{gd} means increasing the chip size, which is not desirable for mass production.

8.2 Device Simulation of Current Aperture Vertical Electron Transistor (CAVET)

The CAVET shares some similarity with the HEMT on the stacking of layers, with the exception where a layer of p-type GaN is inserted between the GaN drift region and the UID GaN layer, as shown in Fig. 8.2. Also the drift region is usually doped to ensure desired on-resistance and breakdown voltage. An aperture is opened between the CBL regions to allow the current to flow through and to reach the drain.

Table 8.2: Key parameters for the simulated CAVET.

Parameter	Label	Value
AlGaN layer thickness	t_{AlGaN}	30 nm
Gate to source length	l_{gs}	1 μm
Gate length	l_g	6 μ m
Gate to drain length	l_{gd}	2 μm
Channel to CBL thickness	t_{cGaN}	0.15 μm
CBL thickness	t_{CBL}	0.125 μm
Aperture width	w_{ap}	2 μm

The aperture is usually achieved by masking the area for the aperture during the implantation process for forming the p-type CBL region[81].

The meshing of the simulated CAVET is shown in Fig. 8.8. The key parameters for the device are presented in Table 8.2. Similar to the lateral HEMT, the body doping concentration for AlGaN layer and substrate GaN is $10^{16} cm^{-3}$. The thickness of the substrate GaN is set at approximately 3 μm. The acceptor doping concentration in the CBL region is set at $5 \times 10^{17} cm^{-3}$. The donor doping concentration in the aperture region and the drift region is $2 \times 10^{16} cm^{-3}$. The device width in the third dimension is set at 1 μm.

I_d versus V_{gs} characteristic is obtained through the simulation and is shown in Fig. 8.9, together with the previously obtained I_d versus V_{gs} characteristic for the HEMT. By directly compare the two devices' performances, we can observe that the CAVET has a positive shift of the threshold with respect to that of the HEMT. This

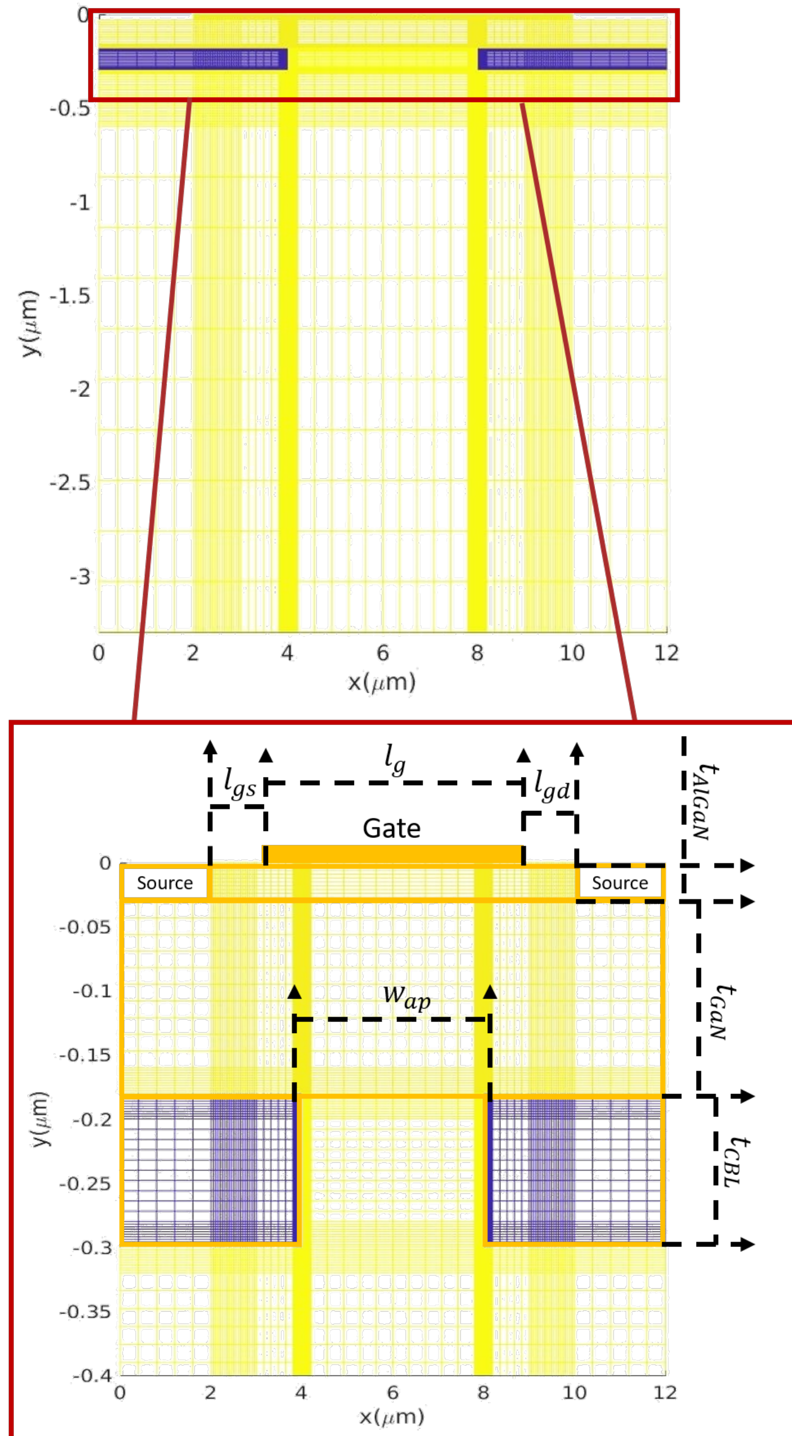

Figure 8.8: Meshing for the simulation of the vertical CAVET and illustration of the parameters presented in Table 8.2.

is due to the existence of the p-type GaN in the CBL region. The holes originating in the CBL region partially deplete the electrons in the channel, thus lowering the electron concentration and causing a positive shift in the threshold. This is also shown in Fig. 8.10, which compares the electron sheet density at the middle point of the channel of both the CAVET and the HEMT, where the electron sheet density of the CAVET is consistently lower than that of the HEMT in the region where $V_g > -6V$.

Other than the shift in threshold, there is a significant difference in the shape of the I_d versus V_{gs} characteristic when comparing both devices. The initial increase of this characteristic curve of CAVET is bigger than that of HEMT. However at around $V_{gs} = -4V$, the curve reaches a region with certain saturation. The initial increase in the drain current is due to the difference in current flow along the channel for the HEMT and the CAVET. In the CAVET, the current flows from the sources at both ends of the channel to the center; while in the HEMT, the current flows only from the source at one end of the channel all the way to the drain on the other end. The CAVET structure has twice the current channel and only half the length of the channel. This is why the initial increase of I_d in I_d versus V_{gs} characteristic curve of the CAVET is bigger than that of the HEMT. When the gate voltage increases, the increase of the current of the CAVET is now not only due to the increase in channel electron density, but also limited by the electron density in the drift region, which is not under the control of the gate. As the gate voltage rises even higher, the current is mainly controlled by the electron density of the drift region, thus causing the saturation behavior of the I_d versus V_{gs} characteristic curve of the CAVET.

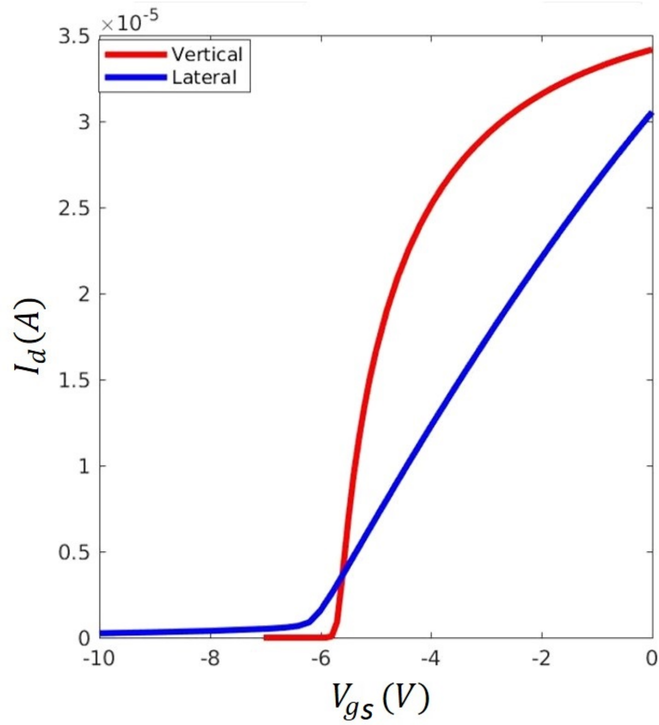

Figure 8.9: Comparison of I_d versus V_{gs} characteristic between the vertical CAVET and the lateral HEMT with V_{ds}=0.02V.

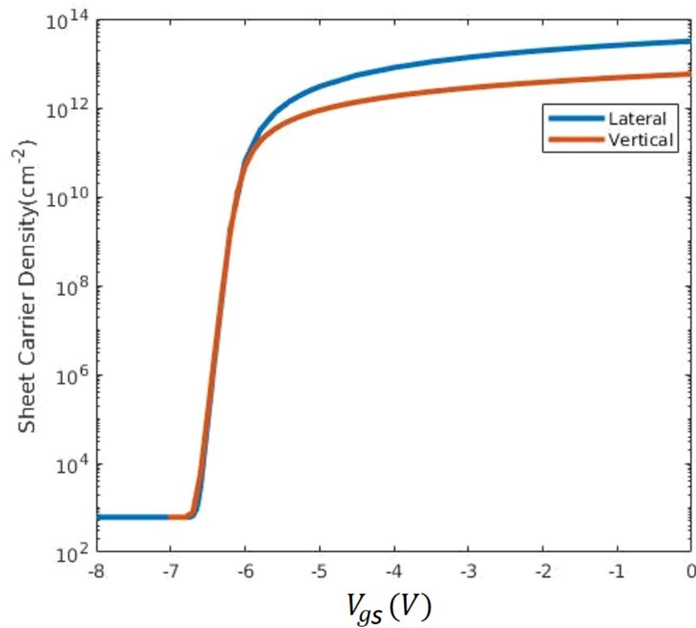

Figure 8.10: Comparison of Sheet electron density at the heterostructure interface versus V_{gs} between the vertical CAVET and the lateral HEMT with V_{ds}=0.02V.

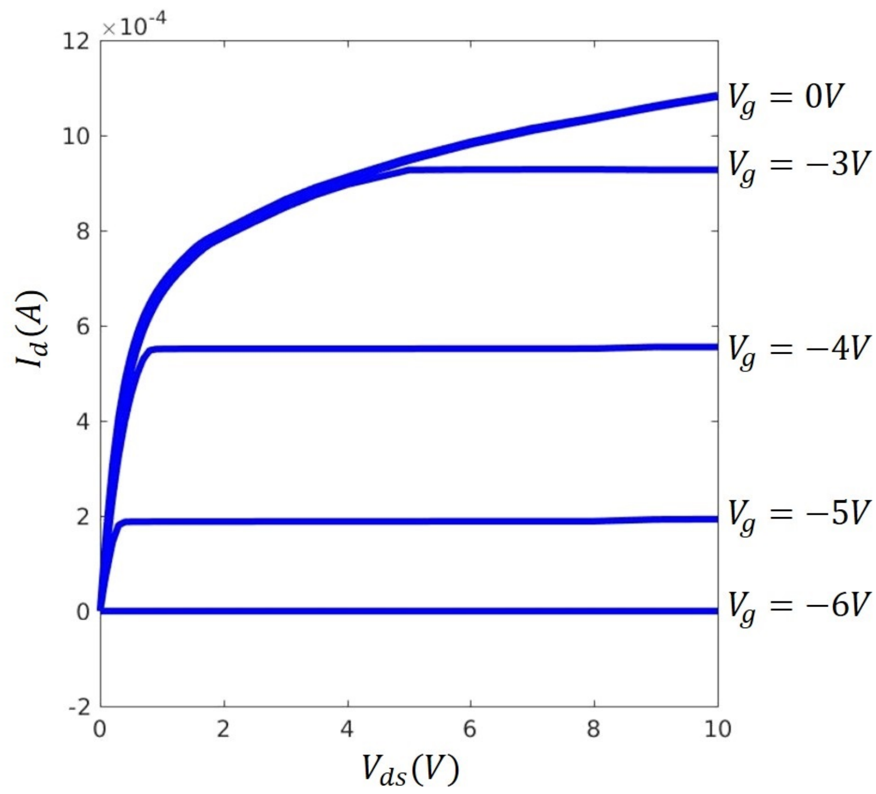

Figure 8.11: I_d versus V_{ds} at various gate voltages of V_{gs}=0V, -3V, -4V, -5V and -6V for the CAVET.

The I_d versus V_{ds} characteristics curves for the CAVET are also obtained during the simulation. This is shown in Fig. 8.11. The drain voltage ranges from 0V to 10V. Different curves correspond to gate voltages of 0, -3V, -4V, -5V and -6V. These curves are similar to those of the HEMT as shown in Fig. 8.6, with a slight shift upwards, with the reason explained previously regarding the differences in I_d versus V_{gs} characteristic between the HEMT and the CAVET. In addition, the saturation behavior is different. In the CAVET simulation, the saturation occurs at a higher V_{ds} voltage than that of the HEMT simulation. At a gate voltage of $V_g = 0V$, the curving does not saturate within the simulated drain voltage range. This could be due to the existence of the drift region. At a lower gate voltage, the electron density under the gate is relatively low, thus easier to be depleted by high drain bias, causing pinch-off and saturation of the current. At higher gate voltage, however, the electron density under the gate is too high to be depleted by the drain voltage. The drain voltage is dropped mostly along the drift region. The I_d-V_{ds} curve behaves more like a resistor in this range. Therefore, there is not a clear saturation for the I_d versus V_{ds} curve at higher gate bias.

To better illustrate this, the electron density profiles under different bias conditions are shown in Fig. 8.12 (a)-(d), where Fig. 8.12 (a) represents the simulation results for $V_{gs} = 0$ and $V_{ds} = 0$; Fig. 8.12 (b) represents those for $V_{gs} = 0$ and $V_{ds} = 30V$; Fig. 8.12 (c) represents those for $V_{gs} = -6$ and $V_{ds} = 0V$; Fig. 8.12 (d) represents those for $V_{gs} = -6$ and $V_{ds} = 30V$.

Comparing Fig. 8.12 (a) and (b), we observe that, at $V_{gs} = 0V$, the electron density from the aperture to the drain remains at the doping concentration level

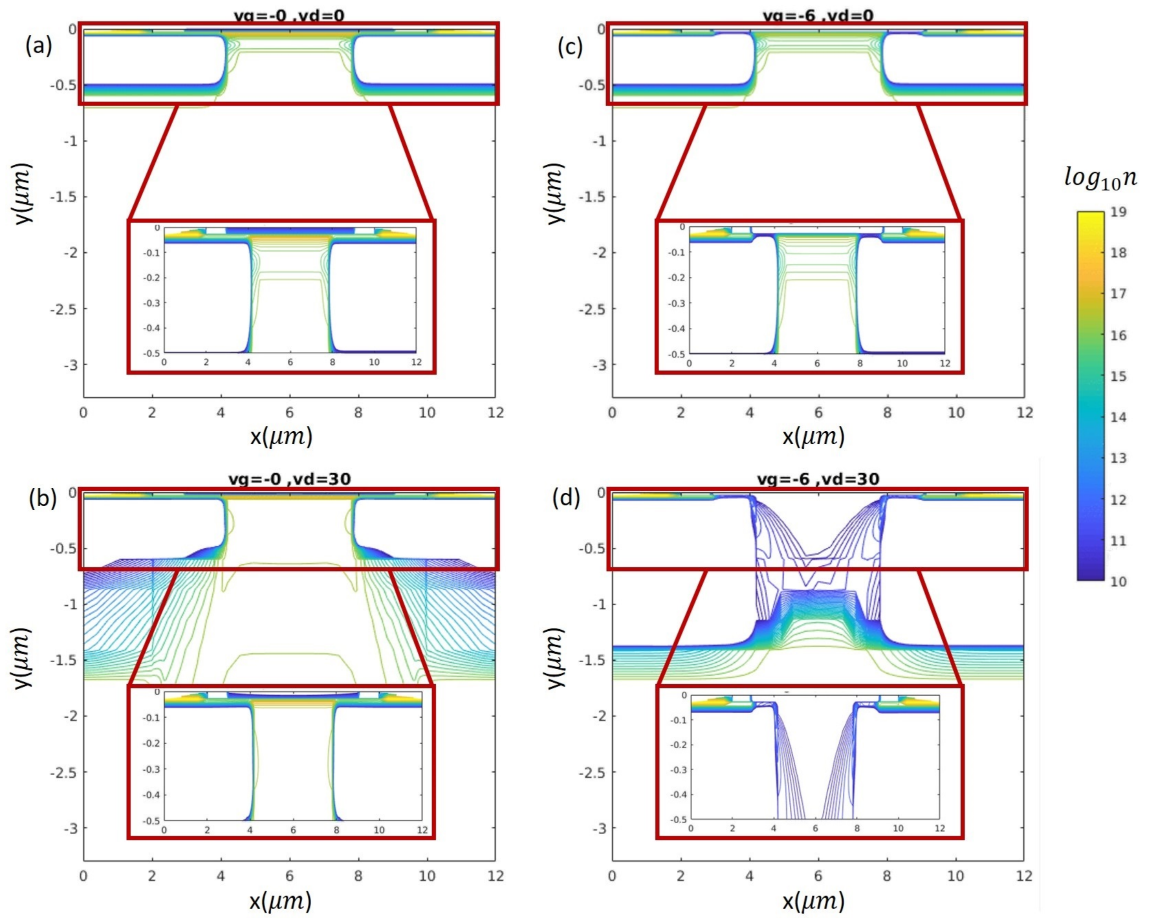

Figure 8.12: Electron concentration profiles for the CAVET under (a) $V_{gs} = 0V$ and $V_{ds} = 0V$; (b) $V_{gs} = 0V$ and $V_{ds} = 30V$; (c) $V_{gs} = -6V$ and $V_{ds} = 0V$; (d) $V_{gs} = -6V$ and $V_{ds} = 30V$

without significant dropping being under high drain bias. This explains the "non-saturation" behavior at gate voltage of 0V in Fig. 8.6.

In Fig. 8.12 (c), the channel is cut off due to the gate voltage of -6V, notably in the region where the gate overlaps with the CBL region. Under such conditions, when the drain voltage increases, the depletion begins to extend into the aperture region, and further into the drift region. This explains the saturation behavior of the I_d versus V_{ds} characteristics of the device at low gate voltage. In addition, this depletion region under high drain bias in the CAVET simulation is extended into the drfit region, while the depletion region in the HEMT simulation is limited near the gate to drain region. The extended depletion region of the CAVET is more effective at dropping the drain voltage without giving rise to extremely high electric field, which is problematic at causing breakdown of the device.

8.3 Summary

In this chapter, we conducted device simulations on two types of GaN devices based on the GaN/AlGaN heterostructure: lateral HEMT and vertical CAVET. Device performances are evaluated and compared between the two devices. The lateral HEMT behaves similar to a typical MOSFET with a negative threshold voltage, indicating it being a normally-on device. The vertical CAVET, which is also a normally-on device in this simulation, has a saturation behavior in the I_d-V_{gs} characteristic and a non-saturation behavior in the I_d-V_{ds} characteristic under high gate voltage. These behaviors don't exist in the lateral HEMT simulation. They

are both due to the existence of the bulk drift region in the CAVET, which is not under the control of the gate. The drift region also helps extending the depletion region under high drain voltage away from the channel, thus providing a longer path to drop the applied drain voltage. The simulations conducted on both devices help explaining the behaviors of the devices and can provide some preliminary insights into designing GaN based devices.

Chapter 9

Summary

This thesis looked into two promising post-silicon materials: Ge and GaN, and investigated the key modeling issues of these two materials.

9.1 Summary of Germanium (Ge)

Ge is considered an excellent candidate for SWIR range photo detecting. However, it suffers from a high dark current due to its intrinsic indirect bandgap material property. Two methods of transforming Ge from indirect to direct bandgap material were investigated: applying strain and alloying with Sn.

EPM is utilized as the main method to conduct the band structure calculation. To successfully model the band structure being influenced by applied strain, EPM was combined with the theory of strain translation that deals with the changes in lattice structure and pseudopotential as a result of applying strain to the crystal. The method successfully revealed the optimal orientation to apply strain, with the largest remaining bandgap at the transition point (denoted "BTP") and the least required strain (denoted "STP"). For uniaxial strain, the optimal direction is along the $\langle 111 \rangle$ direction with a BTP of 0.41eV and an STP of 3.4%. For biaxial strain, the optimal plane is the $\{100\}$ plane with a BTP of 0.45eV and an STP of 2.1%. For hydrostatic strain, a BTP is of 0.636eV and an STP is of 0.86%. The above

results compare favorably with other reported calculations and experiments.

This thesis highlights a problem that arises if the strain-application method is utilized to achieve direct bandgap Ge. This is the miscut angle of the substrate that Ge will be grown atop. The necessity of the miscut angle is discussed in detail in previous chapters. The work investigates how the transition phenomenon is affected if the orientation of the applied strain deviates from its optimal orientation. The simulation results map both BTP and STP along an arbitrary orientation onto a unit contour graph. We also calculated the rate of change of BTP and STP if the orientation tilts from its optimal position. During the process, one interesting fact arose when applying biaxial strain. Despite {100} being the optimal orientation for applying biaxial strain, {110} plane could be a better choice when it comes to robustness against the misalignment from the desired orientation.

Due to the success of EPM in calculating the band structure of Ge, as well as its low computational expenses, EPM is also utilized in the calculation of the band structure of the GeSn alloy. The GeSn alloy is considered another possible method of achieving a direct bandgap material. Its effects are divided into two parts: 1) volume change (the lattice constant change due to the alloying), and 2) the pseudopotential difference resulting from the substitution of Ge atoms by Sn atoms at Ge sites. The inclusion in EPM of the strain translation theory developed in the previous part is also used here. It is used to calculate how the volume change (in the same form as the hydrostatic strain) affects the band structure of the Ge lattice. To account for the effect of the pseudopotential difference between Ge and Sn atoms, first order perturbation theory is utilized. The pure Ge lattice with the

volume change is considered the unperturbed system, while the pseudopotential difference is considered the perturbation of the system. One more parameter is introduced in the simulation: the bowing parameter for the alloy lattice constant. It has a wide range of reported values, differing from paper to paper. Our results indicate that when the bowing parameter ranges from 0A to 0.3A, the required Sn mole fraction to transform GeSn to a direct bandgap material ranges from 8.75% to 5.81%. This shows good agreement with other experimentally measured results. We also conducted a direct comparison with experiments, which provided sufficient data to estimate the bowing parameter of their samples. Our calculation of the direct bandgap for their samples with different Sn mole fractions shows agreement, with the maximum relative difference to be only 5.13%.

In the future, we suggest to develop the methodologies to apply the strain on the {110} plane and ensure that any misalignment tilts towards the {100} plane so that it can obtain the most robustness against the misalignment arising during the process, as suggested by our simulation. Also, the wide range of reported bowing parameters that leads to a choice of treating the bowing parameter as an independent variable in our work deserves our further attention. It will be very useful to help guide future manufacturing process if we can establish the relationship between the manufacturing process and the resulting bowing parameter of the GeSn alloy.

9.2 Summary of Gallium Nitride (GaN)

GaN is a wide bandgap material. This material can form a heterostructure with the ternary compound - AlGaN. The heterostructure can give rise to a layer of electrons confined in a quasi-1D potential well. This quantized 2D electron gas layer shows a different electron transport property when compared to the bulk material. The potential well in which the 2DEG resides changes its shape with different heterostructure configurations or boundary potentials. The effects of the change of potential well on the property of 2DEG is in the scope of the second part of this thesis. An MC simulator is developed to investigate the relationship between the 2DEG transport properties and the potential well shape.

The MC simulation for bulk GaN is conducted first with a three-valley model and several scattering mechanisms including acoustic phonon scattering, piezoelectric scattering, polar optical scattering, impurity scattering and intervalley scattering. The simulation results reveal a drift velocity overshoot resulting from the three-valley model where electrons experience larger effective mass in higher valleys. The peak velocity is around $2.8\times10^7 cm/s$ and the saturation velocity is around $1.5\times10^7 cm/s$. The low-field mobility is estimated to be approximately 800 cm^2/Vs and tends to decrease with increasing doping concentration. These results are compared to other similar MC simulations and reported experimental measurements, and show reasonable agreement.

The MC simulator was then modified to accommodate the simulation of 2DEG at the interface potential well. Inside the potential well, the wave functions are

quantized and coupled to different scattering mechanisms in slightly different ways. The differences between the scattering rates for bulk electron and those for 2DEG are explained in detail in Chapter 5 and partially presented in Chapter 7. Outside the potential well, the electrons are considered to be no longer quantized, and the simulator applies 3D scattering rates.

To quantify the potential well, this work proposed a method to approximate this to a triangular potential well with a potential well height. This method ensures the same sheet carrier density inside both potential wells below Fermi level, and it calculates the approximated potential well's structural parameters (the slope of the triangular well, the height of the well and the width of the well). The potential well is fully investigated by calculating the band alignment across the heterostructure under different configurations and different boundary potentials, and using the method to extract the potential well structural parameters. The calculation results are grouped together to reveal a fixed correlation between the carrier sheet density and potential well structural parameters.

The fixed correlation is then fed into the 2D MC simulation. The simulation is divided into two parts: high electric field simulation (10kV/cm-450kV/cm) and low electric field simulation (2kV/cm-10kV/cm). In the high electric field simulation, at a specific electric field, the drift velocity tends to decrease in the < 50kV/cm range, but increase in the 50 - 100 kV/cm range, with increasing potential well slope. The smaller slope tends to give higher drift velocity, but at the same time is easier for electrons to be scattered out of the potential well, where the electrons experience higher scattering rates and thus slower drift velocity. This is considered the reason

for the crossover behavior of the curves of the drift velocity versus electric field with different slopes.

A drift velocity overshoot is also observed in the simulation in the electric field of $\approx$ 100kV/cm. However, the inclusion of the 2D scattering events tends to affect this property as well. The peak velocity tends to increase with increasing potential well slope, while the electric field at the peak velocity tends to decrease with increasing slope. They both "saturate" at approximately 0.11eV/nm of the potential well slope.

When the electric field increases over 300 kV/cm, the differences between different slopes become increasingly smaller, and are ultimately negligible at the highest simulated electric field (450kV/cm).

In the low electric field simulation, it is observed that lower slope tends to give larger drift velocity. Low-field mobility is extracted from drift velocity versus electric field for different potential well slopes. As mentioned earlier, there is a fixed correlation between the slope and the carrier sheet density inside the well. Because of this, we can compare our calculation with various reported mobility values that also note a measured carrier sheet density. There is a significant agreement between our calculations and the linear regression in the collection of reported values, thus helping verifying our method and results.

Two types of GaN based devices are simulated using Genius Semiconductor Device Simulator. One is a lateral HEMT and the other is a vertical CAVET. I_d versus V_{gs} and I_d versus V_{ds} characteristics are obtained during the simulation. The current of the HEMT is conducted solely through the channel formed at the interface

of the GaN/AlGaN heterostructure. The drain current saturates at high drain voltage bias due to the depletion of electrons at the gate edge near the drain. While for the CAVET, the current flows through the interface channel to the aperture between the CBL, to the drift region, then to the drain contact. The interface channel affects the drain current in a similar way when compared to that of the HEMT under low gate voltages, which shows the behavior of depletion of electrons in the aperture, causing the saturation behavior of the I_d versus V_{ds} characteristics when the drain voltage is high. While under high gate voltage, the drain current is less limited by the channel electron concentration. The limit from the drift region is more significant and the I_d versus V_{ds} does not have the saturation behavior at $V_{gs} = 0$ with V_{ds} ranges from 0 to 10V.

Bibliography

[1] C. Boztug, J. R. Sánchez-Pérez, F. Cavallo, M. G. Lagally, R. Paiella, "Strained-Germanium Nanostructures for Infrared Photonics", ACS Nano 2014 8 (4), 3136-3151

[2] V. R. D'Costa, C. S. Cook, A. G. Birdwell, C. L. Littler, M. Canonico, S. Zollner, J. Kouvetakis, J. Menéndez, "Optical critical points of thin-film $Ge_{1-y}Sn_y$ alloys: A comparative $Ge_{1-y}Sn_y/Ge-1-xSi_x$ study", Phys. Rev. B 73, 125207 – Published 31 March 2006

[3] D. Vasileska, "Tutorial for Semi-Empirical Band-Structure Calculation" downloaded from https://www.nanohub.org/

[4] D. J. Chadi and M. L. Cohen, "Tight-binding calculations of the valence bands of diamond and zincblende crystals" Phys. Stat. Sol. (b), 68 (1975) 405.

[5] J. Luttinger and W. Kohn,"Motion of Electrons and Holes in Perturbed Periodic Fields" Phys. Rev., 97 (1955) 869.

[6] M. L. Cohen and T. K. Bergstresser, "Band Structures and Pseudopotential Form Factors for Fourteen Semiconductors of the Diamond and Zinc-blende Structures" Phys. Rev., 141 (1966) 789.

[7] J. R. Chelikowsky and M. L. Cohen, "Nonlocal pseudopotential calculations for the electronic structure of eleven diamond and zinc-blende semiconductors" Phys Rev. B, 14 (1976) 556.

[8] J. Kim and M. V. Fischetti, "Empirical Pseudopotential Calculation of Band Structure and Deformation Potentials of Biaxially Strained Semiconductors," 2009 13th International Workshop on Computational Electronics, Beijing, 2009, pp. 1-4.

[9] O. Aldaghri, Z. Ikonić, R. W. Kelsall, "Optimum Strain Configurations for Carrier Injection in Near Infrared Ge Lasers", J. Appl. Phys. 2012, 111, 053106

[10] F. Zhang, V.H. Crespi,P. Zhang, "Prediction that Uniaxial Tension along $\langle 111 \rangle$ Produces a Direct Band Gap in Germanium Phys", Rev. Lett. 2009, 102, 156401

[11] M. El Kurdi, G. Fishman, S. Sauvage, J. Boucaud, "Band Structure and Optical Gain of Tensile-Strained Germanium Based on a 30 Band k·p Formalism", J. Appl. Phys. 2010, 107, 013710

[12] E.A. Fitzgerald, S.B. Samavedam, "Utilization of miscut substrates to improve relaxed graded silicon-germanium and germanium layers on silicon", US Patent 6039803 A, March 2000

[13] D. W. Jenkins, J. D. Dow, "Electronic properties of metastable Ge_ySn_{1-y} alloys" Phys. Rev. B 36, 7994

[14] P. Moontragoon, Z. Ikonić, P. Harrison, "Band structure calculations of Si–Ge–Sn alloys: achieving direct band gap materials", Semiconductor Science and Technology, Volume 22, Number 7, Published 31 May 2007

[15] M. Lee, P. Liu, Y.A Hong, Y. Chou, J. Hong, Y Siao, "Electronic band structures of Ge1-xSnx semiconductors: A first-principles density functional theory study" Journal of Applied Physics, 113, 063517 (2013)

[16] C. Darmody and D. P. Ettisserry and N. Goldsman, and N. K. Dhar, "Using density functional theory to engineer direct gap germanium-tin alloy," in 2015 International Conference on Simulation of Semiconductor Processes and Devices (SISPAD) (2015) pp. 329–332.

[17] N. Bhargava, M. Coppinger, J. Prakash Gupta, L. Wielunski, and J. Kolodzey, "Lattice constant and substitutional composi- tion of GeSn alloys grown by molecular beam epitaxy," Applied Physics Letters 103, 041908 (2013).

[18] C. Kittel, "INTRODUCTION TO SOLID STATE PHYSICS, 7TH ED.", Wiley India Pvt.Limited, 2007.

[19] S. Shao-Jian, C. Bu-Wen, X. Chun-Lai, Z. Dong-Liang, Z. Guang-Ze, and W. Qi-Ming, "Lattice constant deviation from Vegard's law in GeSn alloys," Acta Physica Sinica 61, 176104 (2012).

[20] S. Wirths, R. Geiger, N. von den Driesch, G. Mussler, T. Stoica, S. Mantl, Z. Ikonic, M. Luysberg, S. Chiussi, J. M. Hartmann, H. Sigg, J. Faist, D. Buca, D. Grützmacher, "Lasing in direct-bandgap GeSn alloy grown on Si" Nature Photonics 9, 88–92 (2015)

[21] B.K. Ridley, "Quantum Processes in Semiconductors", Oxford science publications. OUP Oxford, 1999.

[22] Tsuneya Ando, Alan B. Fowler, and Frank Stern. "Electronic properties of two-dimensional systems", 54:437-672, 03 1982.

[23] S. Datta. "Quantum phenomena", Modular Series on Solid State Devices, Vol 8. Addison-Wesley Longman, Incorporated, 1989.

[24] M. Lundstrom. "Fundamentals of Carrier Transport", Cambridge University Press, 2009.

[25] M.H Lee, P.L. Liu, Y.A. Hong, Y.T. Chou, J. Y. Hong, and Y. J. Siao, "Electronic band structures of $Ge_{1-x}\,Sn_x$ semiconductors: A first-principles density functional theory study," Journal of Applied Physics 113, 063517 (2013).

[26] Y. C. Yeo, T. C. Chong, and M. F. Li, "Electronic band structures and effective-mass parameters of wurtzite GaN and InN", Journal of Applied Physics 1998 83:3, 1429-1436.

[27] B. Monemar, "Fundamental energy gap of GaN from photoluminescence excitation spectra", Phys. Rev. B 10, 676 – Published 15 July 1974

[28] R. J. Trew, "SiC and GaN transistors - is there one winner for microwave power applications?" in Proceedings of the IEEE, vol. 90, no. 6, pp. 1032-1047, Jun 2002.

[29] H. Yamashita, K. Fukui, S. Misawa, S. Yoshida, "Optical properties of AlN epitaxial thin films in the vacuum ultraviolet region", J. Appl. Phys. 50 (1979) 896.

[30] S. Heikman, S. Keller, Y. Wu, J. S. Speck, S. P. DenBaars, and U. K. Mishra, "Polarization effects in AlGaN/GaN and GaN/AlGaN/GaN heterostructures", Journal of Applied Physics 2003 93:12, 10114-10118

[31] R. S. Pengelly, S. M. Wood, J. W. Milligan, S. T. Sheppard and W. L. Pribble, "A Review of GaN on SiC High Electron-Mobility Power Transistors and MMICs," in IEEE Transactions on Microwave Theory and Techniques, vol. 60, no. 6, pp. 1764-1783, June 2012.

[32] S. Bloom, G. Harbeke, E. Meier, I. B. Ortenburger, "Band structure and Reflectivity of GaN", physica status solidi, 1974

[33] M. Leszczynski, H. Teisseyre, T. Suski, I. Grzegory, M. Bockowski, J. Jun, and S. Porowski K. Pakula and J. M. Baranowski C. T. Foxon and T. S. Cheng, "Lattice parameters of gallium nitride", Applied Physics Letters 1996 69:1, 73-75

[34] V. Bougrov, M.E. Levinshtein, S.L. Rumyantsev, A. Zubrilov, in "Properties of Advanced SemiconductorMaterials GaN, AlN, InN, BN, SiC, SiGe" . Eds. M.E. Levinshtein, S.L. Rumyantsev, M.S. Shur, John Wiley & Sons, Inc., New York, 2001, 1-30.

[35] E. Peng, X. Wang, H. Xiao, C. Wang, H. Yin, H. Chen, C. Feng, L. Jiang, X. Hou, Z. Wang, "Growth and characterization of AlGaN/AlN/GaN/AlGaN double heterojunction structures with AlGaN as buffer layers", Journal of Crystal Growth, Volume 383, 15 November 2013, Pages 25-29, ISSN 0022-0248

[36] L. Shen, S. Heikman, B. Moran, R. Coffie, N.-Q. Zhang, D. Buttari, I. P. Smorchkova, S. Keller, S. P. DenBaars, and U. K. Mishra, "AlGaN/AlN/GaN High-Power Microwave HEMT", IEEE Electron Device Letters, VOL. 22, NO. 10, Oct. 2001

[37] D. Tsvetkov, Yu. Melnik, A. Davydov, A. Shapiro, O. Kovalenkov, J.B. Lam, J.J. Song and V. Dmitriev, "Growth of Submicron AlGaN/GaN/AlGaN Heterostructures by Hydride Vapor Phase Epitaxy (HVPE)", phys.stat.sol.(a) 188, No.1, 429–432 (2001)

[38] P. Ellinghaus, "Simulation of GaN / AlGaN heterostructures for a HEMT simulator", Master Thesis in Mathematical Engineering, Department of Pure and Applied Mathematics, Università degli Studi dell'Aquila

[39] S. Nandi, M. Sarkar, and A. Ghosal, "Monte-Carlo study of hot electron transport in bulk Gan," Journal of Electron Devices 18, 1501–1504 (2013)

[40] M. Farahmand ; C. Garetto ; E. Bellotti ; K.F. Brennan ; M. Goano ; E. Ghillino ; G. Ghione ; J.D. Albrecht ; P.P. Ruden "Monte Carlo simulation of electron transport in the III-nitride wurtzite phase materials system: binaries and ternaries", in IEEE Transactions on Electron Devices, vol. 48, no. 3, pp. 535-542, Mar 2001.

[41] D. C. Herbert, M. J. Uren, B. T. Hughes, D. G. Hayes,J. C. H. Birbeck, R. Balmer, T Martin.1, G. C. Crow, R. A. Abram, M. Walmsley, R. A. Davies,R. H. Wallis, W. A. Phillips and S. Jones,"Monte Carlo simulations of AlGaN/GaN heterojunction field-effect transistors (HFETs)", J. Phys.: Condens. Matter 14 (2002) 3479–3497

[42] T.H. Yu and K. F. Brennan, "Monte Carlo calculation of two-dimensional electron dynamics in GaN–AlGaN heterostructures", Journal of Applied Physics, 91, 3730 (2002)

[43] M. Ramonas, A. Matulionis and L. Rota, "Monte Carlo simulation of hot-phonon and degeneracy effects in the AlGaN/GaN two-dimensional electron gas channel", Semicond. Sci. Technol. 18 (2003) 118–123

[44] L. Ardaravičius, A. Matulionis, J. Liberis, O. Kiprijanovic, and M. Ramonas, "Electron drift velocity in AlGaNÕGaN channel at high electric fields", Applied Physics Letters 2003 83:19, 4038-4040

[45] J. J. Wortman, R. A. Evans, "Young's Modulus, Shear Modulus, and Poisson's Ratio in Silicon and Germanium", Journal of Applied Physics 36, 153 (1965), doi: http://dx.doi.org/10.1063/1.1713863

[46] J. Kim and M. V. Fischetti, "Empirical Pseudopotential Calculation of Band Structure and Deformation Potentials of Biaxially Strained Semiconductors," 2009 13th International Workshop on Computational Electronics, Beijing, 2009, pp. 1-4.

[47] M. V. Fischetti and S. E. Laux, "Band structure, deformation potentials, and carrier mobility in strained Si, Ge, and SiGe alloys," Journal of Applied Physics 80, 2234-2252 (1996).

[48] M. Bauer, J. Taraci, J. Tolle A.V.G Chizmeshya, S. Zollner, J. Menendez, D. J. Smith and J. Kouvetakis, "Ge-Sn semiconductors for band-gap and lattice engineering", Applied Physics Letters 81, 2992 (2002).

[49] Y. Chibane, B. Bouhafs, and M. Ferhat, "Unusual structural and electronic properties of Sn_xGe_{1-x} alloys," physica status solidi (b) 240, 116–119 (2003)

[50] C. Xu, C. L. Senaratne, R. J. Culbertson, J. Kouvetakis, and J. Menndez, "Deviations from Vegard's law in semiconductor thin films measured with X-ray diffraction and Rutherford backscattering: The $Ge_{1-y}Sn_y$ and $Ge_{1-x}Si_x$ cases," Journal of Applied Physics 122, 125702 (2017).

[51] V. R. D'Costa, C. S. Cook, A. G. Birdwell, C. L. Littler, M. Canonico, S. Zollner, J. Kouvetakis, and J. Menéndez, "Optical critical points of thin-film Ge_{1-y} Sn_y alloys: A comparative $\mathrm{Ge}_{1-y}\mathrm{Sn}_y$ /Ge_{1-x} Si_x study," Phys. Rev. B 73, 125207 (2006).

[52] Zhongyunshen Zhu, Yuxin Song, Qimiao Chen, Zhenpu Zhang, Liyao Zhang, Yaoyao Li, and Shumin Wang "Theoretical Investigation of Biaxially Tensile-Strained Germanium Nanowires." Nanoscale Research Letters 12 (2017): 472. PMC. Web. 29 Sept. 2018.

[53] Monica Bollani, Daniel Chrastina, Luca Gagliano, Lidia Rossetto, Daniele Scopece, Michael Barget, Valeria Mondiali, Jacopo Frigerio, Mario Lodari, Fabio Pezzoli, Francesco Montalenti, and Emiliano Bonera, "Local uniaxial tensile strain in germanium of up to 4% induced by SiGe epitaxial nanostructures", Appl. Phys. Lett. 107, 083101 (2015)

[54] K. Tomizawa, "Numerical Simulation of Submicron Semiconductor Devices", Artech House materials science library, 1993

[55] A. Hamdoune and N.-E. C. Sari, "Application of the monte carlo method for the calculation of electrical properties, in both wurtzite and zinc blende phases, of gallium nitride," Physics Procedia 2, 905 – 911 (2009), proceedings of the JMSM 2008 Conference.

[56] F. M. A. El-Ela and A. Z. Mohamed, "Electron transport characteristics of wurtzite gan," ISRN Condensed Matter Physics 2013, 58–72 (2013).

[57] B. Benbakhti, M. Rousseau, A. Soltani, and J.-C. D. Jaeger, "Electron transport properties of gallium nitride for microscopic power device modelling," Journal of Physics: Conference Series 193, 012005 (2009).

[58] D. L. Rode and D. K. Gaskill, "Electron hall mobility of ngan," Applied Physics Letters 66 (1995).

[59] R. P. Tompkins and D. Nguyen, "Contactless mobility, carrier density, and sheet resistance measurements on si, gan, and algan/gan high electron mobility transistor (hemt) wafers," ARL-TR-7209,FEB 2015

[60] H. Tang and J. B. Webb, "Growth of high mobility gan by ammonia-molecular beam epitaxy," Applied Physics Letters 74 (1999).

[61] J. M. Redwing, M. A. Tischler, J. S. Flynn, S. Elhamri, M. Ahoujja, R. S. Newrock, and W. C. Mitchel, "Two dimensional electron gas properties of AlGaN/GaN heterostructures grown on 6H-SiC and sapphire substrates," Applied Physics Letters 69 (1996).

[62] Feng Zhang, Vincent H. Crespi, and Peihong Zhang. "Prediction that uniaxialtension along $\angle 111\rangle$ produces a direct band gap in germanium" Phys. Rev. Lett.,102:156401, Apr 2009.

[63] Peng Huei Lim, Sungbong Park, Yasuhiko Ishikawa, and Kazumi Wada, "Enhanced direct bandgap emission in germanium by micromechanical strain engineering," Opt. Express 17, 16358-16365 (2009)

[64] A. T. M. Fairus and V. K. Arora, "Quantum Engineering of Nanoelectric Devices: the Role of Quantum Confinement on Mobility Degradation," Microelectronics Journal, vol. 32, no. 8, pp. 679-686, 2000.

[65] N. Matsuo, Y. Takami, and Y. Kitagawa, "Modeling of Direct Tunneling for Thin SiO_2 Film on n-Type Si (100) by WKB Method Considering the Quantum

Effect in the Accumulation Layer," Solid-State Electron., vol. 46, no. 4, pp. 577-579, 2002.

[66] S. Padmanabhan and A. Rothwarf, "Quantum Inversion Layer Mobility: Numerical Results," IEEE Trans.Electron Devices, vol. 36, no. 11, pp. 2557-2566, 1989.

[67] M. J. van Dort, P. H. Woerlee, and A. J. Walker, "A Simple Model for Quantisation Effects in Heavily-Doped Silicon MOSFETs at Inversion Conditions," Solid-State Electron., vol. 37, no. 3, pp. 411-414, 1994.

[68] A. Polyakov, N. Smirnov, A. Govorkov, E. Kozhukhova, T. Yugova, A. Usikov, H. Helava, and Y. Makarov, "Improved GaN films with low background doping and low deep trap density grown by hydride vapor phase epitaxy," physica status solidi (c) 12, 341–344 (2015).

[69] J. W. P. Hsu, M. J. Manfra, D. V. Lang, S. Richter, S. N. G. Chu, A. M. Sergent, R. N. Kleiman, L. N. Pfeiffer, and R. J. Molnar, "Inhomogeneous spatial distribution of reverse bias leakage in GaN schottky diodes," Applied Physics Letters 78, 1685–1687 (2001).

[70] O. Ambacher, B. Foutz, J. Smart, J. R. Shealy, N. G. Weimann, K. Chu, M. Murphy, A. J. Sierakowski, W. J. Schaff, L. F. Eastman, R. Dimitrov, A. Mitchell, and M. Stutzmann, "Two dimensional electron gases induced by spontaneous and piezoelectric polarization in undoped and doped AlGaN/GaN heterostructures," Journal of Applied Physics 87, 334–344 (2000).

[71] Y. Wu, B. P. Keller, S. Keller, D. Kapolnek, P. Kozodoy, S. P. Denbaars, and U. K. Mishra, "Very high breakdown voltage and large transconductance realized on GaN heterojunction field effect transistors," Applied Physics Letters 69 (1996).

[72] F. Recht, L. McCarthy, S. Rajan, A. Chakraborty, C. Poblenz, A. Corrion, J. S. Speck, and U. K. Mishra, "Nonalloyed ohmic contacts in AlGaN/GaN HEMTs by ion implantation with reduced activation annealing temperature," IEEE Electron Device Letters 27, 205–207 (2006).

[73] R. Gaska, J. W. Yang, A. Osinsky, Q. Chen, M. A. Khan, A. O. Orlov, G. L. Snider, and M. S. Shur, "Electron transport in AlGaN/GaN heterostructures grown on 6H-SiC substrates," Applied Physics Letters 72 (1998).

[74] O. Katz, A. Horn, G. Bahir, and J. Salzman, "Electron mobility in an AlGaN/GaN twodimensional electron gas. i. carrier concentration dependent mobility," IEEE Transactions on Electron Devices 50, 2002–2008 (2003).

[75] R. Swain, K. Jena, T. R. Lenka, G. N. Dash, and A. K. Panda, "DC and RF characteristics of normally-off AlN/GaN MOSHEMT by varying oxide thickness," in 2015 IEEE International Conference on Electron Devices and Solid-State Circuits (EDSSC) (2015) pp. 399-402.

[76] A. Yamamoto, S. Makino, K. Kanatani, and M. Kuzuhara, "AlGaN/GaN heterostructures with an AlGaN layer grown directly on reactive-ion-etched GaN showing a high electron mobility (>1300 $cm^2V^{-1}s^{-1}$)," physica status solidi (c) 12, 341-344 (2015)

[77] Lehighton Electronics Inc., "Non-contact metrology for mobility and resistivity," (2016), [Online; accessed 18-July-2018].

[78] I. Nifa, C. Leroux, A. Torres, M. Charles, D. Blachier, G. Reimbold, G. Ghibaudo, and E. Bano, "Characterization of 2DEG in AlGaN/GaN heterostructure by hall effect," Microelectronic Engineering 178, 128 - 131 (2017), special issue of Insulating Films on Semiconductors (INFOS 2017).

[79] H.-P. Lee, J. Perozek, L. D. Rosario, and C. Bayram, "Investigation of AlGaN/GaN high electron mobility transistor structures on 200-mm silicon (111) substrates employing different buffer layer configurations," Scientific Reports 6 (2016)

[80] I. H. Lee, Y. H. Kim, Y. J. Chang, J. H. Shin, T. Jang, and S. Y. Jang, "Temperature-dependent hall measurement of AlGaN/GaN heterostructures on Si substrates," Journal of the Korean Physical Society 66, 61-64 (2015).

[81] S. Chowdhury and U. K. Mishra, "Lateral and Vertical Transistors Using the AlGaN/GaN Heterostructure," in IEEE Transactions on Electron Devices, vol. 60, no. 10, pp. 3060-3066, Oct. 2013.

[82] R. Reiner, P. Waltereit, B. Weiss, R. Quay and O. Ambacher, "Investigation of GaN-HEMTs in Reverse Conduction," PCIM Europe 2017; International Exhibition and Conference for Power Electronics, Intelligent Motion, Renewable Energy and Energy Management, Nuremberg, Germany, 2017, pp. 1-8.

[83] C. Sørensen et al., "Conduction, reverse conduction and switching characteristics of GaN E-HEMT," 2015 IEEE 6th International Symposium on Power Electronics for Distributed Generation Systems (PEDG), Aachen, 2015, pp. 1-7.

[84] D. Jin and J. A. del Alamo, "Mechanisms responsible for dynamic ON-resistance in GaN high-voltage HEMTs," 2012 24th International Symposium on Power Semiconductor Devices and ICs, Bruges, 2012, pp. 333-336.